DENSE GRANULAR FLOW IN ROTATING DRUMS: A COMPUTATIONAL INVESTIGATION OF CONSTITUTIVE EQUATIONS

TIMOTHY MARK POVALL

Thesis presented for the degree of Doctor of Philosophy
in the Department of Physics
University of Cape Town

April 2018

Supervisors:
Prof. Indresan Govender
Dr Andrew McBride
Prof. B. Daya Reddy

DECLARATION

I know the meaning of plagiarism and declare that all of the work in this thesis, save for that which is properly acknowledged, is my own

Vancouver, April 2018

Timothy Mark Povall

ABSTRACT

The constitutive laws of dense granular flow are investigated. Simulations of a drum, with periodic boundary conditions, rotating at varying speeds are performed. From the resulting data, kinematic and kinetic fields are extracted and used to investigate the validity of constitutive relations proposed in the literature (Jop et al., 2006; Pathmathas, 2015; da Cruz et al., 2005). Two key constitutive assumptions are (a) isotropy and (b) incompressibility. The rotating drum system is found to be largely isotropic for high rotational speeds. For low rotational speeds, anisotropy is observed in the bottom part of the system, where the particles are flowing upwards. A small degree of compressibility is observed in the downward-flowing layer. The friction coefficient for the granular constitutive relations is also investigated. An empirically-derived friction law has a better fit to the data when compared to other friction laws proposed in the literature. Lastly, two scaling laws are investigated: the scaling between the scaled flow-rate (flux) and the thickness of the downward-flowing layer and the scaling between the dynamic angle of repose of the bed and the flux through the downward-flowing layer. The thickness-flux scaling is measured by interpolating the flux over a number of slices through the flowing layer, this is done in a number of different ways. The size of the measured section through the flowing layer is varied. The orientation of the slices is also varied. Also investigated is whether the total velocity or the tangential velocity produce the same scaling. The size of the section of the flowing layer significantly changes the scaling, this shows that the scaling is not constant throughout the flowing layer. The dynamic angle of repose is determined using two methods, one which is determined unambiguously as the repose angle of the ellipse fitted to the equilibrium surface and the other which is the changing angle of the tangent to the equilibrium surface or free surface. The first repose angle is found to be highly dependent on the flux even in the limit of infinite drum length, which is modelled using axial periodic boundary conditions. The second definition results in two sets of repose angles with complex behaviour that may be due to inertial effects. An instability in the system is observed, this is conjectured to be due to a frictional threshold that is breached as the rotational speed of the drum increases. Algorithms for calculating field variables and features of the charge are presented.

namque papaveris haustus itemst facilis quod aquarum;
nec retinentur enim inter se glomeramina quaeque
et perculsus item proclive volubilis exstat.

(And you may scoop up poppy seed as easily
As water, which will also, if you spill it,
Glide away with as ready a downward flow.)

— Lucretius (99-55 B.C.), "De Rerum Natura"
(R. C. Trevelyan, 1937)

ACKNOWLEDGMENTS

I am grateful to my supervisors Dr Andrew McBride and Prof. Indresan Govender for their advice and support. My thanks go to Prof. Daya Reddy for providing work space at the Centre for Research in Computational and Applied Mechanics as well as my peers in this space for the positive and stimulating work environment. The funding provided by the National Research Foundation and the Centre for Minerals Research is gratefully acknowledged. I greatly appreciate encouragement from family and friends. My thanks to Keri Povall and Ron Uken for providing a comfortable working space during the final stages of writing. I am appreciative of the advice and interest from my parents, Mark and Julie Povall. Most importantly, I am grateful to my wife Raïssa Philibert for all of her support.

CONTENTS

LIST OF FIGURES

LIST OF TABLES

LIST OF ALGORITHMS

NOTATION

The following is a summary of standard notation adopted.

SCALARS, VECTORS AND TENSORS

The field variables used in continuum mechanics can be scalar, vector- or tensor-valued. These are generally represented by lower-case, bold lower-case and bold upper-case characters, respectively, e.g.

$$\begin{aligned} \text{scalars} \quad & a, b, \rho, \cdots \\ \text{vectors} \quad & \mathbf{u}, \boldsymbol{\chi}, \cdots \\ \text{tensors (second-order)} \quad & \boldsymbol{\sigma}, \boldsymbol{C}, \cdots \end{aligned}$$

Vectors and tensors are also represented in indicial form relative to a fixed Cartesian basis $\mathbf{e}_i,\ i = 1, 2, 3$, e.g.

$$\begin{aligned} &\mathbf{u} = u_i \mathbf{e}_i, \\ &\mathbf{C} = C_{ij} \mathbf{e}_i \otimes \mathbf{e}_j. \end{aligned}$$

The convention in index notation is that the sum is taken over repeated subscripts, i.e.

$$C_{ij} x_j = \sum_{j=1}^{N_{\text{dim}}} C_{ij} x_j,$$

where N_{dim} is the rank (dimension) of the tensor or vector. Tensors are linear transformations of other tensors. A second-order tensor is a linear transformation of a vector (first-order tensor) to another vector, e.g.

$$\mathbf{Cx} = \mathbf{b} \text{ or } C_{ij} x_j = b_i.$$

OPERATIONS

The trace of a second order tensor $\boldsymbol{T}$ is defined as the sum over the diagonal entries in the tensor:

$$\operatorname{tr}(\boldsymbol{T}) = T_{ii}. \tag{0.1}$$

The vector dot product is the scalar product between two vectors:

$$\boldsymbol{a} \cdot \boldsymbol{b} = a_i b_i. \tag{0.2}$$

The vector cross product is given by

$$\boldsymbol{a} \times \boldsymbol{b} = a_i b_j \varepsilon_{ijk}, \tag{0.3}$$

where ε_{ijk} is the Levi-Civita tensor, in 3D given by

$$\varepsilon_{ijk} = \begin{cases} +1 & \text{if } (i,j,k) \text{ is } (1,2,3),(2,3,1) \text{ or } (3,1,2), \\ -1 & \text{if } (i,j,k) \text{ is } (3,2,1),(1,3,2) \text{ or } (2,1,3), \\ 0 & \text{if } i=j, \text{ or } j=k, \text{ or } k=i. \end{cases} \tag{0.4}$$

DERIVATIVES, GRADIENT AND DIVERGENCE

The derivatives of scalar, vector and tensor fields are defined by

$$\begin{aligned} \frac{\partial a}{\partial \mathbf{x}} &= \frac{\partial a}{\partial x_j}\mathbf{e}_j, \\ \frac{\partial \mathbf{u}}{\partial \mathbf{x}} &= \frac{\partial u_i}{\partial x_j}\mathbf{e}_i \otimes \mathbf{e}_j. \end{aligned}$$

The gradient operator is the derivative of a field relative to the spatial (Eulerian) or material (Lagrangian) setting. All of the fields and operators in this work are expressed relative to a spatial setting. The gradient of an arbitrary vector field $\mathbf{u}$ is denoted by

$$\operatorname{grad}\mathbf{u} \equiv \frac{\partial \mathbf{u}}{\partial \mathbf{x}} = \frac{\partial u_i}{\partial x_j}\mathbf{e}_i \otimes \mathbf{e}_j.$$

The divergence of an arbitrary vector field $\boldsymbol{u}$ is denoted by

$$\operatorname{div}(\boldsymbol{u}) = \frac{\partial u_i}{\partial x_i}.$$

The divergence of an arbitrary tensor field $\mathbf{T}$ is denoted by

$$\operatorname{div}(\mathbf{T}) = \frac{\partial T_{ij}}{\partial x_j}\mathbf{e}_i.$$

1

INTRODUCTION

A granular system is composed of a collection of particles that range in size from 1µm, e. g. talcum powder, to 1km, e. g. asteroids. The microscopic and macroscopic scales are the scales of, respectively, the unseen (small) and seen (large) parts of a system. The macroscopic scale is generally considered to be many orders of magnitude larger than the microscopic scale. In granular systems the microscopic scale is the scale of the particle. Depending on the size of the particle the micro- and macro-scales can be separated by only a few orders of magnitude. Some granular systems are therefore more accurately defined as mesoscopic systems, which exist in the intermediate scale between microscopic and macroscopic.

Granular systems can have features that resemble solid-, liquid-, and gas-like flow. The phases of flow are characterized by the types of interactions between the particles. In solid-like flows, particles mostly interact via frictional contacts. Gas-like flows have interactions dominated by collisional contacts. Liquid-like flows exhibit a combination of frictional and collisional interactions. A dense granular system is composed of dry particles that are mostly in contact with one another. The particles in a system undergoing rapid dense granular flow are travelling at high velocities, e. g. flows of sand down a dune. However, the velocity of the particles in such systems is not high enough for the particles to be flowing in a predominantly gas-like manner. The material studied in this thesis is undergoing rapid dense flow and is composed of dry spherical particles.

Comminution is the process of reducing the average size of the particles in a granular system. Tumbling mills are horizontally-oriented drums commonly used in the mining industry for comminution. The particles in a tumbling mill are crushed as it rotates. The mechanism of breakage in a tumbling mill is not clearly understood. The two main mechanisms that have been proposed are attrition, a slow wearing-down of the surface of the particles, and fracture (Hogg, 1999). In industry, tumbling mill efficiency is optimized based on empirical models. At best the efficiency of tumbling mills (the percentage of energy that is used to break the particles) is around 5% and the energy used in tumbling mills accounts for around 60% of the plant's operating costs (Wills et al., 2015). A complete mechanistic model of breakage in a tumbling mill does not yet exist. This would be invaluable as it would allow for rapid prototyping of industrial mills. In this thesis the rotating drum system is studied; this is an idealization of a tumbling mill with dry spherical particles.

Key to a mechanistic model of tumbling mills is a constitutive law for granular flow. Constitutive laws are relations between kinematic and kinetic quantities. Jop et al. (2006) proposed a widely-adopted three-dimensional (3D) constitutive law for rapid dense granular flow of dry particles. The constitutive law assumes that the flow has a response that is independent of the orientation at a point, i. e. isotropic, and of constant density, i. e. incompressible. The main aim of this thesis is to investigate the validity of Jop et al.'s law by assessing these assumptions. The isotropy assumption is assessed using a novel measure for quantifying the degree of anisotropy in the system. The compressibility assumption is assessed using the spatial gradient of the velocity. In addition, Jop et al.'s proposed form of the viscosity, also called the friction coefficient, is evaluated and compared with the form proposed by da Cruz et al. (2005), and a new empirically-derived form.

The investigations to confirm Jop et al.'s law may be considered an extension of the work of Rycroft et al. (2009) and Cortet et al. (2009). Rycroft et al. performed 3D Discrete Element Method (DEM) simulations of tall and wide silo drainage, as well as a pushing simulation in which half of the domain is moved upwards. All three systems are periodic along one of their axes. Cortet et al. performed 2D DEM simulations of a rotating drum filled with disks. A novel contribution of the work presented here is the use of data from 3D DEM simulations of a rotating drum to investigate Jop et al.'s law.

Scaling laws for granular systems are also investigated. The scaling between the thickness and the flux in the middle of the downwards-flowing layer is key to understanding the dynamics of the system. Various methods for calculating the thickness-flux scaling are compared. Also studied is the scaling between the flux through the flowing layer and the angle it makes with the horizontal. This relation has been used to derive a friction law (Pouliquen, 1999). Both of the scaling laws require knowledge of the location of the equilibrium surface, which is the boundary between upward and downward flow, and the free surface, which is the surface created by the top-most layer of particles in the system. Novel procedures for finding these surfaces are proposed here.

The thesis is arranged as follows. A review of the literature on dense granular flow is given in Chapter 2. An overview of DEM is given in Chapter 3. Chapter 4 focuses on the continuum theory of granular fluids. A derivation of the constitutive law for an isotropic and incompressible fluid is provided and a number of existing constitutive laws are outlined. The constitutive law of Jop et al. (2006) is covered in some detail. The homogenization techniques used to obtain kinetic and kinematic measures are described in Chapter 5. The methods for approximating features of the flow field as well as the packing fraction (volume fraction) of the particles in the system are also provided. The assumptions of isotropy and incompressibility in the constitutive laws are investigated in Chapter 6. The forms of the friction coefficient and the packing fraction are also explored. Scaling laws are investigated in Chapter 7. Conclusions and recommendations are presented in Chapter 8.

2

LITERATURE REVIEW

2.1 INTRODUCTION

Ralph Alger Bagnold is considered to be a pioneer of desert exploration. During his time in the desert of North Africa in the 1930s he made a number of significant observations which were later included in his book *The Physics of blown sand and desert dunes* (Bagnold, 1954b). His work was the first to propose a constitutive law for a granular fluid based on the kinetic theory of gases. In acknowledgement of the immense contribution of his work towards granular flow and the physics of sand dunes, a field of dunes on the surface of Mars was named after him.

Subsequent work on the kinetic theory of Bagnold has shown that it is only applicable to highly kinetic systems, which mimic gases. The focus of the present work is on rapid-dense flow of granular materials. These are systems in which the particles flow more slowly than in kinetic systems. This literature review covers the more recent work on rapid-dense granular flow, with a focus on the constitutive laws that have been developed and the work on flow in rotating drums and tumbling mills. Special attention is also given to the scaling laws governing the flows in such systems.

This chapter is arranged as follows. The categorization of flow in rotating drums and tumbling mills is given in Section 2.2. Bagnold's kinetic theory and subsequent work is summarized in Section 2.3. A review of the numerical simulation of granular systems is given in Section 2.4. The literature on granular rheology is reviewed in Section 2.5. Scaling laws are discussed in Section 2.6.

2.2 FLOW IN ROTATING DRUMS AND TUMBLING MILLS

The flow of granular material in rotating drums is central to this thesis. This section provides background on the flow regimes and features of the flow field. Flows of dry particles in rotating drums exhibit all of the features that have been observed in granular systems. This includes solid-, liquid- and gas-like behaviour. The flow-regimes can be divided into six categories according to rotational speed, as shown in Figure 2.1. At low speeds, Figure 2.1 (a) and (b), the flow is not continuous, with slumping (avalanches) occurring intermittently. The frequency of slumping is dependent on the rotational speed and the size and diameter of the particles (Mellmann, 2001; Henein et al., 1983). The flows of particles during the avalanches are similar to heap flows (GDR MiDi, 2004; Pont et al., 2003). At higher speeds, Figure 2.1 (c) to (f), the downward flow in a rotating drum becomes continuous. The particles start centrifuging at very high speeds, Figure 2.1 (f).

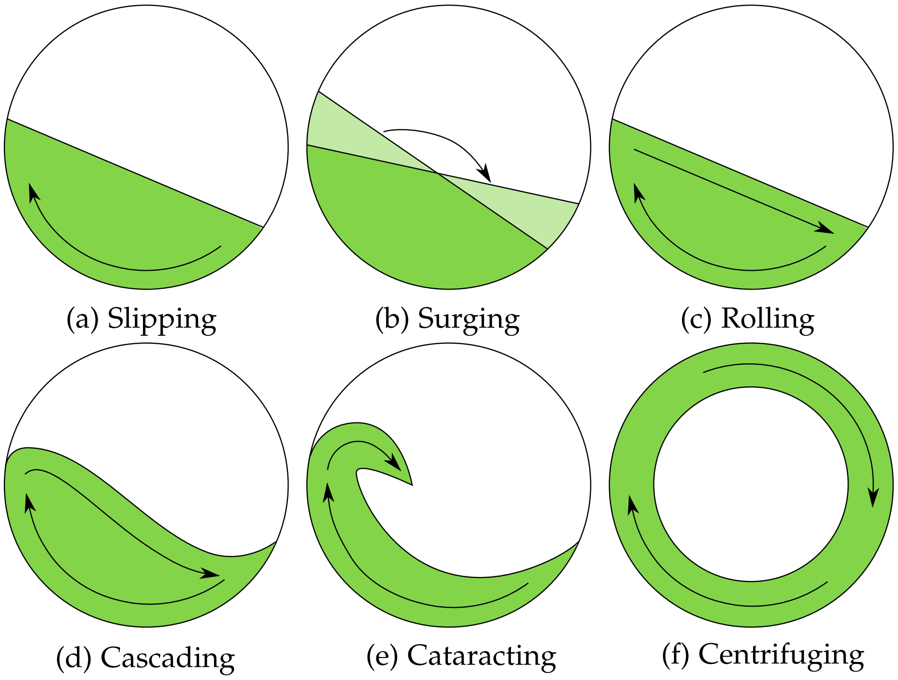
(a) Slipping
(b) Surging
(c) Rolling
(d) Cascading
(e) Cataracting
(f) Centrifuging

Figure 2.1: Six categories of granular flow in rotating drums. Schematics (a) through (f) depict the flow profiles with increasing rotational speed.

The flow in rotating drums is often described by (a) a surface layer (called the free surface) flowing over a densely packed en-masse layer that is considered static relative to the rotating drum; and (b) an internal layer, marking the boundary between rising and falling flow, called the equilibrium surface. Figure 2.2 shows the regions of flow that are typically studied in the rolling, cascading and cataracting regimes. These schematics are based on those of the Groupement de Recherche Milieux Divisés (GDR MiDi, 2004). The upward-flow of material is considered to be static (plug flow) relative to the drum. The downward flow ranges from quasi-static, near the equilibrium-surface, to rapid dense (liquid-like) flow at the free surface. The velocity in the flowing layer decreases approximately linearly with distance from the free-surface until it reaches the quasi-static region, where it decreases exponentially to zero at the equilibrium surface. Beyond the equilibrium surface, the velocity increases linearly up to the boundary where it approaches the velocity of the drum. The free flowing layer, the liquid-like linear region just below the free-surface, has particles interacting by frictional and collisional contacts (Pouliquen et al., 2002; GDR MiDi, 2004; Forterre et al., 2008). The bulk deformations in the quasi-static (exponential) region are slow and the particles interact mostly by frictional contact (Roux et al., 2002). Cascading and cataracting regimes will additionally have a highly-kinetic (gas-like) cataracting region above the free surface (Goldhirsch, 2003). The volume of material in the gas-like region increases with rotational speed.

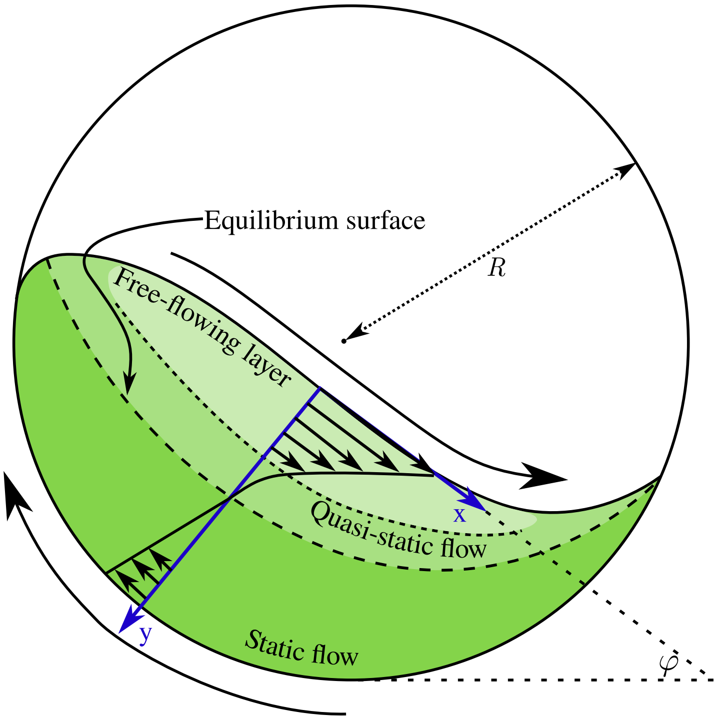

Figure 2.2: Regions of flow in a rolling or cascading rotating drum. R is the radius of the drum, the orthonormal coordinate system (x, y) used in some scaling laws is shown in blue. Lastly, the angle of repose φ is shown.

A rotating drum that is widely used industrially is the tumbling mill, which is used to grind granular media. Metal balls are used to aid the grinding process in certain types of mills. Radially arranged lifters, parallel to the axis of rotation, often line the inside of the drum. The lifters are intended to increase efficiency of the machine by increasing the effective friction on the inside wall of the mill. Tumbling mills are often run at a high speed with cataracting flows, see Figure 2.1 (e).

In rapidly-rotating tumbling mills and drums there are a number of scalar features as well as a set of surfaces that divide the bed into regions with distinct granular behaviour in the profile of the flow. Figure 2.3 illustrates some of these features:

- The **bed free surface** is the surface created of the uppermost particles in the bed.
- The **bulk free surface** is the surface below which the particles are constantly in contact.

- The **departure shoulder** is defined as the point at which the rising region leaves the wall of the drum, previously this has been called the shoulder (Powell et al., 2004).
- The **bulk shoulder** is the point at which the bulk free surface and equilibrium surface intersect.
- The **head** is the highest point on the bed free surface.
- The **centre of circulation** is the only stationary point in the bed.

The region bounded by the bulk and bed free surfaces contains particles that are in free fall, flowing in a gas-like manner with contacts between particles being infrequent and elastic. For slower mill speeds the free-fall region is negligible and the bulk and bed free surfaces will coincide.

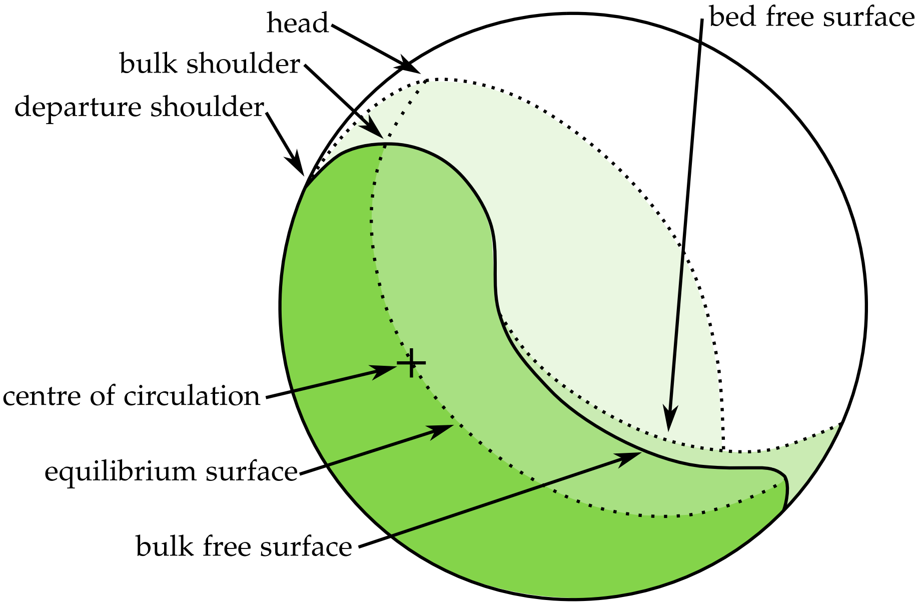

Figure 2.3: Surfaces and regions in a continuously-flowing mills and rotating drums.

As mentioned in Chapter 1, the low efficiency of industrial mills provides a strong need for improving the understanding of granular flows in rotating drums. This need forms part of the motivation for this thesis.

2.3 KINETIC THEORY

Bagnold's kinetic theory is not investigated in this thesis; this section is included due to its historical importance. The theory was based upon the results of annular shear cell experiments on a system with particles made of paraffin wax and lead stearate in a fluid of glycerine, water and alcohol (Bagnold, 1954a). For particle inertia-dominated flows, the shear component of the stress, denoted σ_{xy} in their coordinate system, was found to have a quadratic dependence on the shear rate (velocity gradient) $\frac{\partial v_x}{\partial y}$, given by

$$\sigma_{xy} = \chi(\lambda)\rho_p d^2 \left(\frac{\partial v_x}{\partial y}\right)^2, \tag{2.1}$$

where $\chi(\lambda)$ is a function of the inter-particle spacing, ρ_p is the density of the particles and d is the diameter of the particles.

The kinetic theory assumes that the inter-particle collisions are elastic and that friction between particles is negligible. Ogawa et al. (1980) derived constitutive relations for kinetic granular systems. The constitutive relations have the same quadratic form as Bagnold's, which was obtained semi-empirically. Savage et al. (1981) presented a theory of the stress in rapidly shearing granular materials[1]. Ding et al. (1990) used the kinetic theory of granular flow to derive a model of two-phase flow for a fluidized bed. When compared with data from 2D fluidized bed experiments, the model predicted the time-averaged porosity correctly. Ancey et al. (1999) examined the bulk stress for granular suspensions. In suspensions, the bulk stress has a fluid component in addition to a component arising from the inter-particle forces. They observed a mismatch in bulk and true dissipation rates. The bulk dissipation rate is the rate at which energy is dissipated in the bulk and the true dissipation rate is the rate for net energy dissipation for the whole system. Ancey et al. found that the true dissipation rate can only be the same as the bulk dissipation rate if the dissipation rate due to contacting particles is negligible. This observation led them to question the validity of other energy-based computations of the bulk viscosity for suspensions.

Jenkins et al. (2002) proposed a kinetic theory that takes frictional interactions into account. The theory compared well with numerical simulations of a shear cell containing inelastic frictional spheres.

Rajchenbach (2004) emphasized the inapplicability of the Bagnoldian and kinetic theories to dense flow. It was argued that in dense flows the main means of particle interaction is not elastic collisions, and the transport of momentum is mainly by pressure waves (sound) passing through the network of contacting particles. Lois et al. (2006) tested the binary collision assumption. They show that the formation of multi-contact clusters lead directly to the breakdown of the binary collision assumption.

Bagnold's kinetic theory, while historically significant, has been shown to be inaccurate for dense flows. The key assumption that the particles are contacting via elastic collisions no longer holds for dense flows with continuously contacting particles. The theory will therefore not be investigated in this thesis.

---

[1] A detailed review of granular flow modelling up to 1984 was given by Savage (1984).

2.4 SIMULATION

The simulations done in this thesis model numerically the individual particles of the system. The first mention of a simulation of a granular system was given in Cundall (1971). In a more detailed paper Cundall et al. (1979) described the method of simulating "distinct" contacting particles that interact via a contact law. Originally called the Distinct Element Method by Cundall et al., the method is now also known as the Discrete Element Method (DEM). A number of advances in algorithms has enabled DEM simulations to be run in a highly-efficient manner (Bonet et al., 1991). In addition to the algorithmic advances, the rapid increase in computing power has enabled full-scale simulations of tumbling mills containing millions of particles (Cleary et al., 2015a; Cleary et al., 2015b). The computing power of Graphic Processing Units (GPUs) has been used to speed up significantly the DEM simulations of rotating drums (Hromnik, 2013).

In rotating drums, the DEM has been found to match experimental results relatively well. Yamane et al. (1998) compared experimental results, obtained using the Magnetic Resonance Imaging (MRI) technique of Nakagawa et al. (1993) with mustard seeds in a rotating drum, with numerical results obtained from DEM simulations. They noted differences in the shape of the free surface. Yang et al. (2003) found good agreement when comparing results from PEPT experiments with DEM simulations. They concluded that DEM is an "effective and reliable" technique for studying the microdynamics in a rotating drum. McCarthy et al. (2010) did a quantitative validation of DEM by comparing simulations with an experimental annular shear cell. They observed that very accurate representations of the shape of the particle were needed in the simulations in order to match the experimental measurements exactly. Govender et al. detailed an X-ray technique for tracking a tagged plastic bead in an experimental mill[2]. The resulting data were compared to DEM simulations by McBride et al. (2004). McBride et al. observed differences in the head and toe regions of flow. The literature mentioned here shows that DEM can be tweaked to match experimental data exactly and accurately models the microdynamics of real particles.

Rycroft et al. (2009) and Cortet et al. (2009) investigated constitutive laws of dense granular flows in, respectively, silo drainage and pushing simulations and simulations of a 2D rotating drum. In addition, they discussed the limitations and artifices of 2D DEM. More details on these works are given in Section 2.5.

DEM simulations of rotating drum systems have been shown to be an effective proxy for the physical systems. An important benefit of numerical systems over physical experiments is the knowledge of the

---

[2] More details can be found in Govender (2005).

force between the particles. As a consequence the stress field can be calculated, which is key to understanding constitutive laws.

2.5 GRANULAR RHEOLOGY

In this section some context on the development of the 3D constitutive law of Jop et al. is presented. Literature covering the assessment of the constitutive law is also presented. In experiments of granular flows down inclined planes, Pouliquen (1999) found the scaling given by

$$\frac{u}{\sqrt{gh}} \propto \frac{h}{h_{\text{stop}}(\varphi)}, \tag{2.2}$$

where u and h are the depth-averaged velocity and the height of the flowing layer, respectively. For each experiment, for some value of φ, Pouliquen would stop the source of flow and measure the thickness of the flowing layer once it had come to rest. This thickness is expressed as $h_{\text{stop}}(\varphi)$ in Equation 2.2. The threshold angle φ was taken to be related to a frictional threshold. Pouliquen proposed a friction law using the frictional threshold with a depth-averaged force balance through the flowing layer.

GDR MiDi (2004) suggested that the friction is dependent on the dimensionless rescaled shear rate

$$I = \dot{\gamma} d \sqrt{\frac{\rho_p}{p}}\,, \tag{2.3}$$

where $\dot{\gamma}$ is the shear rate and p is the hydrostatic pressure.

The rescaled shear rate I is interpreted as a ratio of two different time scales

$$I = \frac{T_p}{T_\gamma}. \tag{2.4}$$

Consider a layer of particles flowing over another layer, the top layer will be going through a cycle of “climbing” over the particles on the bottom layer and falling back down again. The confinement timescale T_p is the approximate time taken for the top layer to fall back down onto the bottom layer

$$T_p = d\sqrt{\frac{\rho_p}{p}}. \tag{2.5}$$

The typical time of deformation T_γ is the time taken for the top layer to move the distance d over the bottom layer

$$T_\gamma = \frac{1}{\dot{\gamma}}. \tag{2.6}$$

In 2D DEM simulations of disks undergoing shear deformation, da Cruz et al. (2005) confirmed that the state of a granular medium can be determined by I, which they named the *inertial number*. Small values of the inertial number ($I < 10^{-2}$) correspond to quasi-static flows. Likewise large values ($I > 0.2$) correspond to the collisional (gaseous) regime. The regime of (liquid-like) dense granular flow corresponds to the middle range of inertial numbers ($10^{-2} < I < 0.2$). da Cruz et al. (2005) found that both the effective friction μ and the packing fraction (solids fraction) ϕ, which is the proportion of the total volume occupied by the particles, have a linear dependence on the inertial number I given by

$$\phi(I) = \phi_{\max} - aI, \tag{2.7}$$

$$\mu(I) = \mu_{\min} + bI, \tag{2.8}$$

with constants $\phi_{\max} \simeq 0.81$, $a \simeq 0.3$, $\mu_{\min} \simeq 0.25$ and $b \simeq 1.1$.

Jop et al. (2005) performed experiments of particles flowing down channels of varying width. Like da Cruz et al. (2005) they found that the effective friction μ is dependent on I, but unlike the linear dependence of da Cruz et al. (2005) they found the effective friction μ followed the sigmoidal curve

$$\mu(I) = \mu_1 + \frac{\mu_2 - \mu_1}{I_0/I + 1}, \tag{2.9}$$

with constants $\mu_1 = \tan(20.9^\circ)$, $\mu_2 = \tan(32.76^\circ)$ and $I_0 = 0.279$.

Jop et al. (2006) generalized the constitutive law for dense granular flow to three dimensions and used it to perform finite-difference simulations of flow down a channel. The 3D constitutive equation is given by

$$\boldsymbol{\tau} = \mu(I)\frac{p}{|\dot{\gamma}|_J}\dot{\gamma}, \tag{2.10}$$

where the shear rate is given by twice the symmetric velocity gradient as

$$\dot{\gamma} = \frac{\partial \boldsymbol{v}}{\partial \boldsymbol{x}} + \frac{\partial \boldsymbol{v}}{\partial \boldsymbol{x}}^T. \tag{2.11}$$

The norm of the shear rate is non-standard and is given by

$$|\dot{\gamma}|_J := \sqrt{\frac{1}{2}\dot{\gamma}_{ij}\dot{\gamma}_{ij}}. \tag{2.12}$$

The friction coefficient $\mu(I)$ in Equation 2.10 is of the same form as Equation 2.9 and the shear stress tensor $\boldsymbol{\tau}$ is the deviatoric (volume preserving) component of the stress tensor $\boldsymbol{\sigma}$ given by

$$\boldsymbol{\tau} = \boldsymbol{\sigma} + p\boldsymbol{I}, \tag{2.13}$$

where $\boldsymbol{I}$ is the second-order identity tensor and the pressure $p := -1/3\mathrm{tr}\boldsymbol{\sigma}$. Note here that the usual sign convention for fluid mechanics is taken where tension is a positive stress and compression a negative stress. Jop et al. redefined the inertial number in 3D as

$$I = |\dot{\gamma}|_J d\sqrt{\frac{\rho_p}{p}}. \tag{2.14}$$

Jop et al. found that the velocity at the free surface of chute-flow experiments agreed well with the finite-difference simulations that used the generalized law. Two key assumptions that are necessary for the constitutive law are:

1. The change in the packing fraction ϕ is negligible, which makes the flow incompressible.
2. The shear stress $\boldsymbol{\tau}$ and shear rate $\dot{\gamma}$ tensors are scalar multiples of one another, i. e. colinear.

Forterre et al. (2008) presented a review of current understanding of dense granular flow with focus on constitutive equations. They give the key limitations of the constitutive law of Jop et al. (2006) as:

- The lack of a microscopic explanation of the law.
- The inability of the law to accurately describe flows approaching the quasi-static limit.
- Hysteresis effects in the threshold between phases of flow.
- The inability to describe flows approaching the kinetic regime.

A Coulomb material has the same form as Equation 2.10, but with constant μ. Schaeffer (1987) showed that a Coulomb material with a von Mises yield criterion (a threshold for the von Mises stress, a multiaxial measure of stress) is ill-posed sometimes in 3D and always in 2D. Barker et al. (2015) showed that in 2D Jop et al.'s rheology is ill-posed for high and low inertial numbers and well-posed for intermediate values. Ill-posed in this case is defined as an instability in numerical solutions. They use numerical error analysis techniques to show that for a given resolution a standard numerical scheme is unstable in the ill-posed parameter space. Based on the findings of Schaeffer (1987), Barker et al. (2015) also suggest, but do not prove, that in 3D Jop et al.'s rheology is likely to be better posed, but "zones of ill-posedness" are still expected.

Lagrée et al. (2011) used a numerical Navier-Stokes solver with Jop et al.'s rheology to solve 2D granular collapse problems. The numerical results were found to agree with with analytical and DEM results. Staron et al. (2012) used the numerical solver of Lagrée et al. (2011) to simulate 2D silo drainage. They showed that the numerical solver could be used to capture the phenomenon of a low-pressure cavity forming at the opening of the silo. Barker et al. (2015) observed that the results of Lagrée et al. (2011) and Staron et al. (2012) may not display the expected zones of ill-posedness due to the ad-hoc regularizations introduced into the numerical solver to avoid the singularity at low strain rates.

Cortet et al. (2009) performed 2D DEM simulations of slowly rotating drums filled with disks. They investigated the assumption of colinearity between the shear stress $\boldsymbol{\tau}$ and the deviatoric (volume preserving) part of the shear rate $\dot{\gamma}$ tensors for the constitutive law of Jop et al. (2006). These quantities were obtained by splitting the domain into a number of bins and averaging over the particles inside each bin. The quantities in each element were averaged over 400 evenly spaced temporal "snapshots", which together constituted a single rotation of the drum. In order for the colinearity condition to be satisfied, the principle directions of $\boldsymbol{\tau}$ and $\dot{\gamma}$ need to be aligned. They found that the angular difference in alignment between $\boldsymbol{\tau}$ and $\dot{\gamma}$ ranged from -10° to 10° in the flowing layer, which flows more rapidly ($5 \times 10^{-4} < I < 5 \times 10^{-2}$). In the quasi static region below the flowing layer (with $10^{-6} < I < 5 \times 10^{-4}$) the misalignment increased to 35°. Figure 2.4 shows the angular difference between $\boldsymbol{\tau}$ and $\dot{\gamma}$ throughout the drum. The misalignment is attributed to "transient dilatancy effects" in the slowly deforming regions of the drum. They also investigated the effective friction $\mu(I)$ of Jop et al. (2006). Despite the misalignment between $\boldsymbol{\tau}$ and $\dot{\gamma}$, the scalar effective friction $\mu = |\boldsymbol{\tau}|/p$ agrees reasonably well with the Jop et al. rheology, even in regions where the inertial number is very small ($I \sim 10^{-5}$) and the misalignment is quite large.

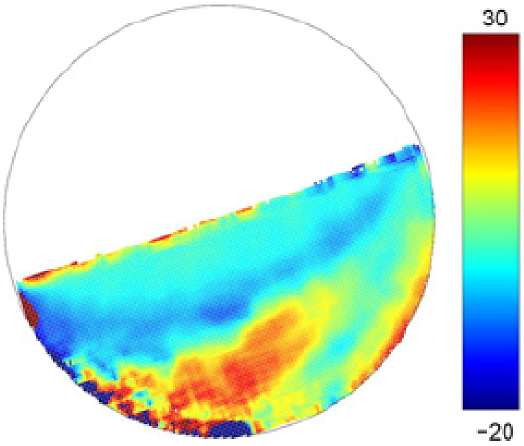

Figure 2.4: Angular difference between the principle directions of $\boldsymbol{\tau}$ and $\dot{\gamma}$ for a drum rotating at 12 rpm. Obtained from Cortet et al. (2009).

Rycroft et al. (2009) performed 3D DEM simulations of particles draining out of tall and wide silos. They also performed a pushing simulation, where half of the domain was forced upwards, on the wide silo. They investigated the applicability of continuum descriptions of flow in spatial (Eulerian) and material (Lagrangian) settings. In both cases continuum measures are taken by averaging over rectangular volumetric elements. The Eulerian elements were static, while the Lagrangian elements moved at the mean velocity of the particles therein. Like Cortet et al. (2009), they studied the alignment between the principle directions of the deviator of the shear rate and the shear stress tensors. They found that the average misalignment, over a single snapshot, between the tensors was 12°. If the quantities were averaged over a "window" of 20 temporal snapshots the average misalignment decreased to 6.7°. They also found a linear relationship between the packing fraction ϕ and inertial number I ($\phi(I) = 0.635 - 8.13I$), which agreed with the results of da Cruz et al. (2005)[3].

Pignatel et al. (2012) performed quasi-2D experiments of rotating drums and found a disagreement between the measured effective friction and that predicted by the constitutive equation of Jop et al. (2006). The discrepancy was attributed to the influence from the side-walls of the rotating drum.

Hatano (2007) performed DEM simulation of two periodic sheared systems of different sizes. It was shown that the dilatancy ϕ has a power-law dependence on the inertial number

$$\phi(I) = a - bI^{c}, \tag{2.15}$$

with constants $b \approx 0.11$ and $c = 0.56 \pm 0.02$. a was estimated by extrapolation.

Lee et al. (2012) used the dilatancy law of Hatano (2007) to develop a constitutive model that accounts for hysteresis in the transition from quasi-static to rapid-dense flows.

An empirically-derived exponential law for the packing fraction, based on PEPT experiments, was proposed by Pathmathas (2015). PEPT is a technique to track a particle tagged with a radioactive tracer (Parker et al., 1993). The proposed law is given by

$$\phi(I) = I_0 e^{-bI^{c}}. \tag{2.16}$$

The validation of the constitutive law of Jop et al. is a central goal in this thesis. The applicability of the law is bounded at low inertial numbers by the hysteresis in the phase transition from liquid- to solid-like flows. At high inertial numbers, the law is unable to capture highly kinetic flows. The rapidly rotating drum system simulated in this thesis has flows with a wide range of inertial numbers, varying from quasi-static to rapid-dense; this allows for a comprehensive assessment of the law. The assumptions of incompressibility and isotropy are key to the law. While the DEM simulations of Rycroft et al. (2009) and Cortet et al. (2009) allowed for an investigation of these assumptions for 3D silo drainage and 2D rotating drum systems; this has not yet been done for 3D simulations of a rotating drum. This thesis is intended to address this gap in the literature.

---

[3] An excellent review of the recent progress of work on rheology of dense granular flow is given in Jop (2015).

2.6 SCALING

Scaling laws relate non-dimensional quantities in a system. They are important as they provide constraints to the possible form of a constitutive law. The $\mu(I)$ friction law described in the previous section is a key scaling relation for determining the constitutive form for the shear stress $\boldsymbol{\tau}$. The literature covering two scaling laws that are investigated in this thesis is outlined in this section.

2.6.1 *Flowing-layer thickness*

The relationship between the velocity and thickness in a layer of flowing granular material is a key scaling for understanding the dynamical behaviour of the system. When investigating the flowing layer in heap flow and rotating drums, a coordinate system perpendicular to the flowing layer is typically used, shown in Figure 2.2. The following assumptions are generally made about the flow in a rotating drum when formulating scaling relations: (a) there is a constant angle of repose of the bed, (b) the flow is not cascading or cataracting, (c) the thickness of the flowing layer (h) is small relative to the radius of the drum, i.e. $h^2 \ll R^2$, and (d) the rising region has flux per unit length of drum defined by $Q_r = \left(\frac{\omega}{2}\right)\left[R^2 - h^2\right] \approx \left(\frac{\omega}{2}\right) R^2$, where ω is the angular velocity of the drum. In addition, some studies on rotating drum systems that are very narrow along the axis of rotation make the assumption that the side walls have no influence on the scaling relation.

Parker et al. (1997) observed in a series of PEPT experiments of a rotating drum that the flowing layer is roughly two-thirds as thick as the static layer, regardless of speed. Orpe et al. (2001) carried out experiments on a variety of different particles in a thin rotating drum. Their results showed that the average of the component of velocity tangential to the flowing layer is proportional to the cube of the flowing layer thickness, i.e. $\langle v \rangle \propto h^3$. In experiments of flows down a rough inclined channel, Ancey (2002) emphasized that the velocity profiles measured at the side-walls are strongly disturbed. Ancey described two different flow-regimes that are dependent on the Froude number F_r. Above some critical value of F_r the flow has a linear velocity profile. Below this, a convex velocity profile with a constant mean velocity was observed. The heap flow and rotating drum experiments of GDR MiDi (2004) indicated a linear scaling, i.e. $\langle v \rangle \propto h^1$. From experiments on flow down a chute, Jop et al. (2006) also concluded that there is a linear scaling, and that the distance between the side-walls affects the thickness of the flowing layer.

Félix et al. (2007) ran experiments with various drum and particle sizes. They found the scaling exponent n, where $\langle v \rangle \propto h^n$, to be dependent on the ratio of drum radius to particle size. The scaling expo-

AUTHOR	SCALING: $\langle v \rangle$ VS h	$\lvert\dot{\gamma}\rvert$ ESTIMATE	COMMENT
Parker et al. (1997)	$\langle v \rangle \approx h^0$	≈ 0	wall slip
Orpe et al. (2001)	$\langle v \rangle \approx h^3$	$\sqrt{\frac{g\omega}{Md\cos(\theta)}}$	θ is the dynamic angle of repose of bed, M is a fit parameter
GDR MiDi (2004)	$\langle v \rangle \approx h^1$	$0.5\sqrt{\frac{g}{d}}$	
Jop et al. (2006)	$\langle v \rangle \approx h^{3/2}$	dependent on Q^*	based on chute flows
Félix et al. (2007)	$\langle v \rangle \approx h^{5.5\pm0.5}$	variable	$D/d = 100$, narrow drum end-wall effects likely
Pignatel et al. (2012)	$\langle v \rangle \approx h^{1.27}$	variable	quasi-2D. Best fit from all data
Pathmathas (2015)	$\langle v \rangle \approx h^{0.86\pm0.04}$	$\dot{\gamma} \approx 0.25\sqrt{g}\langle d \rangle$e	cataracting flows
Govender et al. (2016)	$\langle v \rangle \approx h^{0.997\pm0.027}$	$(0.620 \pm 0.225)\sqrt{\frac{g}{d}}$	

Table 2.1: An overview of previous works on scaling laws for rotating drums and flow down a heap.

nent n was found to range from 5 to 0.5 corresponding to small and large size-ratios, respectively. Pignatel et al. (2012) found that

$$\frac{h}{d} \approx 2.86 \left(\frac{\langle v \rangle h}{d\sqrt{dg}} \right)^{0.44}, \tag{2.17}$$

where the dimensionless flow rate $Q^* := \frac{\langle v \rangle h}{d\sqrt{gd}}$. Rearranging Equation 2.17 gives $\langle v \rangle \approx h^{1.27}$. In addition Pignatel et al. concluded that the side-walls affect the flowing layer thickness.

Govender et al. (2016) performed PEPT experiments on rotating drums with and without lifter bars. They found an approximately linear scaling ($\langle v \rangle \propto h^{0.997\pm0.027}$) from measurements of multiple slices through the flowing layer for both cases. Table 2.1 summarizes key information of works done on scaling laws.

2.6.2 *Dynamic angle of repose*

Another scaling relation investigated in the literature is the relationship between the angular speed ω and the dynamic angle of repose φ. The dynamic angle of repose is the angle that the free surface makes with the horizontal (see Figure 2.2). Rajchenbach (1990) found the scaling to be $\varphi \propto \omega^2$. Dury et al. (1998) performed a number of experiments and simulations of rotating drums. The experiments were performed using MRI with mustard seeds as particles. They found a linear scaling, i.e. $\varphi \propto \omega$. GDR MiDi (2004) found that the degree of dependence of φ on the flux, which is proportional to the speed, was inversely proportional to the axial-width of the drum. A very wide drum was found to have an almost constant repose and a narrow drum a strong dependence on the flux.

At high speeds the free surface has a curved shape, which makes the repose angle difficult to define uniquely. Govender et al. (2016) proposed redefining the dynamic angle of repose as the angle between the horizontal and the semi-major axis of the ellipse that best fits the equilibrium surface. This definition provides an unambiguous way of finding the repose even for cataracting flows. A flow field with the fitted ellipse is shown in Figure 2.5. To fit the ellipse they used the algorithm of Fitzgibbon (1998).

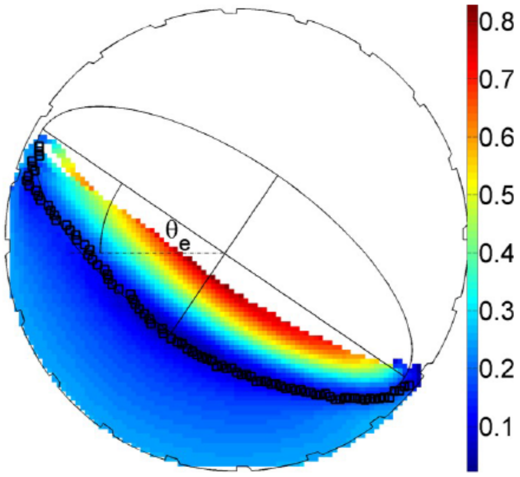

Figure 2.5: Time-averaged speed, obtained with PEPT, of 5mm beads in a 300mm drum with lifters rotating at 15.4 revolutions per minute (rpm). The black squares show the equilibrium surface. A fitted ellipse with the dynamic angle of repose θ_e is shown. Obtained from Govender et al. (2016).

2.6.3 *Summary*

In addition to the assessing the constitutive law of Jop et al.; this thesis is intended to supplement the above-mentioned literature with an assessment of the scaling laws over a wide range of flow-regimes. There is little agreement in the literature on the scaling relation between the thickness of a granular layer flowing down a slope and the flux. The most promising seems to be a linear scaling relation, as it has been found in a number of separate studies. In the scaling between the dynamic angle of repose and the flux in the rising layer GDR MiDi (2004) found that the degree of dependence of the repose angle on the flux was inversely proportional to the axial width of the drum. The simulations done in this thesis model a drum that is periodic along the axis of rotation; this will provide data on the limiting case of GDR MiDi's scaling law, an infinitely long drum.

2.7 SUMMARY

In the continuously-flowing regimes the rotating drum system can contain regions of flow ranging from quasi-static (solid-like) to highly kinetic (liquid- and gas-like) flows. DEM simulations are of great value as, unlike other experimental methods, they allow kinetic quantities such as the force between particles and the stress to be calculated over the entire flow-field. To date there has been no assessment of the constitutive law of Jop et al. (2006) using 3D DEM simulations of rapidly-rotating drums, a central aim of this thesis is to provide this assessment. In addition, the wide range of simulation speeds in this work will provide new insight into the velocity-thickness and repose-angle scaling laws.

From an industrial perspective, the design of efficient industrial mills would require rapid prototyping. The prototyping would need to be done using simulations. If Jop et al.'s constitutive law is accurate, the simulations may be done using a fluid model and finite-element or finite-difference methods. The influence of liquid in an industrial mill may mean a similar study on suspensions is needed first, however. Interestingly, some granular suspension literature also make the assumption of isotropy and incompressibility for the constitutive law (Boyer et al., 2011; Trulsson et al., 2012). The results of the assessment of these assumptions in this work may imply that assumptions for granular suspensions also need to be questioned in a similar manner.

3

MICRO-SCALE MODEL

3.1 INTRODUCTION

Emergent phenomena are those complex phenomena that arise out of a collection of smaller, simpler, entities. The phenomena observed in granular materials, such as hysteresis and segregation, are examples of emergence. It is from the relatively simple interactions between particles at the microscopic scale that these phenomena, at the mesoscopic scale, arise. The mesoscopic scale is the intermediate scale between the micro- and macro-scales. The 3D rotating drum simulations that are analyzed in this thesis are performed using the Discrete Element Method (DEM), which uses a model of these simple interactions at the micro scale. These simulations are the focus of this chapter.

An overview of this chapter is as follows. An outline of the DEM, based on an explicit time-integration scheme, is given in Section 3.2 A detailed derivation of a model of contact that takes into account the history of contact is given in Section 3.3. Details on the hardware, software and configuration of the simulations of a rotating drum that are performed for this work are given in Section 3.4.

3.2 DISCRETE ELEMENT METHOD

The simulations in this thesis are performed with the DEM. As previously mentioned, the DEM is a numerical method used to model systems of particles in contact with one another. It was originally developed by Cundall (1971) for the analysis of rock mechanics problems. Consider a system of N particles, the total force $\boldsymbol{F}^i$ on a particle i can be expressed as the sum of the forces applied by the particles it is in contact with, i.e.

$$\boldsymbol{F}^i = \sum_{\alpha=1}^{N_c} \boldsymbol{F}_\alpha + m^i \boldsymbol{g}, \quad \boldsymbol{t}^i = \boldsymbol{\mathcal{I}}^i \boldsymbol{\alpha}^i, \tag{3.1}$$

where $\boldsymbol{F}_\alpha$ is the force applied by contact α, $\boldsymbol{g}$ is acceleration due to gravity and m^i, $\boldsymbol{t}^i$, $\boldsymbol{\mathcal{I}}^i$, $\boldsymbol{\alpha}^i$ and N_c are, respectively, the mass, torque applied, moment of inertia tensor, angular acceleration and number of contacts for particle i. The contact law, to calculate the force, is described in Section 3.3. After dividing the equation on the left by m^i the system becomes

$$\frac{\boldsymbol{F}^i}{m^i} = \boldsymbol{a}^i = \sum_{\alpha=1}^{N_c} \frac{\boldsymbol{F}_\alpha}{m^i} + \boldsymbol{g}, \quad \boldsymbol{t}^i = \boldsymbol{\mathcal{I}}^i \boldsymbol{\alpha}^i, \tag{3.2}$$

where $\boldsymbol{a}^i$ is the linear acceleration of particle i. Finite-difference methods (e. g. forward-Euler, backward-Euler etc.) can be used to approximate the solution to the above system of equations.

A forward-Euler approximation is explicit and conditionally stable. The critical value of the timestep Δt is related to the minimum eigenperiod of the system (Chareyre et al., 2005). In systems with large numbers of particles the minimum eigenperiod is difficult to calculate. The critical timestep is approximated by considering the speed of pressure waves that propagate throughout the system (Yade Authors, 2016). For a system of spheres the approximated critical timestep is given as

$$\Delta t_{cr} = \min_i R^i \sqrt{\frac{{\rho_p}^i}{E_y^i}}, \tag{3.3}$$

where E_y^i is the Young's modulus of particle i. A timestep of $\Delta t = 0.3\Delta t_{cr}$ should be used to guarantee stability (Yade Authors, 2016).

The algorithm using the aforementioned approximations for simulating a system of particles is summarized in Algorithm 1.

Algorithm 1 Outline of the procedure for the Discrete Element Method (DEM).

1. Start with a set of particles $i \in [1, \cdots, N]$ with some initial position $\boldsymbol{X}^i$, linear velocity $\boldsymbol{v}^i$ and angular velocity $\boldsymbol{\omega}^i$.
2. Step through time with a time-step Δt satisfying the constraint given in Equation 3.3. At each timestep the following is done:
    a) The particles that are in contact with one another are determined.
    b) The forces between particles in contact are determined. This can be made up of frictional and elastic components, and may depend on the history of the contact. More detail on the contact law is given in Section 3.3.
    c) Newton's second law is used to obtain the linear and angular acceleration of each particle from the forces.
    d) The displacements and linear and angular velocities of all of the particles are updated.

The contact detection step in Algorithm 1 is relatively computationally expensive, however it is not necessary at every time-step. Contact detection can be skipped if it is known that no new contacts have been made. The rate of change of contacts can be approximated by the speed of all the particles. Faster particles will change contacts more rapidly and contact detection will have to occur more frequently when compared to slow-moving particles.

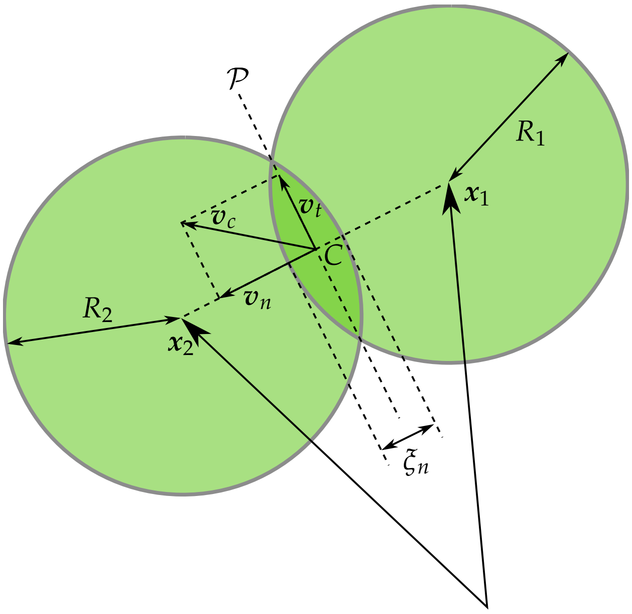

Figure 3.1: Diagram for two spherical particles in contact.

3.3 VISCOELASTIC CONTACT LAW

The contact law used in the simulations is described in this section. Contact laws between two contacting particles typically make use of the decomposition of the force $\boldsymbol{f}$ given by

$$\boldsymbol{f} = \boldsymbol{\phi}_n + \boldsymbol{\phi}_t, \tag{3.4}$$

where $\boldsymbol{\phi}_n$ and $\boldsymbol{\phi}_t$ are, respectively, the components of the force normal- and tangential to the surface at the point of contact. In this thesis the particles are identical frictional spheres with properties intended to approximate that of glass beads. A soft model of contact is used to allow for overlap between contacting particles. Consider two contacting spherical particles G_1 and G_2, as shown in Figure 3.1. The overlap $\boldsymbol{\xi}$ is defined as the solution, with initial condition $\boldsymbol{\xi}|_{t=0} = \mathbf{0}$, of the following differential equation (Pournin, 2005)

$$\dot{\boldsymbol{\xi}} = (\boldsymbol{e}_n \times \dot{\boldsymbol{e}}_n) \times \boldsymbol{\xi} - \boldsymbol{v}_c, \tag{3.5}$$

where $\boldsymbol{v}_c$ is the net velocity of the two particles at the point of contact C, given by

$$\boldsymbol{v}_c = \dot{\boldsymbol{x}}_2 - \dot{\boldsymbol{x}}_1 + \boldsymbol{e}_n \times (R_1\boldsymbol{\omega}_1 + R_2\boldsymbol{\omega}_2), \tag{3.6}$$

and $\boldsymbol{e}_n$ is the unit vector normal to the tangent plane $\mathcal{P}$ at C, given by

$$\boldsymbol{e}_n = \frac{\boldsymbol{x}_2 - \boldsymbol{x}_1}{|\boldsymbol{x}_2 - \boldsymbol{x}_1|}. \tag{3.7}$$

The overlap $\boldsymbol{\xi}$ is decomposed into normal and tangential components by

$$\begin{align}
\boldsymbol{\xi}_n &= \xi_n \boldsymbol{e}_n \tag{3.8}\\
\boldsymbol{\xi}_t &= \xi_t \boldsymbol{e}_t, \tag{3.9}
\end{align}$$

where the scalars ξ_n and ξ_t are given by

$$\begin{align}
\xi_n &= \boldsymbol{\xi} \cdot \boldsymbol{e}_n \tag{3.10}\\
\xi_t &= (\boldsymbol{\xi} - \boldsymbol{\xi}_n) \cdot \boldsymbol{e}_t. \tag{3.11}
\end{align}$$

The time derivative of ξ_n is

$$\begin{align}
\dot{\xi}_n &= \dot{\boldsymbol{\xi}} \cdot \boldsymbol{e}_n + \boldsymbol{\xi} \cdot \dot{\boldsymbol{e}}_n \notag\\
&= ((\boldsymbol{e}_n \times \dot{\boldsymbol{e}}_n) \times \boldsymbol{\xi} - \boldsymbol{v}_c) \cdot \boldsymbol{e}_n + \boldsymbol{\xi} \cdot \dot{\boldsymbol{e}}_n \notag\\
&= -(\boldsymbol{\xi} \cdot \dot{\boldsymbol{e}}_n)\boldsymbol{e}_n \cdot \boldsymbol{e}_n + (\boldsymbol{\xi} \cdot \boldsymbol{e}_n)\dot{\boldsymbol{e}}_n \cdot \boldsymbol{e}_n - \boldsymbol{v}_c \cdot \boldsymbol{e}_n + \boldsymbol{\xi} \cdot \dot{\boldsymbol{e}}_n \notag\\
&= -(\boldsymbol{\xi} \cdot \dot{\boldsymbol{e}}_n)1 + (\boldsymbol{\xi} \cdot \boldsymbol{e}_n)0 - \boldsymbol{v}_c \cdot \boldsymbol{e}_n + \boldsymbol{\xi} \cdot \dot{\boldsymbol{e}}_n \notag\\
&= -\boldsymbol{v}_c \cdot \boldsymbol{e}_n, \tag{3.12}
\end{align}$$

where the vector triple product ($(\boldsymbol{a} \times \boldsymbol{b}) \times \boldsymbol{c} = -(\boldsymbol{c} \cdot \boldsymbol{b})\boldsymbol{a} + (\boldsymbol{c} \cdot \boldsymbol{a})\boldsymbol{b}$) is used along with the fact that $\dot{\boldsymbol{e}}_n \cdot \boldsymbol{e}_n = 0$. $\boldsymbol{e}_t$ is defined as a unit vector normal to $\boldsymbol{e}_n$ such that $\dot{\boldsymbol{e}}_t = (\boldsymbol{e}_n \times \dot{\boldsymbol{e}}_n) \times \boldsymbol{e}_t$.

The time derivative of ξ_t is

$$\dot{\xi}_t = \dot{\boldsymbol{\xi}}_t \cdot \boldsymbol{e}_t + \boldsymbol{\xi}_t \cdot \dot{\boldsymbol{e}}_t. \tag{3.13}$$

Focusing on the first term of the above, $\dot{\boldsymbol{\xi}}_t$ becomes

$$\begin{align}
\dot{\boldsymbol{\xi}}_t &= \dot{\boldsymbol{\xi}} - (\dot{\boldsymbol{\xi}} \cdot \boldsymbol{e}_n)\boldsymbol{e}_n - (\boldsymbol{\xi} \cdot \dot{\boldsymbol{e}}_n)\boldsymbol{e}_n - (\boldsymbol{\xi} \cdot \boldsymbol{e}_n)\dot{\boldsymbol{e}}_n \notag\\
&= \dot{\boldsymbol{\xi}} - (-\boldsymbol{\xi} \cdot \dot{\boldsymbol{e}}_n - \boldsymbol{v}_c \cdot \boldsymbol{e}_n)\boldsymbol{e}_n - (\boldsymbol{\xi} \cdot \dot{\boldsymbol{e}}_n)\boldsymbol{e}_n - (\boldsymbol{\xi} \cdot \boldsymbol{e}_n)\dot{\boldsymbol{e}}_n \notag\\
&= (\boldsymbol{e}_n \times \dot{\boldsymbol{e}}_n) \times \boldsymbol{\xi} - \boldsymbol{v}_c + (\boldsymbol{v}_c \cdot \boldsymbol{e}_n)\boldsymbol{e}_n - (\boldsymbol{\xi} \cdot \boldsymbol{e}_n)\dot{\boldsymbol{e}}_n \notag\\
&= -(\boldsymbol{\xi} \cdot \dot{\boldsymbol{e}}_n)\boldsymbol{e}_n + (\boldsymbol{\xi} \cdot \boldsymbol{e}_n)\dot{\boldsymbol{e}}_n - \boldsymbol{v}_c + (\boldsymbol{v}_c \cdot \boldsymbol{e}_n)\boldsymbol{e}_n - (\boldsymbol{\xi} \cdot \boldsymbol{e}_n)\dot{\boldsymbol{e}}_n \notag\\
&= -(\boldsymbol{\xi} \cdot \dot{\boldsymbol{e}}_n)\boldsymbol{e}_n - \boldsymbol{v}_c + (\boldsymbol{v}_c \cdot \boldsymbol{e}_n)\boldsymbol{e}_n. \tag{3.14}
\end{align}$$

Now focusing on the second term of Equation 3.13

$$\begin{align}
\boldsymbol{\xi}_t \cdot \dot{\boldsymbol{e}}_t &= (\boldsymbol{\xi} - (\boldsymbol{\xi} \cdot \boldsymbol{e}_n)\boldsymbol{e}_n) \cdot (\boldsymbol{e}_n \times \dot{\boldsymbol{e}}_n) \times \boldsymbol{e}_t \notag\\
&= (\boldsymbol{\xi} - (\boldsymbol{\xi} \cdot \boldsymbol{e}_n)\boldsymbol{e}_n) \cdot (-(\boldsymbol{e}_t \cdot \dot{\boldsymbol{e}}_n)\boldsymbol{e}_n + (\boldsymbol{e}_t \cdot \boldsymbol{e}_n)\dot{\boldsymbol{e}}_n) \notag\\
&= -\boldsymbol{\xi} \cdot (\boldsymbol{e}_t \cdot \dot{\boldsymbol{e}}_n)\boldsymbol{e}_n + ((\boldsymbol{\xi} \cdot \boldsymbol{e}_n)\boldsymbol{e}_n) \cdot (\boldsymbol{e}_t \cdot \dot{\boldsymbol{e}}_n)\boldsymbol{e}_n \notag\\
&= -(\boldsymbol{\xi} \cdot \boldsymbol{e}_n)(\boldsymbol{e}_t \cdot \dot{\boldsymbol{e}}_n) + (\boldsymbol{\xi} \cdot \boldsymbol{e}_n)(\boldsymbol{e}_n \cdot \boldsymbol{e}_n)(\boldsymbol{e}_t \cdot \dot{\boldsymbol{e}}_n) \notag\\
&= 0. \tag{3.15}
\end{align}$$

Substituting Equations 3.14 and 3.15 into Equation 3.13 gives

$$\begin{align}
\dot{\xi}_t &= (-(\boldsymbol{\xi} \cdot \dot{\boldsymbol{e}}_n)\boldsymbol{e}_n - \boldsymbol{v}_c + (\boldsymbol{v}_c \cdot \boldsymbol{e}_n)\boldsymbol{e}_n) \cdot \boldsymbol{e}_t \notag\\
&= -(\boldsymbol{\xi} \cdot \dot{\boldsymbol{e}}_n)\boldsymbol{e}_n \cdot \boldsymbol{e}_t - \boldsymbol{v}_c \cdot \boldsymbol{e}_t + (\boldsymbol{v}_c \cdot \boldsymbol{e}_n)\boldsymbol{e}_n \cdot \boldsymbol{e}_t \notag\\
&= -\boldsymbol{v}_c \cdot \boldsymbol{e}_t. \tag{3.16}
\end{align}$$

The force at the point of contact is composed of functions of the scalar part of the normal overlap ξ_n and the tangential overlap $\boldsymbol{\xi}_t$ and their time-derivatives $\dot{\xi}_n$ and $\dot{\boldsymbol{\xi}}_t$, i. e.

$$\boldsymbol{f} = \phi_n(\xi_n, \dot{\xi}_t)\boldsymbol{e}_n + \boldsymbol{\phi}_t^C(\boldsymbol{\xi}_t, \dot{\boldsymbol{\xi}}_t), \tag{3.17}$$

where $\boldsymbol{\phi}_t^C$ is governed by a Coulomb-type frictional threshold, given by

$$\boldsymbol{\phi}_t^C(\boldsymbol{\xi}_t, \dot{\boldsymbol{\xi}}_t) = \min\left[\mu\phi_n(\xi_n, \dot{\xi}_t), |\boldsymbol{\phi}_t(\boldsymbol{\xi}_t, \dot{\boldsymbol{\xi}}_t|\right] \boldsymbol{u}_t. \tag{3.18}$$

μ is the friction coefficient and $\boldsymbol{u}_t$ is given by

$$\boldsymbol{u}_t = \begin{cases} \frac{\boldsymbol{\phi}_t(\boldsymbol{\xi}_t, \dot{\boldsymbol{\xi}}_t)}{|\boldsymbol{\phi}_t(\boldsymbol{\xi}_t, \dot{\boldsymbol{\xi}}_t)|} & \text{if } \boldsymbol{\phi}_t(\boldsymbol{\xi}_t, \dot{\boldsymbol{\xi}}_t) \neq \boldsymbol{0}, \\ \boldsymbol{0} & \text{if } \boldsymbol{\phi}_t(\boldsymbol{\xi}_t, \dot{\boldsymbol{\xi}}_t) = \boldsymbol{0}. \end{cases} \tag{3.19}$$

Cundall et al. (1979)'s viscoelastic contact law is used in this thesis, for this law the components of the force are given by

$$\phi_n(\xi_n, \dot{\xi}_t) = k_n\xi_n + c_n\dot{\xi}_n, \tag{3.20}$$

$$\boldsymbol{\phi}_t(\boldsymbol{\xi}_t, \dot{\boldsymbol{\xi}}_t) = k_t\boldsymbol{\xi}_t + c_t\dot{\boldsymbol{\xi}}_t. \tag{3.21}$$

The first terms in both equations are elastic terms, and the rate dependence in the second make them viscous terms.

A problem with Cundall et al.'s viscoelastic contact law is in the determination of the parameters c_n, k_n, c_t and k_t, since they lack a meaningful physical interpretation. For some given material these parameters can be determined empirically from experiments between two particles with a single point of contact; this was done by Pournin et al. (2001), who derived analytical expression of the parameters given by

$$k_n = \frac{m_{\text{eff}}}{t_c^2}\left(\pi^2 + \ln(\delta_n)^2\right), \tag{3.22}$$

$$c_n = \frac{2m_{\text{eff}}}{t_c}\ln(\delta_n), \tag{3.23}$$

$$k_t = \frac{1}{t_c^2\left(\frac{1}{m_{\text{eff}}} + \frac{R_1^2}{I_1} + \frac{R_2^2}{I_2}\right)}\left(\pi^2 + \ln(\delta_n)^2\right), \tag{3.24}$$

$$c_t = \frac{1}{t_c\left(\frac{1}{m_{\text{eff}}} + \frac{R_1^2}{I_1} + \frac{R_2^2}{I_2}\right)}\ln(\delta_t), \tag{3.25}$$

where t_c is the duration of contact and δ_n and δ_t are, respectively, the normal and tangential restitution coefficients.

3.4 DEM SIMULATIONS

3.4.1 *Numerical software*

The simulations are done using Yet Another Dynamic Engine (YADE), an open-source framework for modelling with DEM (Gladky et al.,

MATERIAL PARAMETER	DRUM	"GLASS" BEADS
Friction coefficient μ	0.95	0.5
Normal restitution coefficient δ_n	0.46	0.56
Tangential restitution coefficient δ_t	0.46	0.46
Duration of contact t_c	10^{-4}	10^{-4}

Table 3.1: The parameters for the two types of materials in the DEM simulations.

2014). It is written in C++ and provides a Python-based wrapper for scripting. All of the simulations are run on version 1.12.0 of YADE. Post-processing is done using Python scripts; more detail on this is given in Chapter 5.

3.4.2 *Rotating drum simulations*

The simulations model a rotating drum 450mm in diameter with a smooth, high friction, surface. In the axial direction, the drum has periodic boundary conditions with a period of 24mm. The drum is filled to 40% of the total volume with 65 863 "glass" beads 3mm in diameter. The frictional, viscoelastic, contact law of Pournin et al. (2001) is used for both the beads and the drum. The material parameters used for the beads and the drum are shown in Table 3.1. The duration of contact for glass is in reality a much lower value than the one used in the simulations. A consequence of this is that the Young's modulus E_y will have a lower value than in reality. Recall from Equation 3.3 that the timestep stability condition is proportional to the inverse square of E_y of all of the particles. The small timestep needed for a larger E_y can potentially make the simulation computationally expensive. Landry et al. (2003) showed that the use of a larger Young's modulus than reality has a negligible effect on the overall response of the system.

The simulations were performed for nine equally-spaced rotational speeds: 7 revolutions per minute (rpm), 14 rpm, 21 rpm, 28 rpm, 35 rpm, 42 rpm, 49 rpm, 56 rpm and 63 rpm. The chosen speeds cover a wide range of flows in the rolling and cascading regimes. For the initial state of the system in each simulation, except the 7 rpm, a snapshot from a slower simulation is used. The initial state for the 7 rpm system is an evenly-spaced grid of particles. Each particle is imparted with a random initial velocity. In each simulation, the system was allowed to settle before taking 400 snapshots spaced evenly every 10 000 time steps. Section 3.4.3 provides detail on measures for the stability of the flow. The material quantities that are extracted from the 400 snapshots were then averaged; more details on this are given in Chapter 5.

SIMULATION	REAL TIME [DAY]	TIMESTEPS	VIRTUAL TIME [S]
7 rpm	41.9	51,170,037	62.9
14 rpm	16.5	16,001,794	19.6
21 rpm	21.1	20,675,746	25.4
28 rpm	25.2	19,864,296	24.4
35 rpm	20.1	17,137,824	21.0
42 rpm	16.6	17,965,503	22.1
49 rpm	21.7	19,442,342	23.9
56 rpm	20.0	19,377,426	23.8
63 rpm	16.5	14,979,367	18.4

Table 3.2: Time taken for each simulation, in real and virtual time, as well as the number of timesteps.

The simulations were run on two Intel Xeon E5-2470 machines. Each machine has 16 cores. Yade is parallelized for shared memory systems, so each machine ran one simulation at a time. In all of the simulations a timestep of $\Delta t = 1.23 \times 10^{-6}$s was used. Table 3.2 shows the real and virtual times for each simulation, as well as the number of timesteps. Each simulation took on average about 22 days in real-time to simulate about 21.8×10^{6} timesteps (26s virtual time).

3.4.3 *Settling of the system*

As mentioned in the previous section the snapshots of the system are taken once it has settled into a steady state. In this section, some detail is given on how to quantify at what point in time the system reaches a steady state. Three measures are used to investigate the stability of the system over time: the head, the departure shoulder and the centre of mass (recall the definitions in Section 2.2). Consider the system with the set of N particles, denoted $\mathcal{P}$, and the subset of particles that are in contact with the drum wall, denoted $\mathcal{P}_{\text{drum}}$. The departure shoulder, denoted H_d, is the maximum height of all of the particles in $\mathcal{P}_{\text{drum}}$:

$$H_d = \max_{\boldsymbol{x} \in \mathcal{P}_{\text{drum}}} (\boldsymbol{x}|_z), \tag{3.26}$$

where $\boldsymbol{x}$ is the location in Cartesian coordinates. In this coordinate system the axis of the drum lies along the x-axis and the z-axis is parallel to $\boldsymbol{g}$. The head H_h is the maximum height of all the particles

$$H_h = \max_{i \in \{1,\ldots,N\}} (\boldsymbol{x}^i|_z) \tag{3.27}$$

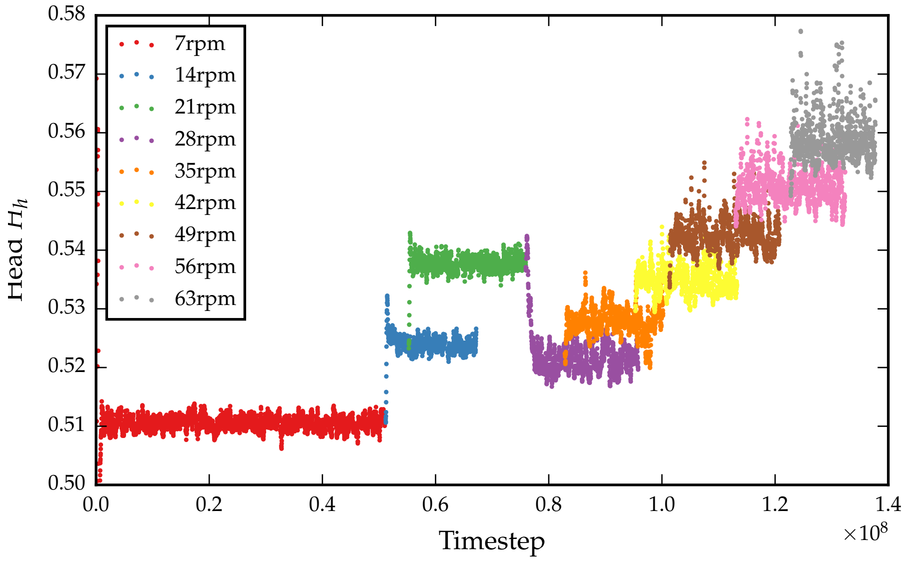

Figure 3.2: The head H_h for all of the simulations. The height increases with rotational speed, except for a sudden decrease that is observed as the drum speed is increased from 21 to 28 rpm

and the centre of mass $\boldsymbol{H}_c$ is given by[1]

$$\boldsymbol{H}_c = \frac{1}{N} \sum_{i=1}^{N} \boldsymbol{x}^i. \tag{3.28}$$

The head H_h for all of the simulations performed is shown in Figure 3.2. There is a large amount of noise in the head for each simulation. This is because the highest particles are usually very fast moving, cataracting, particles. Despite the noise it is clear that the head increases up until 21 rpm, decreases suddenly at 28 rpm, and then increases from 35 rpm onwards. The departure shoulder H_d for all of the simulations performed is shown in Figure 3.3. This quantity is less noisy than the head as it is linked to the slower-moving particles in contact with the wall of the drum. Again a sudden decrease is observed as the speed increases to 28 rpm. The centre of mass H_c is shown in Figure 3.4. The sudden decrease is also observed there.

It is conjectured that the sudden decrease, or slipping event, is related to the frictional properties of the drum and particles. As the speed of the drum is increased the force imparted on the particles in contact with the drum will also increase. The particles and the facets that make up the drum interact via the same viscoelastic contact law described in Section 3.3. In the tangential direction, they interact via Coulomb friction (Equation 3.18). It is hypothesized that the slipping event is the result of the particles in contact with the mill collectively reaching the frictional threshold, and then all slipping against the surface of the drum in unison. This slipping of the whole system would

---

[1] All particles have the same mass

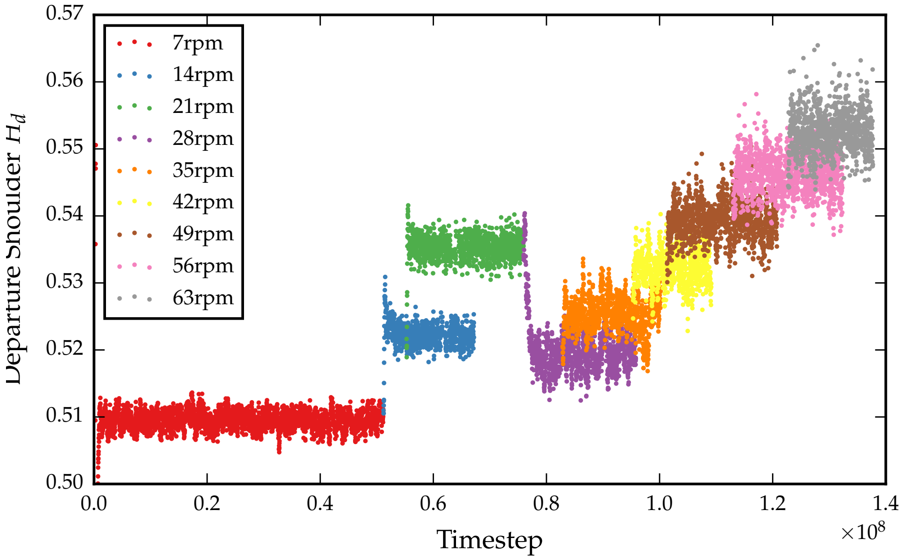

Figure 3.3: The departure shoulder H_d for all of the simulations. As with Figure 3.2 the sudden decrease at 28 rpm is observed here.

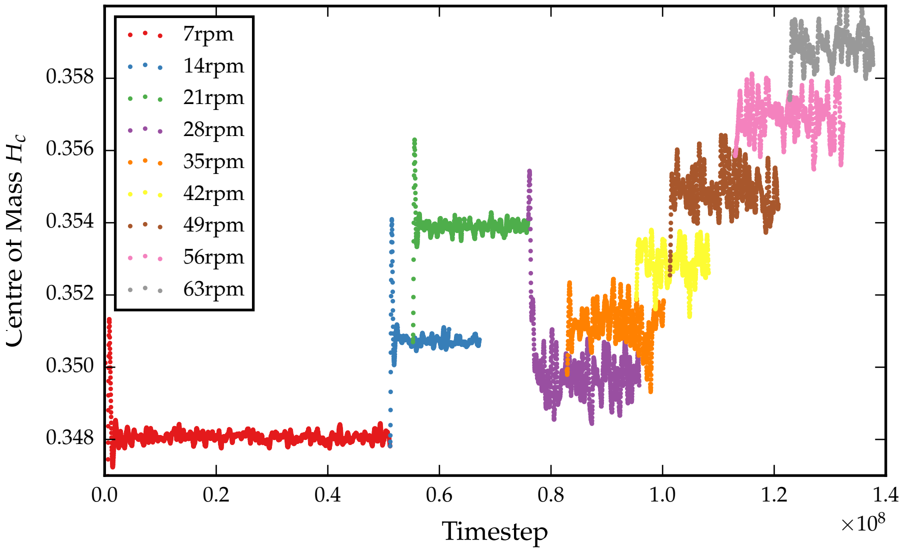

Figure 3.4: The height of the centre of mass $(\boldsymbol{H}_c)_z$ for all of the simulations.

result in a sudden decrease in the various height measures of the system, similar to what is observed.

A way of testing the hypothesis is to examine kinetic measures of the particles in contact with the drum. In order to do this a final simulation is performed in which the rotational speed of the drum is increased incrementally from 21 rpm to 28 rpm over 10^7 timesteps. The incremental increase is done to determine more accurately the speed at which the slipping of the system occurs. Figure 3.5 shows the centre of mass for the final simulation. The system appears to slip in between 27 and 28 rpm.

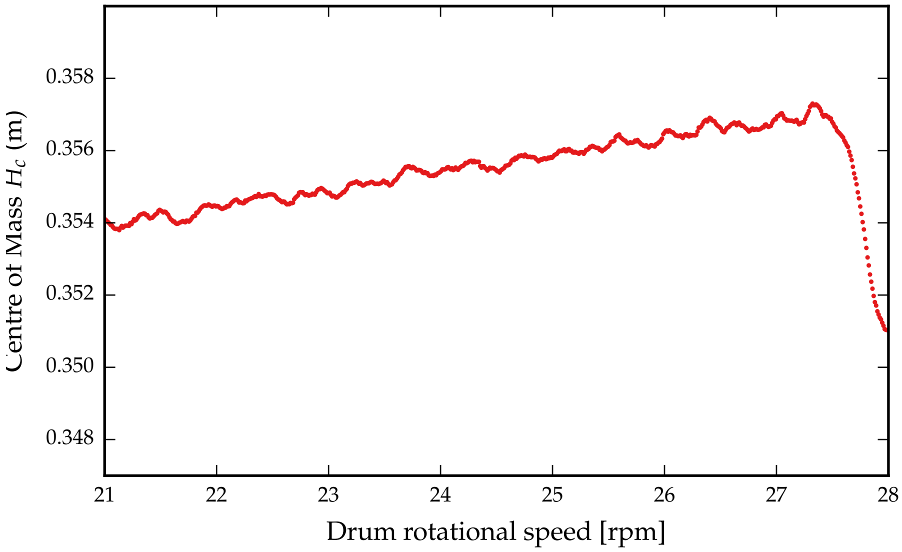

Figure 3.5: The height of the centre of mass $(\boldsymbol{H}_c)_z$ for the final simulation, in which the rotational speed is incrementally increased from 21 to 28 rpm. The slipping event occurs in between 27 and 28 rpm.

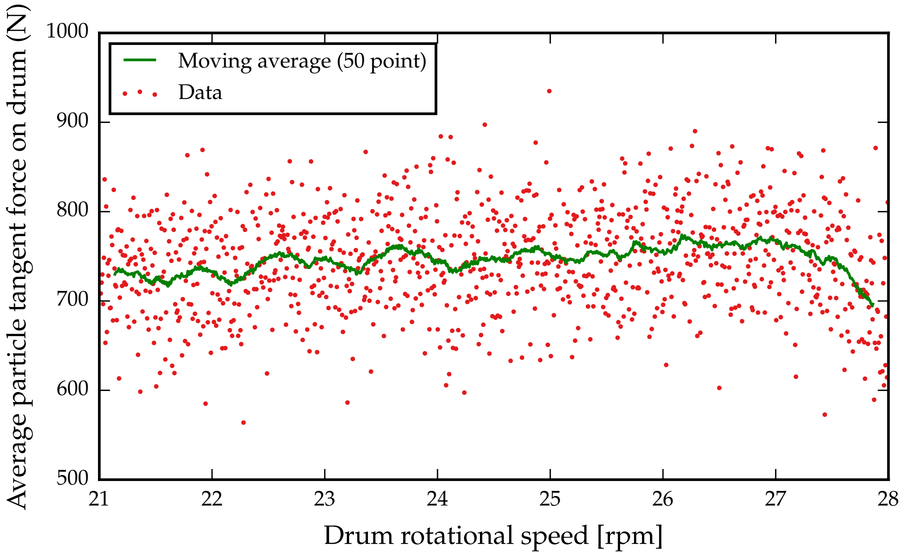

Figure 3.6: The average force tangent to the surface of the drum for all of the particles in contact with the drum. Also shown is a moving average (in green), which, for each point, takes the average of the surrounding 50 data points. This data is from the final simulation in which the rotational speed is increased linearly from 21 to 28 rpm.

The kinetic measure that is used to test the hypothesis is the force imparted on each particle that is in contact with the surface of the drum. Figure 3.6 shows the average force tangential to the surface of the drum for all of the particles in contact with the drum. The tangential force data is relatively noisy. A moving average is also shown in order to aid in discerning the overall trend in the data. A small decrease in the tangential force can be seen in between 27 and 28 rpm. The decrease indicates in a qualitative manner that the hypothesis may be correct, however further work is needed that is outside the scope of this thesis.

3.5 SUMMARY

In this chapter the simulations of a rotating drum were described. The results of these simulations are analyzed in later chapters. A brief description of DEM using an explicit time-integration scheme was given. A derivation was given for the visco-elastic contact law that was used in the simulations.

Nine 3D DEM simulations were performed with the rotational speed of the drum varying (with equal increments) from 7 rpm to 63 rpm. The inside surface of the drum was given a highly frictional surface and filled with glass beads.

A sudden decrease in the height of the bed was observed in between 27 and 28 rpm. This decrease was investigated by examining the average tangent force of the particles in contact with the drum. The sudden decrease was possibly due to a frictional threshold between the surface of the drum and the particles being reached as the rotational speed of the drum increased.

4

MESO-SCALE CONSTITUTIVE LAW

4.1 INTRODUCTION

Granular systems with rapid-dense flow behave in a manner qualitatively similar to fluids. A fundamental assumption for fluids is that of the continuum. A continuous system has material quantities that can be represented as smooth functions of position and time. For typical fluids, e. g. water, the continuum assumption can be made because there is a very large separation between the microscopic and macroscopic scales. Granular systems do not have a large degree of separation between scales and are more accurately interpreted as being in the mesoscopic scale. The meso-scale is the intermediate scale between the microscopic and macroscopic scales. Although there is not a clear separation between the mesoscopic and microscopic scales, for the purposes of this work the assumption is made that the granular system as a whole can be described as a continuum.

In this chapter the kinematic and kinetic quantities are defined in Sections 4.2 and 4.3, respectively. A derivation of the constitutive relations, which relate kinematic and kinetic quantities, for isotropic incompressible fluids is given in Section 4.4.1. A number of constitutive models are discussed. Particular attention is given to the constitutive law for dense granular flow of Jop et al. (2006) in Section 4.4.3. Some of the key assumptions of (Jop et al., 2006) are outlined.

4.2 KINEMATICS

4.2.1 *Motion*

Define the body B_0 as an object that occupies a region of Euclidean space $\mathcal{E}$ in some fixed configuration called the reference configuration, also called the material configuration. The choice of a reference configuration is arbitrary. B_0 is referred to as the reference body, and to a point $\boldsymbol{X}$ in B_0 as a material point or particle. A motion of a point in B_0 is a smooth bijective function. The motion χ assigns to each material point $\boldsymbol{X}$ at time t a point

$$x = \chi(\boldsymbol{X}, t), \tag{4.1}$$

where $\boldsymbol{x}$ is referred to as the spatial (or current) point. The displacement is defined to be the difference between the spatial and reference points, i.e.

$$\begin{aligned} \boldsymbol{u}(\boldsymbol{X},t) &= \boldsymbol{x} - \boldsymbol{X} \\ &= \chi(\boldsymbol{X},t) - \boldsymbol{X}. \end{aligned} \tag{4.2}$$

The velocity ($\boldsymbol{v}$) is defined as the rate of change in time of the displacement, i.e.

$$\boldsymbol{v}(\boldsymbol{X},t) = \dot{\boldsymbol{u}} = \frac{\partial \boldsymbol{u}}{\partial t}. \tag{4.3}$$

4.2.2 *Velocity gradient*

The spatial velocity gradient is given by

$$\boldsymbol{L} = \frac{\partial \boldsymbol{v}}{\partial \boldsymbol{x}}. \tag{4.4}$$

The symmetric velocity gradient $\boldsymbol{D}$ is commonly used in constitutive relations for fluids, it is given by

$$\boldsymbol{D} = \frac{1}{2}(\boldsymbol{L} + \boldsymbol{L}^T). \tag{4.5}$$

The deviatoric (volume preserving) part of $\boldsymbol{D}$ is given by

$$\boldsymbol{D}_{\text{dev}} = \boldsymbol{D} - \frac{1}{3}\text{tr}(\boldsymbol{D})\boldsymbol{I}. \tag{4.6}$$

4.3 STRESS AND BALANCE RELATIONS

4.3.1 *Body force and traction*

Consider a body which is undergoing a deformation, as shown in Figure 4.1. Consider an infinitesimal surface area dA inside the body in the reference configuration, which maps to da, an infinitesimal surface area in the current configuration. In the current configuration the relationship between the infinitesimal internal force, $d\boldsymbol{f}$, and the infinitesimal surface area is given by

$$d\boldsymbol{f} = \boldsymbol{t}da, \tag{4.7}$$

where $\boldsymbol{t}$ is the Cauchy traction. Similarly in the reference configuration the first Piola-Kirchhoff traction $\boldsymbol{T}$ relates $d\boldsymbol{f}$ to dA by

$$d\boldsymbol{f} = \boldsymbol{T}dA. \tag{4.8}$$

Cauchy's postulate states that the two tractions are dependent on their respective normals, their position and time, i.e.

$$\boldsymbol{T} = \boldsymbol{T}(\boldsymbol{X},t,\boldsymbol{N}) \text{ and } \boldsymbol{t} = \boldsymbol{t}(\boldsymbol{x},t,\boldsymbol{n}). \tag{4.9}$$

The force per unit current volume that is applied to the entire body is denoted by $\boldsymbol{b}$. In the following sections the focus will be on quantities in the current configuration.

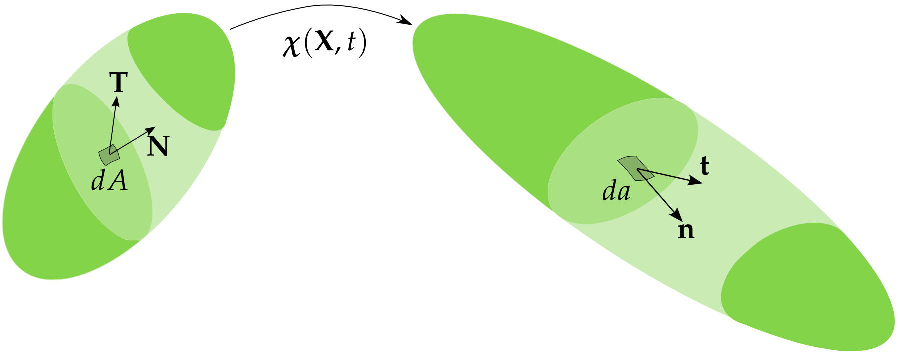

Figure 4.1: A diagram of a body undergoing a deformation.

4.3.2 *Stress*

Cauchy's stress theorem postulates a linear relationship between the Cauchy traction, $\boldsymbol{t}$ and the normal, $\boldsymbol{n}$. There exists a spatial tensor field $\boldsymbol{\sigma}$, called the Cauchy stress, such that

$$\boldsymbol{t} = \boldsymbol{\sigma}\boldsymbol{n}. \tag{4.10}$$

The shear stress $\boldsymbol{\tau}$ is defined as the deviatoric component of the stress

$$\boldsymbol{\tau} = \boldsymbol{\sigma} - \frac{1}{3}\mathrm{tr}(\boldsymbol{\sigma})\boldsymbol{I}. \tag{4.11}$$

4.3.3 *Momentum balance*

The balance of linear momentum in the current configuration is given by

$$\rho\left(\frac{\partial \boldsymbol{v}}{\partial t} + \boldsymbol{L}\boldsymbol{v}\right) = \mathrm{div}\boldsymbol{\sigma} + \boldsymbol{b}, \tag{4.12}$$

where ρ is the spatial density. It can be shown via the balance of angular momentum that the Cauchy stress is symmetric

$$\boldsymbol{\sigma} = \boldsymbol{\sigma}^T. \tag{4.13}$$

4.3.4 *Mass conservation*

In a classical continuum the mass conservation equation is given by

$$\frac{\partial \rho}{\partial t} + \mathrm{div}(\rho \boldsymbol{v}) = 0. \tag{4.14}$$

4.4 CONSTITUTIVE MODELS

Together the linear momentum equation, symmetric stress equation and mass balance equation (Equations 4.12, 4.13, and 4.14, respectively) amount to 7 equations. The quantities $\boldsymbol{v}$, $\boldsymbol{\sigma}$ (excluding symmetry) and ρ amount to 13 unknowns. The imbalance in knowns to unknowns necessitates the use of additional relations called constitutive relations. This section provides an outline of a number of constitutive relations as well as the derivation for an isotropic incompressible fluid.

4.4.1 *Derivation of constitutive models for fluids*

The behaviour of an isotropic material is invariant of its orientation in space. The Rivlin-Ericksen theorem (Astarita et al., 1974) states that an isotropic symmetric tensor function $\boldsymbol{g}(\boldsymbol{D})$ can only be of the form given by

$$\boldsymbol{g}(\boldsymbol{D}) = \alpha_0 \boldsymbol{I} + \alpha_1 \boldsymbol{D} + \alpha_2 \boldsymbol{D}^2, \tag{4.15}$$

where α_i are scalar functions of the invariants of $\boldsymbol{D}$

$$\alpha_i = \alpha_i(I_D, II_D, III_D), \tag{4.16}$$

and the invariants are

$$I_D = \text{tr}\boldsymbol{D}, \quad II_D = \text{tr}\boldsymbol{D}^2, \quad III_D = \det \boldsymbol{D}. \tag{4.17}$$

Consequently the most general stress for an isotropic fluid must be of the form

$$\boldsymbol{\sigma}(\boldsymbol{D}) = \alpha_0 \boldsymbol{I} + \alpha_1 \boldsymbol{D} + \alpha_2 \boldsymbol{D}^2. \tag{4.18}$$

Fluids of this form are referred to as Reiner-Rivlin fluids. When there is no rate of deformation ($\boldsymbol{D} = \boldsymbol{0}$) the stress should be hydrostatic, i.e. $\boldsymbol{\sigma}(\boldsymbol{0}) = \alpha_0 \boldsymbol{I}$. It can be shown that $\alpha_0 = -\tilde{p} + \lambda \text{tr}\boldsymbol{D}$ (Aris, 1990, Chapter 5.23), where $\tilde{p}$ is the hydrostatic pressure and λ the bulk viscosity. Equation (4.18) now becomes

$$\boldsymbol{\sigma}(\boldsymbol{D}) = (-\tilde{p} + \lambda \text{tr}\boldsymbol{D})\boldsymbol{I} + \alpha_1 \boldsymbol{D} + \alpha_2 \boldsymbol{D}^2. \tag{4.19}$$

The density ρ of the material is assumed to be constant (incompressible). The mass conservation Equation (4.14) now becomes

$$\text{div}(\boldsymbol{v}) = \text{tr}\boldsymbol{D} = 0. \tag{4.20}$$

The constitutive equation is now of the following form

$$\boldsymbol{\sigma}(\boldsymbol{D}) = -\tilde{p}\boldsymbol{I} + \alpha_1 \boldsymbol{D} + \alpha_2 \boldsymbol{D}^2. \tag{4.21}$$

The hydrostatic pressure is thus the same the pressure $p = -\frac{1}{3}\text{tr}\boldsymbol{\sigma} = -\frac{1}{3}\text{tr}(-\tilde{p}\boldsymbol{I} + \alpha_1 \boldsymbol{D} + \alpha_2 \boldsymbol{D}^2) = \tilde{p}$. Thermodynamic considerations restrict the possible values of α_1 and α_2 (Astarita et al., 1974). The only physically realistic combination is $\alpha_1 \geq 0$ and $\alpha_2 = 0$, which gives

$$\boldsymbol{\sigma}(\boldsymbol{D}) = -p\boldsymbol{I} + 2\eta \boldsymbol{D}, \tag{4.22}$$

where η is the viscosity. Note the colinearity assumption in the law of Jop et al. (2006) arises from the restriction that $\alpha_2 = 0$. The shear stress (Equation 4.11) is thus given by

$$\boldsymbol{\tau} = 2\eta \boldsymbol{D}. \tag{4.23}$$

If η is constant then fluids conforming to equation (4.22) are referred to as incompressible Newtonian fluids, if not the fluid is referred to as a non-Newtonian fluid. The following subsections describe some relevant non-Newtonian fluids.

4.4.2 *Bingham and Herschel-Bulkley fluids*

Some fluids do not flow until the magnitude of the shear stress reaches a threshold. The Bingham fluid model displays this kind of behaviour (Malvern, 1969). The rate of deformation is written in terms of the shear stress as follows

$$2\eta \boldsymbol{D} = \begin{cases} \boldsymbol{0} & \text{if } F < 0 \\ F\boldsymbol{\tau} & \text{if } F \geq 0 \end{cases}. \tag{4.24}$$

F is a scalar measure of the intensity of the stress, given by

$$F = 1 - \frac{k}{\sqrt{II_\tau}}, \tag{4.25}$$

where k is the critical value at which the fluid yields and $II_\tau = \mathrm{tr}(\boldsymbol{\tau}^2)$ is the second invariant of $\boldsymbol{\tau}$. While granular systems do display this type of behaviour, the critical value would be variable due to the hysteresis that has been observed in the transition from solid- to liquid-like flows (Rajchenbach, 1990).

A generalization of the Bingham fluid is the Herschel-Bulkley fluid (Bird et al., 1983), given by

$$\eta = \begin{cases} \eta_0 & \text{if } |\boldsymbol{D}| < D_0 \\ k|\boldsymbol{D}|^{n-1} + \tau_0|\boldsymbol{D}| & \text{if } |\boldsymbol{D}| \geq D_0, \end{cases} \tag{4.26}$$

where D_0 is the yielding value for the rate of deformation.

4.4.3 *Dense granular flow model*

Recall from Chapter 2.5 the 3D constitutive model proposed by Jop et al. (2006), where the effective viscosity η is dependent on the shear rate and the pressure

$$\boldsymbol{\tau} = \eta(|\dot{\gamma}|_J, p)\dot{\gamma}, \tag{4.27}$$

where Jop et al. define $\dot{\gamma} = \boldsymbol{L} + \boldsymbol{L}^T$ and the non-standard norm $|\dot{\gamma}|_J = \sqrt{\frac{1}{2}\gamma_{ij}\gamma_{ij}}$.

Equation 4.27 in terms of the symmetric velocity gradient $\boldsymbol{D}$ and the standard norm $|\boldsymbol{D}| = \sqrt{D_{ij}D_{ij}}$ is given by

$$\boldsymbol{\tau} = 2\eta(\sqrt{2}|\boldsymbol{D}|, p)\boldsymbol{D}. \tag{4.28}$$

Note in the above equation that $|\dot{\gamma}|_J = \sqrt{2}|\boldsymbol{D}|$. The effective viscosity is given by

$$\eta(\sqrt{2}|\boldsymbol{D}|, p) = \mu(I)\frac{p}{\sqrt{2}|\boldsymbol{D}|}, \tag{4.29}$$

where the function for the effective friction coefficient $\mu(I)$ was determined phenomenologically by Jop et al. (2006) as

$$\mu(I) = \mu_1 + \frac{\mu_2 - \mu_1}{I_0/I + 1}, \tag{4.30}$$

where the constants for glass beads are $\mu_1 = \tan 21°$, $\mu_2 = \tan 33°$, $I_0 = 0.6$ and $\phi_m = 0.4$ (Jop et al., 2005). Jop et al. (2006) define the inertial number I in 3D in terms of the non-standard norm. Using the standard norm of $\boldsymbol{D}$, I is given by

$$I = \sqrt{2}|\boldsymbol{D}|d\sqrt{\frac{\rho_p}{p}}. \tag{4.31}$$

The constitutive model of Jop et al., as investigated in this thesis, is fully described by Equations 4.27 to 4.31.

Forterre et al. (2008) emphasized that the strength of a granular material comes not only from the friction between grains, but also from the entanglement of the particles. The properties of the entanglement between some particles is dependent on the history of the system (Daerr et al., 1999). Hysteresis has been observed in the transitions from solid- to liquid-like and liquid- to gas-like flows. In the context of rotating drums the hysteresis is observed as an inconsistency in the rotational speed where the transition from intermittent avalanching to continuous flow occurs. Rajchenbach (1990) observed that, when starting with intermittent flow and increasing the rotational speed, the transition occurs at a different speed to the opposite case where the system is continuously flowing and the speed is decreased. The hysteresis implies that for some friction coefficient there can potentially be multiple values of inertial number. Lee et al. (2012) suggest that an effective friction of the form shown in Figure 4.2 should be able to capture the observed hysteresis.

4.5 SUMMARY

In this chapter the kinetic and kinematic quantities used in descriptions of fluids have been defined. The derivation of the constitutive law for an isotropic, incompressible, fluid was given and a number of constitutive relations were outlined.

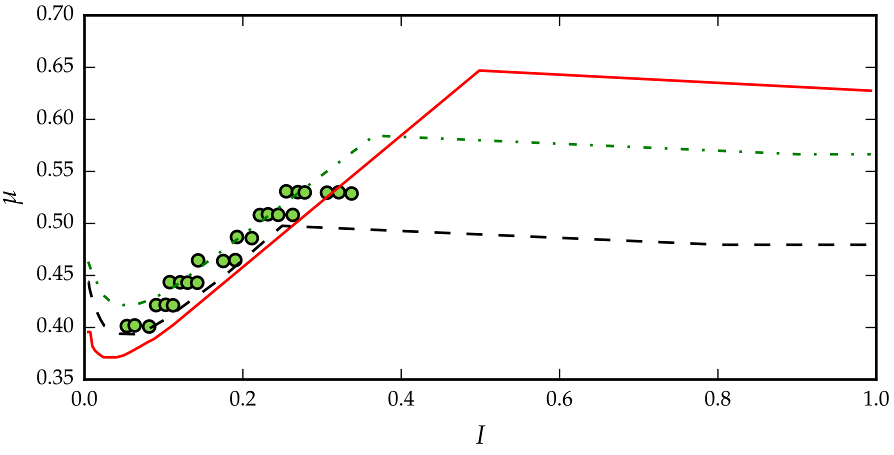

Figure 4.2: The effective friction coefficient proposed by Lee et al. (2012) and experimental data of GDR MiDi (2004) (green circles), the solid and dashed lines represent the new constitutive relation with various effective restitution coefficients and static internal friction angles. The "hook" shape for low inertial numbers is intended to capture hysteresis in the transition from solid-like to liquid-like flow.

The non-Newtonian fluid model of Jop et al. (2006) for rapid dense granular flow was described. The key assumptions for the constitutive relation of Jop et al. are:

1. Incompressibility, i.e. $\text{div}(\boldsymbol{v}) = \text{tr}\boldsymbol{D} = 0$.

2. Colinearity of the shear stress $\boldsymbol{\tau}$ and symmetric velocity gradient $\boldsymbol{D}$ tensors.

3. An approximately constant packing fraction ϕ.

These assumptions will be tested by examining kinetic and kinematic quantities extracted from the DEM simulations described in Chapter 3. Jop et al.'s law has been assessed in simulations of rotating drums in 2D Cortet et al. (2009), but not in 3D, which is a novel contribution of this thesis. In the next chapter the methods for extracting the kinetic and kinematic quantities from the simulations (see Chapter 3.4) are described.

5

HOMOGENIZATION AND FEATURE EXTRACTION

5.1 INTRODUCTION

Given the discrete nature of a granular medium, spatial averaging techniques need to be used to obtain the continuum kinematic and kinetic measures. To process the data from the simulations, the domain is divided into a number of volumetric elements. The averaging to obtain the continuum measures is done over these volumetric elements. This is different from typical homogenization techniques as those require a significant scale separation between the system and the particle. In the simulations done in this work the particles are only two orders of magnitude smaller than the whole system. Irrespective of the lack of scale separation, the volume averaging procedure provides a robust mechanism to transform discrete data to continuum fields (Rycroft et al., 2009).

The purpose of this chapter is to provide details on the spatio-temporal averaging methods as well as the techniques used to locate features of the flow in rotating drums. A detailed derivation of the stress $\boldsymbol{\sigma}$ for generalized volumetric elements is given. A linear regression algorithm for finding the velocity $\boldsymbol{D}$ gradient is outlined. In addition, the results of the described techniques applied to the rotating drum simulations are shown.

As mentioned in Chapter 3, the rotating drum simulations are performed over a range of 9 equally-spaced rotational speeds from 7 to 63 rpm. This set of simulations will be referred to as the "test space".

This chapter is arranged as follows. In Section 5.2 an outline of the process for temporal averaging is given and a spatial averaging function is defined. A full derivation of the method for obtaining the components of the stress tensor is given in Section 5.4. The technique for obtaining the velocity gradient is described in Section 5.5. The packing fraction is obtained using methods described in Section 5.6. The methods of approximating the equilibrium- and free-surfaces are described in Section 5.7. The results of the inertial number are shown in Section 5.8.

5.2 SPATIO-TEMPORAL AVERAGING

As described in Chapter 3 snapshots are taken of the 9 DEM simulations every 10000 timesteps. 400 snapshots are taken for each simulation. The spatio-temporal averaging for each simulation takes place as follows. The data from the 400 snapshots are merged into 40 groups

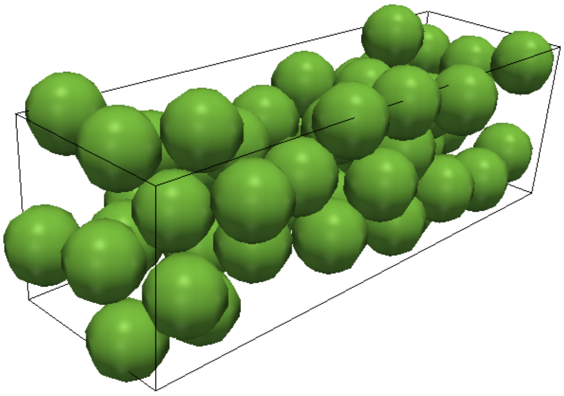

Figure 5.1: A volumetric element with spheres inside.

of 10 data sets. Merging 400 snapshots would be ideal, but computer memory limitations make this infeasible The spatial averaging techniques to obtain material quantities are performed on the merged data sets. The results of the 40 processed datasets are then averaged to obtain the final quantities.

Define an averaging function $\mathcal{G}(\boldsymbol{x})$ that satisfies the following conditions:

$$\int \mathcal{G}(\boldsymbol{x})\, dV = 1 \quad \text{and} \quad \nabla \mathcal{G}(\boldsymbol{0}) = \boldsymbol{0}. \tag{5.1}$$

Possible functions include multivariate Gaussian distributions and step-functions. The volumetric element that is used in this case corresponds to a rectangular step function, given by

$$\mathcal{G}(\boldsymbol{x}) = \begin{cases} 1 & \text{if } \; -\frac{l_i}{2} < x_i - \hat{x}_i < \frac{l_i}{2},\; i \in \{1,2,3\} \\ 0 & \text{otherwise} \end{cases}, \tag{5.2}$$

where $\hat{\boldsymbol{x}}$ is the centre of the prism and $\boldsymbol{l}$ is an array representing the size of the prisms, given by

$$\boldsymbol{l} = (2.5d, 2.5d, 8d), \tag{5.3}$$

where d is the diameter of the particles, see Figure 5.1. Note that the volumetric elements are made to span the axis of the drum ($8d$ in length), which makes them periodic.

The volumetric element is the same size as those used in the analyses of Rycroft et al. (2009). The size of the volumetric element is small enough to resolve local effects such as shear bands, which are typically $10d$ to $15d$ in size (GDR MiDi, 2004). Since a very large number of snapshots were used, the size of the volumetric element could have been decreased with minimal increase in noise, as was done by Cortet et al. (2009). This would, however, have increased the computational cost of the analysis without any benefit other than the results appearing slightly "smoother".

The volumetric elements are arranged in a grid. If any are found to overlap with the edge of the drum, they are removed. This prevents spurious edge effects from arising in the results.

5.3 VELOCITY

Using the general averaging function $\mathcal{G}(\boldsymbol{x})$ the average density is given by

$$\rho(\boldsymbol{x},t) = m\sum_{\alpha=1}^{N}\mathcal{G}(\boldsymbol{x}-\boldsymbol{x}^{\alpha}(t)). \tag{5.4}$$

Note above the use of the superscript α to denote the position of the particle $\boldsymbol{x}^{\alpha}$. Greek superscripts are used for summations over particles. The density-weighted average velocity is given by

$$\rho\boldsymbol{v}(\boldsymbol{x},t) = m\sum_{\alpha=1}^{N}\boldsymbol{v}^{\alpha}(t)\mathcal{G}(\boldsymbol{x}-\boldsymbol{x}^{\alpha}(t)). \tag{5.5}$$

The magnitude of the velocity $|\boldsymbol{v}|$ over the test space is shown in Figure 5.2.

5.4 STRESS

The constitutive law under investigation (Jop et al., 2006) has the shear stress $\boldsymbol{\tau}$ and the pressure p as the kinetic measures, these represent the deviatoric and volumetric components of the stress $\boldsymbol{\sigma}$, respectively, i.e.

$$\boldsymbol{\sigma} = \boldsymbol{\tau} + p\boldsymbol{I} \tag{5.6}$$

$$p = -\frac{1}{3}\mathrm{tr}\boldsymbol{\sigma}. \tag{5.7}$$

A derivation of the stress $\boldsymbol{\sigma}$ over the region described by the averaging function is now given.

First obtain the derivative of Equation 5.5 with respect to time

$$\begin{aligned}
\frac{\partial\rho v_i(\boldsymbol{x},t)}{\partial t} =& m\sum_{\alpha=1}^{N} v_i^{\alpha}(t)\frac{\partial(\boldsymbol{x}-\boldsymbol{x}^{\alpha}(t))}{\partial t}\frac{\partial\mathcal{G}(\boldsymbol{x}-\boldsymbol{x}^{\alpha}(t))}{\partial x_j}\\
&+m\sum_{\alpha=1}^{N}\frac{dv_i^{\alpha}(t)}{dt}\mathcal{G}(\boldsymbol{x}-\boldsymbol{x}^{\alpha}(t))\\
=&-m\sum_{\alpha=1}^{N} v_i^{\alpha}(t)v_j^{\alpha}(t)\frac{\partial\mathcal{G}(\boldsymbol{x}-\boldsymbol{x}^{\alpha}(t))}{\partial x_j}\\
&+m\sum_{\alpha=1}^{N}\frac{dv_i^{\alpha}(t)}{dt}\mathcal{G}(\boldsymbol{x}-\boldsymbol{x}^{\alpha}(t)).
\end{aligned} \tag{5.8}$$

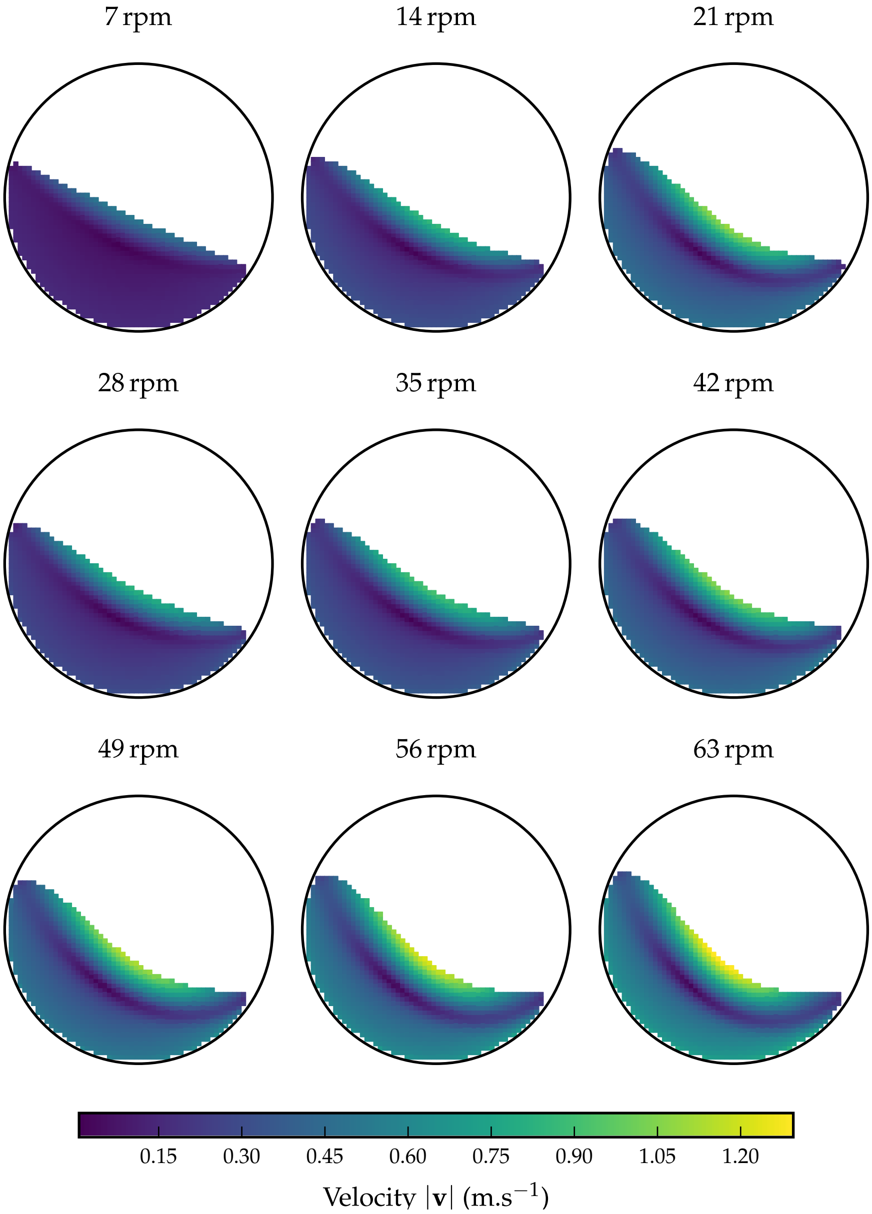

Figure 5.2: The magnitude of the velocity $|v|$ over the test space.

Multiplying Equation 4.14 by $\boldsymbol{v}$ and adding to Equation 4.12 gives

$$\begin{aligned} &\rho\frac{\partial v_i}{\partial t}+\rho\frac{\partial v_i}{\partial x_j}v_j+v_i\frac{\partial \rho}{\partial t}+v_i\frac{\partial \rho v_j}{\partial x_j}=\frac{\partial \sigma_{ij}}{\partial x_j}+\rho g_i \\ \Rightarrow &\left(\frac{\partial \rho v_i}{\partial t}+\frac{\partial \rho v_i v_j}{\partial x_j}\right)=\frac{\partial \sigma_{ij}}{\partial x_j}+\rho g_i. \end{aligned} \tag{5.9}$$

Subtracting Equation 5.9 from Equation 5.8 gives

$$\begin{aligned} \frac{\partial \sigma_{ij}}{\partial x_j}=&\underbrace{\frac{\partial}{\partial x_j}\left(\rho v_i v_j-m\sum_{\alpha=1}^{N}v_i^\alpha(t)v_j^\alpha(t)\mathcal{G}(\boldsymbol{x}-\boldsymbol{x}^\alpha(t))\right)}_{A} \\ &\underbrace{+m\sum_{\alpha=1}^{N}\left(\frac{dv_i^\alpha(t)}{dt}-g_i\right)\mathcal{G}(\boldsymbol{x}-\boldsymbol{x}^\alpha(t)).}_{B} \end{aligned} \tag{5.10}$$

Focusing now on part A of Equation 5.10

$$\begin{aligned} &\rho v_i v_j-m\sum_{\alpha=1}^{N}v_i^\alpha(t)v_j^\alpha(t)\mathcal{G}(\boldsymbol{x}-\boldsymbol{x}^\alpha(t)) \\ =&\rho v_i v_j-m\sum_{\alpha=1}^{N}\left(v_i^\alpha(t)v_j^\alpha(t)-v_i v_j^\alpha(t)-v_i^\alpha(t)v_j+v_i v_j\right)\mathcal{G}(\boldsymbol{x}-\boldsymbol{x}^\alpha(t)) \\ &+m\sum_{\alpha=1}^{N}\left(-v_i v_j^\alpha(t)-v_i^\alpha(t)v_j+v_i v_j\right)\mathcal{G}(\boldsymbol{x}-\boldsymbol{x}^\alpha(t)) \\ =&\rho v_i v_j-m\sum_{\alpha=1}^{N}\left(v_i^\alpha(t)-v_i\right)\left(v_j^\alpha(t)-v_j\right)\mathcal{G}(\boldsymbol{x}-\boldsymbol{x}^\alpha(t)) \\ &-v_i m\sum_{\alpha=1}^{N}v_j^\alpha(t)\mathcal{G}(\boldsymbol{x}-\boldsymbol{x}^\alpha(t)) \\ &-v_j m\sum_{\alpha=1}^{N}v_i^\alpha(t)\mathcal{G}(\boldsymbol{x}-\boldsymbol{x}^\alpha(t)) \\ &+v_i v_j m\sum_{\alpha=1}^{N}\mathcal{G}(\boldsymbol{x}-\boldsymbol{x}^\alpha(t)) \\ =&\rho v_i v_j-m\sum_{\alpha=1}^{N}\left(v_i^\alpha(t)-v_i\right)\left(v_j^\alpha(t)-v_j\right)\mathcal{G}(\boldsymbol{x}-\boldsymbol{x}^\alpha(t)) \\ &-v_i\rho v_j-v_j\rho v_i+v_i v_j\rho \\ =&-m\sum_{\alpha=1}^{N}\left(v_i^\alpha(t)-v_i\right)\left(v_j^\alpha(t)-v_j\right)\mathcal{G}(\boldsymbol{x}-\boldsymbol{x}^\alpha(t)). \end{aligned} \tag{5.11}$$

Now part B of Equation 5.10 is now considered. First recall the momentum for particle α

$$m\frac{dv_i^\alpha}{dt}=mg_i+\sum_\beta f_i^{\alpha\beta}(t), \tag{5.12}$$

with $\boldsymbol{f}^{\alpha\beta}(t)$ being the force exerted by particle β on particle α. Part B can thus be rewritten as

$$B = \sum_{\alpha=1}^{N} \sum_{\beta=1}^{N} f_i^{\alpha\beta}(t)\mathcal{G}(\boldsymbol{x} - \boldsymbol{x}^{\alpha}(t)). \tag{5.13}$$

Given that $f_i^{\alpha\beta} = -f_i^{\beta\alpha}$, we can write this as

$$B = \sum_{\alpha=1}^{N} \sum_{\beta=1}^{N} -f_i^{\beta\alpha}(t)\mathcal{G}(\boldsymbol{x} - \boldsymbol{x}^{\beta}(t)). \tag{5.14}$$

Combining Equations 5.13 and 5.14 gives

$$B =\frac{1}{2} \sum_{\alpha=1}^{N} \sum_{\beta=1}^{N} f_i^{\alpha\beta}(t) \left(\mathcal{G}(\boldsymbol{x} - \boldsymbol{x}^{\alpha}(t)) - \mathcal{G}(\boldsymbol{x} - \boldsymbol{x}^{\beta}(t))\right). \tag{5.15}$$

The fundamental theorem of calculus is used to obtain a line integral

$$\begin{aligned} &\int_a^b \frac{d\mathcal{G}(\boldsymbol{r}(t))}{dt}\, dt = G(\boldsymbol{r}(b)) - G(\boldsymbol{r}(a)) \\ \Rightarrow &\int_0^1 \frac{d\mathcal{G}(\boldsymbol{r}((b-a)s + a))}{ds}\, ds = G(\boldsymbol{r}(b)) - G(\boldsymbol{r}(a)). \end{aligned} \tag{5.16}$$

The path $\boldsymbol{r}(t)$ is arbitrary, and can thus be taken to be linear

$$\int_0^1 \frac{d\mathcal{G}((\boldsymbol{r}(b) - \boldsymbol{r}(a))s + \boldsymbol{r}(a))}{ds}\, ds = G(\boldsymbol{r}(b)) - G(\boldsymbol{r}(a)). \tag{5.17}$$

If we take $\boldsymbol{r}(a) = \boldsymbol{x} - \boldsymbol{x}^{\alpha}$ and $\boldsymbol{r}(b) = \boldsymbol{x} - \boldsymbol{x}^{\beta}$ then we have[1]

$$\begin{aligned} &\mathcal{G}(\boldsymbol{x} - \boldsymbol{x}^{\alpha}(t)) - \mathcal{G}(\boldsymbol{x} - \boldsymbol{x}^{\beta}(t)) \\ =& -\int_0^1 \frac{\partial}{\partial s}\mathcal{G}\left(\boldsymbol{x} - \boldsymbol{x}^{\alpha}(t) + s(\boldsymbol{x} - \boldsymbol{x}^{\beta}(t) - (\boldsymbol{x} - \boldsymbol{x}^{\alpha}(t))\right) ds \\ =& -\int_0^1 \frac{\partial}{\partial s}\mathcal{G}(\boldsymbol{x} - \boldsymbol{x}^{\alpha}(t) + s\boldsymbol{x}^{\alpha\beta}(t))\, ds. \end{aligned} \tag{5.18}$$

The multivariate chain rule is

$$\frac{\partial\mathcal{G}(\boldsymbol{r}(s))}{\partial s} = \nabla\mathcal{G}(\boldsymbol{r}(s)) \cdot \frac{\partial\boldsymbol{r}(s)}{\partial s}. \tag{5.19}$$

Thus we have

$$\begin{aligned} &\frac{\partial}{\partial s}\mathcal{G}(\boldsymbol{x} - \boldsymbol{x}^{\alpha}(t) + s\boldsymbol{x}^{\alpha\beta}) \\ =&\nabla\mathcal{G}(\boldsymbol{x} - \boldsymbol{x}^{\alpha}(t) + s\boldsymbol{x}^{\alpha\beta}) \cdot \frac{\partial}{\partial s}\left(\boldsymbol{x} - \boldsymbol{x}^{\alpha}(t) + s\boldsymbol{x}^{\alpha\beta}\right) \\ =&\nabla\mathcal{G}(\boldsymbol{x} - \boldsymbol{x}^{\alpha}(t) + s\boldsymbol{x}^{\alpha\beta}) \cdot \boldsymbol{x}^{\alpha\beta}. \end{aligned} \tag{5.20}$$

---

[1] Note that there is a typographical error in eqns 3.27 and 3.28 of Andreotti et al. (2013). They write $\boldsymbol{x}^{\beta}(t)$, but it should instead be $\boldsymbol{x}^{\alpha}(t)$.

Using the results in Equations 5.18 and 5.20, Equation 5.15 can be written as

$$\begin{aligned} B &= -\frac{1}{2}\sum_{\alpha=1}^{N}\sum_{\beta=1}^{N} f_i^{\alpha\beta}(t)x_j^{\alpha\beta}\int_0^1 \frac{\partial}{\partial x_j}\mathcal{G}(\boldsymbol{x}-\boldsymbol{x}^{\alpha}(t)+s\boldsymbol{x}^{\alpha\beta})\,ds \\ &= -\frac{\partial}{\partial x_j}\left(\frac{1}{2}\sum_{\alpha=1}^{N}\sum_{\beta=1}^{N} f_i^{\alpha\beta}(t)x_j^{\alpha\beta}\int_0^1 \mathcal{G}(\boldsymbol{x}-\boldsymbol{x}^{\alpha}(t)+s\boldsymbol{x}^{\alpha\beta})ds\right). \end{aligned} \tag{5.21}$$

Equation 5.10 now becomes

$$\begin{aligned} \frac{\partial\sigma_{ij}}{\partial x_j} = \frac{\partial}{\partial x_j}&\left(-m\sum_{\alpha=1}^{N}(v_i^{\alpha}(t)-v_i)\left(v_j^{\alpha}(t)-v_j\right)\mathcal{G}(\boldsymbol{x}-\boldsymbol{x}^{\alpha}(t))\right) \\ &-\frac{\partial}{\partial x_j}\left(\frac{1}{2}\sum_{\alpha=1}^{N}\sum_{\beta=1}^{N} f_i^{\alpha\beta}(t)x_j^{\alpha\beta}\int_0^1 \mathcal{G}(\boldsymbol{x}-\boldsymbol{x}^{\alpha}(t)+s\boldsymbol{x}^{\alpha\beta})\,ds\right). \end{aligned} \tag{5.22}$$

The stress thus becomes

$$\sigma_{ij}(\boldsymbol{x},t) = \sigma_{ij}^{k}(\boldsymbol{x},t) + \sigma_{ij}^{c}(\boldsymbol{x},t), \tag{5.23}$$

where the kinetic stress $\sigma_{ij}^{k}(\boldsymbol{x},t)$ and contact stress $\sigma_{ij}^{c}(\boldsymbol{x},t)$ are given by

$$\sigma_{ij}^{k}(\boldsymbol{x},t) = -\sum_{\alpha=1}^{N} m v'^{\alpha}_i(t)v'^{\alpha}_j(t)\mathcal{G}(\boldsymbol{x}-\boldsymbol{x}^{\alpha}(t)), \tag{5.24}$$

$$\sigma_{ij}^{c}(\boldsymbol{x},t) = -\frac{1}{2}\sum_{\alpha,\beta,\alpha\neq\beta} f_i^{\alpha\beta}(t)x_j^{\alpha\beta}(t)\int_0^1 \mathcal{G}(\boldsymbol{x}-\boldsymbol{x}^{\alpha}(t)+s\boldsymbol{x}^{\alpha\beta}(t))ds, \tag{5.25}$$

where $\boldsymbol{x}^{\alpha\beta} = \boldsymbol{x}^{\alpha} - \boldsymbol{x}^{\beta}$ and $\boldsymbol{v}'^{\alpha}(\boldsymbol{x},t) = \boldsymbol{v}^{\alpha}(t) - \boldsymbol{v}(\boldsymbol{x},t)$.

The kinetic stress can be interpreted as a kinetic-energy-like term, with the contribution coming from the particles with very high velocity. Gas-like systems will have a high kinetic stress. The contact stress arises from contact forces between particles. Solid-like systems will have a high contact stress. Systems with rapid-dense flow will have similar contributions from both types of stress. The magnitude of the kinetic stress $|\boldsymbol{\sigma}^{k}|$ and contact stress $|\boldsymbol{\sigma}^{c}|$ over the test space are shown, respectively, in Figure 5.3 and 5.4. The kinetic stress is of a greater magnitude in the downward flowing layer, which is flowing more rapidly than the rising layer. The highest kinetic stress appears near the toe region and is larger for the simulations with higher rotational speed.

The maximum contact stress is an order of magnitude larger than the kinetic stress. The contact stress exhibits the opposite behaviour to the kinetic stress, with large magnitude near the bottom of the rising layer. A slight decrease just next to the edge of the drum for the simulations with rotational speeds of 28 rpm and upwards can be observed. This corresponds to the slipping event that was observed in Chapter 3.

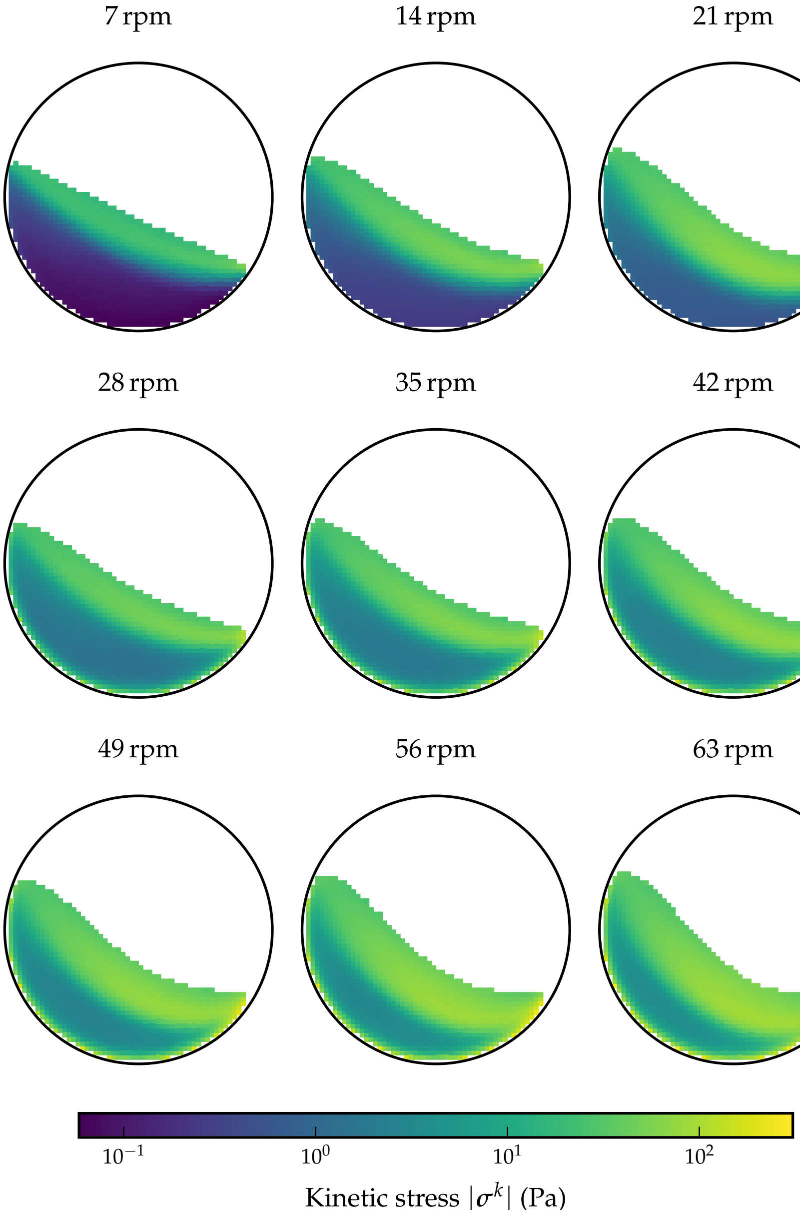

Figure 5.3: The magnitude of the kinetic stress $|\sigma^k|$ over the test space. The colours are mapped using a log scale.

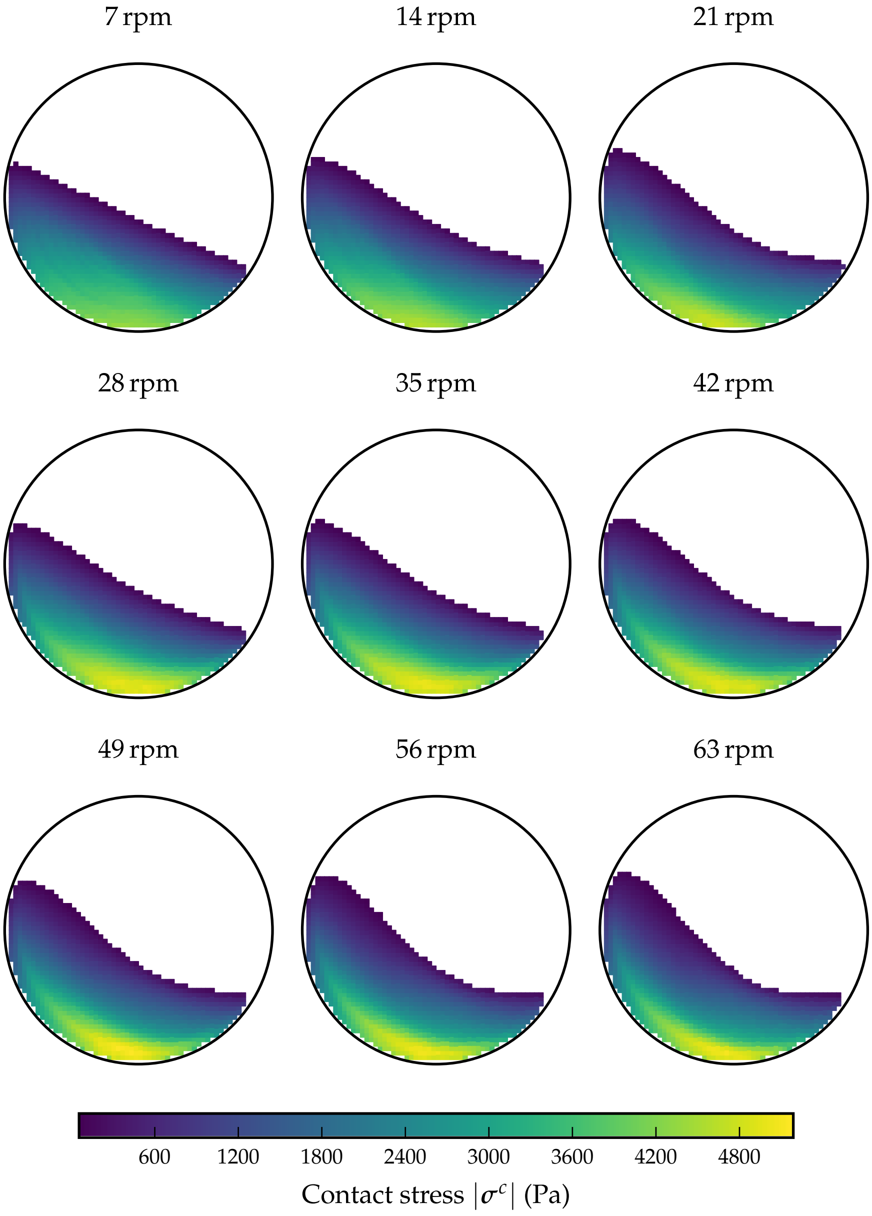

Figure 5.4: The magnitude of the contact stress $|\sigma^c|$ over the test space.

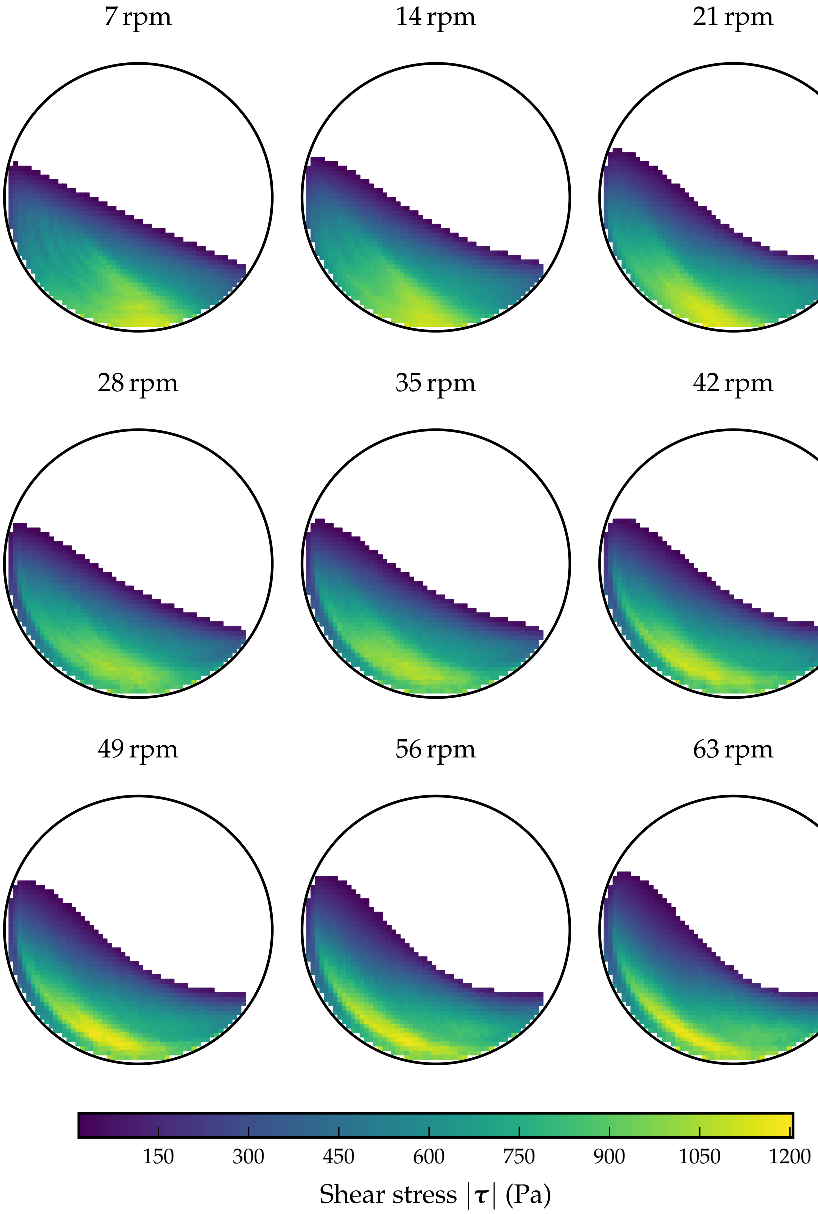

Figure 5.5: The magnitude of the shear stress $|\boldsymbol{\tau}|$ over the test space.

The shear stress $|\boldsymbol{\tau}|$ over the test space is shown in Figure 5.5. Narrow bands of high shear stress at roughly 45° from the horizontal can be seen in the 7, 14 and 21 rpm results. The pressure p over the test space is shown in Figure 5.6. Both the shear stress and pressure also exhibit the drop in magnitude near the edge of the drums for the 28 rpm simulations onwards.

5.5 VELOCITY GRADIENT

Recall that the velocity gradient is given by

$$\boldsymbol{L} = \frac{\partial \boldsymbol{v}}{\partial \boldsymbol{x}}. \tag{5.26}$$

The velocity for each particle α in the volumetric element can be approximated using a first order Taylor approximation as

$$\boldsymbol{v} \approx \boldsymbol{L}(\boldsymbol{x}^\alpha - \boldsymbol{x}^0) + \boldsymbol{v}^0, \tag{5.27}$$

where $\boldsymbol{x}^0$ and $\boldsymbol{v}^0$ are the averages of the position and the velocity, respectively, of all of the particles in the volumetric element. The problem of finding the velocity gradient thus becomes that of solving nine separate linear regression problems, i.e. finding L_{ij} for $i, j \in \{1, 2, 3\}$ in

$$\hat{v}_i^\alpha = L_{ij}\hat{x}_j^\alpha, \tag{5.28}$$

with $\hat{\boldsymbol{x}}^\alpha = \boldsymbol{x}^\alpha - \boldsymbol{x}^0$ and $\hat{\boldsymbol{v}}^\alpha = \boldsymbol{v}^\alpha - \boldsymbol{v}^0$. Using simple linear regression, the gradient becomes

$$L_{ij} = \frac{\sum_{\alpha=1}^N \hat{v}_i^\alpha \hat{x}_j^\alpha}{\sum_{\alpha=1}^N \hat{x}_j^\alpha \hat{x}_j^\alpha}. \tag{5.29}$$

The standard error of the gradient is given by

$$(S_L)_{ij} = \sqrt{\frac{\frac{1}{N-2}\sum_{\alpha=1}^N \hat{v}_i^\alpha - (L_{ij}\hat{x}_j^\alpha)^2}{\sum_{\alpha=1}^N (\hat{x}_j^\alpha)^2}}. \tag{5.30}$$

Figure 5.7 shows a plot of $\hat{v}_1$ vs $\hat{x}_2$ and the line of best fit (with gradient L_{12}) in a randomly chosen volumetric element. Figure 5.8 shows the magnitude of the velocity gradient $|\boldsymbol{L}|$ over the test space. Figure 5.9 shows the ratio of the norm of the standard error to the norm of the velocity gradient, i.e $|\boldsymbol{S}_L|/|\boldsymbol{L}|$. The standard error is low, i.e. $|\boldsymbol{S}_L|/|\boldsymbol{L}| \ll 1$, for most of the volumetric elements with the exception of a small number of elements on the free surface. These elements produce spurious results because they are not always uniformly packed and may sometimes be empty.

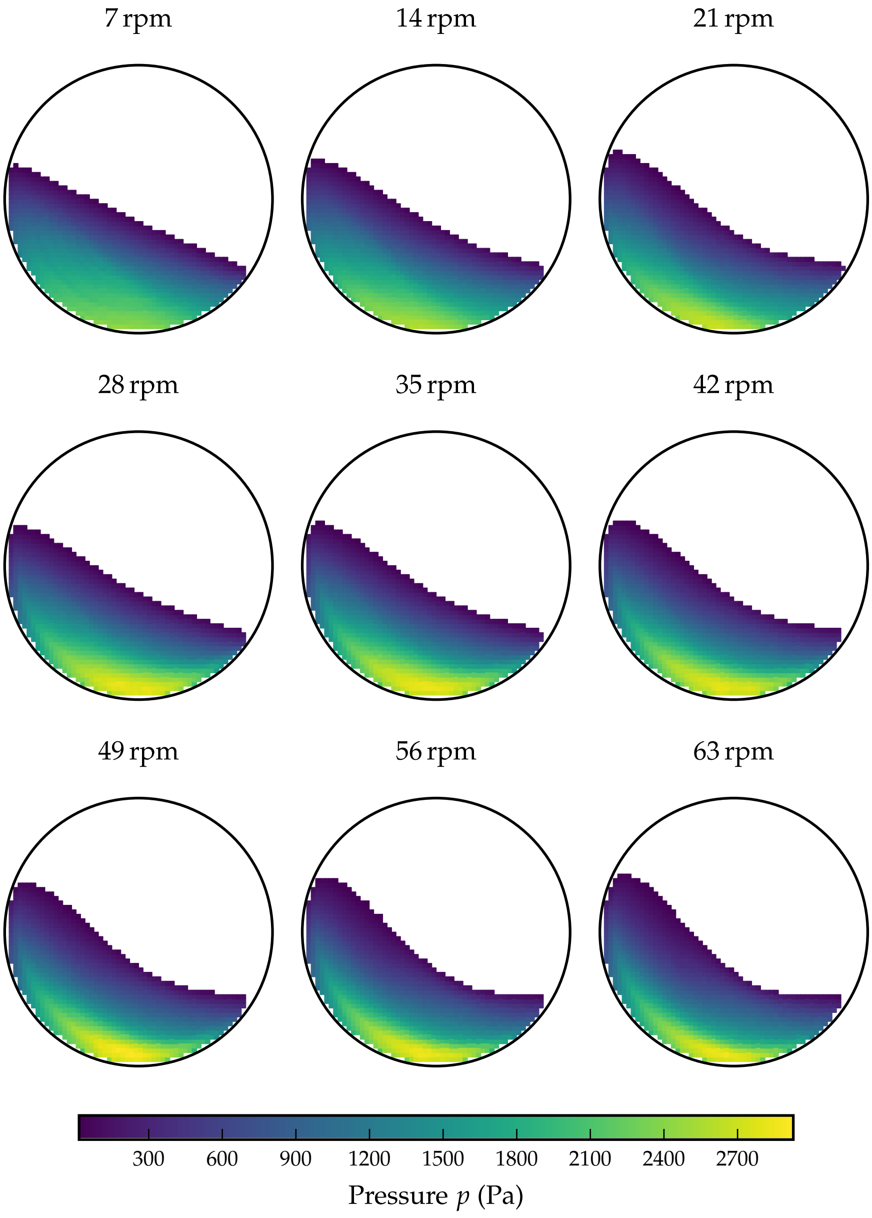

Figure 5.6: The pressure p over the test space.

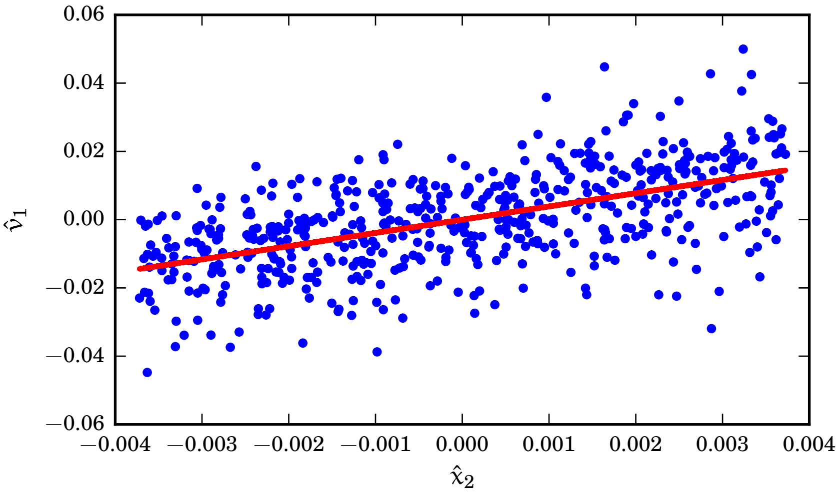

Figure 5.7: A plot of $\hat{v}_1$ vs $\hat{x}_2$ for ten snapshots of a volumetric element in the 63 rpm simulation. The line of best fit found from simple linear regression is also shown.

5.6 PACKING FRACTION

The packing fraction ϕ, also called the solidicity or volume fraction, is the fraction of volume of a volumetric element occupied by the particles. In this section, the method used to calculate the solidicity for rectangular-shaped volumetric elements is described.

Typically the packing fraction is calculated numerically by dividing the volumetric element into a grid (Malahe, 2012). A search is then done over all the particles to count the number of grid points they intersect. The packing fraction is then the number of grid points with intersections divided by the total number of grid points in the volumetric element. This method is computationally expensive. A more efficient method is to use analytical expressions for the volumes of intersections between the spheres and the volumetric element.

The packing fraction can be decomposed into two parts comprising the contributions from those particles completely inside the volumetric elements and those that have parts lying outside the volumetric elements. The decomposed solidicity is given by

$$\phi = \frac{1}{V_{\text{element}}} \left(\sum_{\alpha \in \boldsymbol{N}_{\text{inside}}} V_\alpha + \sum_{\beta \in \boldsymbol{N}_{\text{intersect}}} V_\beta \right), \tag{5.31}$$

where $\boldsymbol{N}_{\text{inside}}$ is the set of particles completely inside the the volumetric element, $\boldsymbol{N}_{\text{intersect}}$ is the set of particles that intersect the surface of the volumetric element, V_α is the volume of particle α and V_β is the volume of the intersection of particle β and the volumetric element.

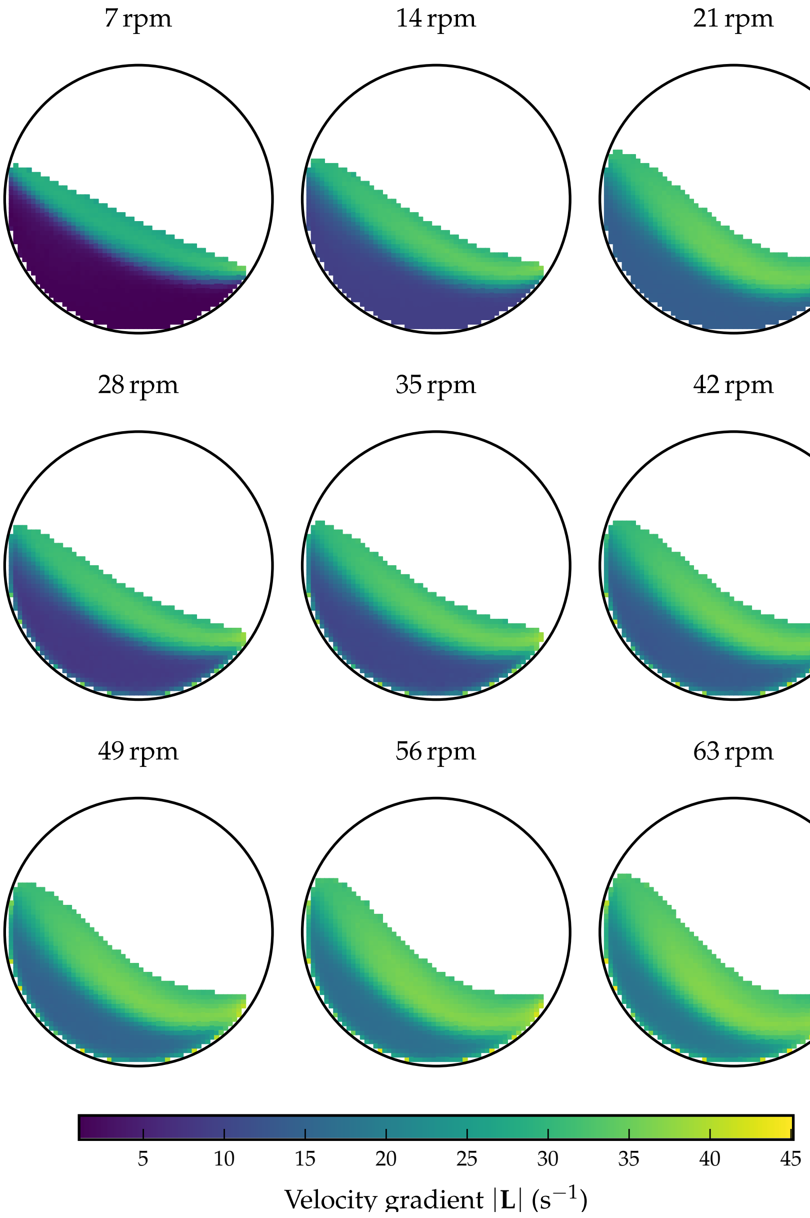

Figure 5.8: The magnitude of the velocity gradient $|\boldsymbol{L}|$ over the test space.

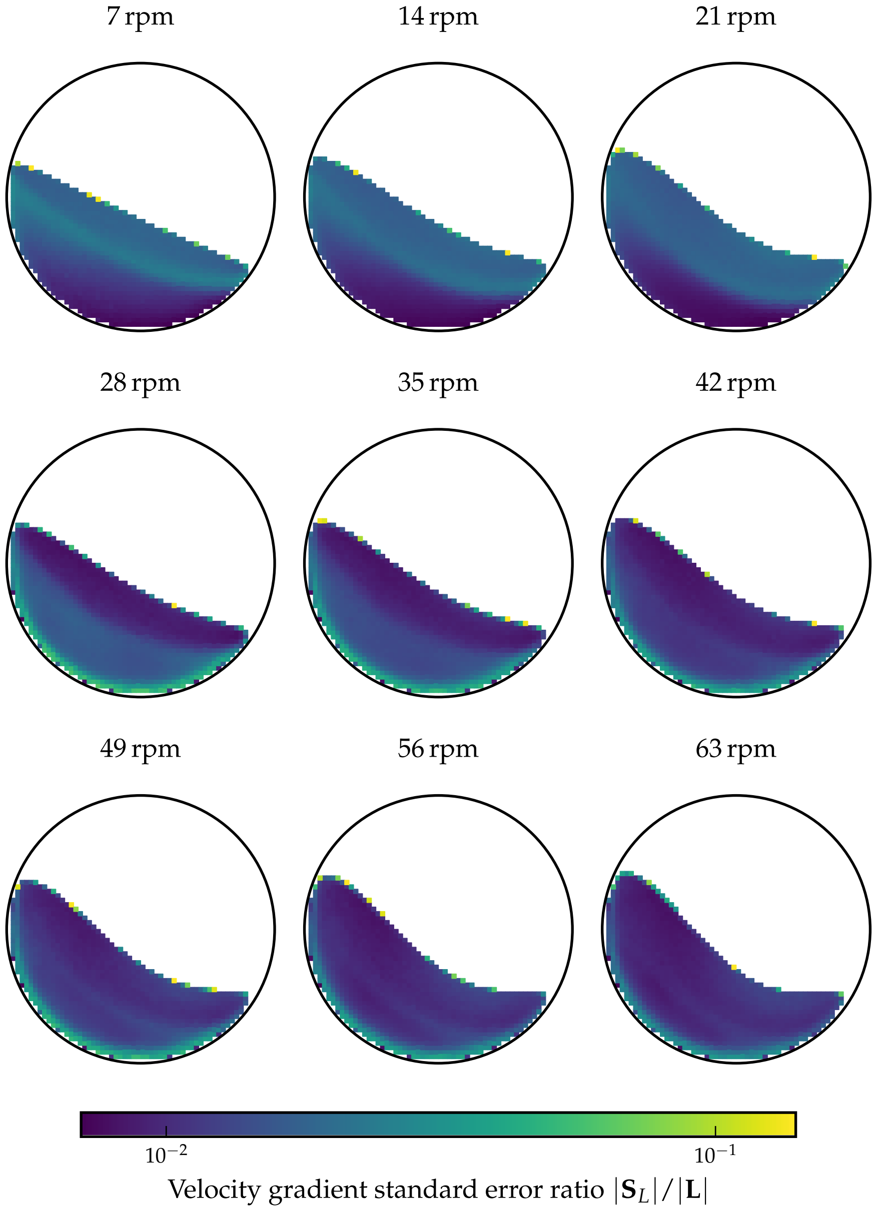

Figure 5.9: The ratio of the magnitude of the standard error $|\boldsymbol{S}_L|$ to the magnitude of the velocity gradient $|\boldsymbol{L}|$ over the test space. The colours are mapped using a log scale.

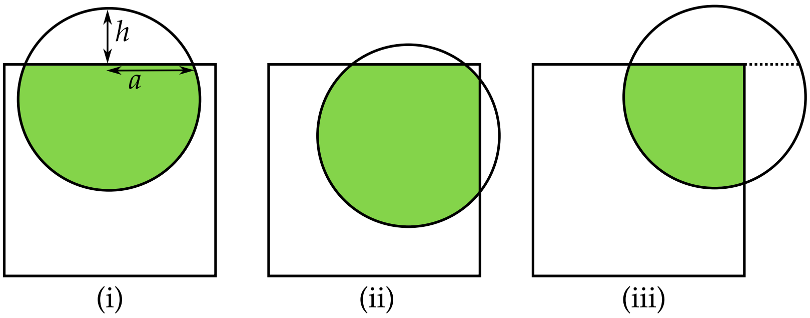

Figure 5.10: Three cases of a sphere intersecting a periodic volumetric element.

The periodicity of the system simplifies the calculation of the intersection for particles that are intersecting the volumetric element. The volumetric element spans the axis of rotation of the drum, and the particle will thus always intersect the volumetric element along this axis. Assuming that the volumetric element is at least as large as a particle diameter, the intersection is split into three cases:

i The particle intersects one face of the volumetric element.

ii The particle intersects two faces of the volumetric element, but no edges, i.e. the two sections are not joined.

iii The particle intersects two faces and an edge of the volumetric element, i.e. the sections are joined.

Figure 5.10 shows diagrams of the three cases. The volume of the intersection in case (i) and (ii) is the difference between the volume of the sphere and the volume of one and two spherical caps, respectively. The volume of a spherical cap is given by

$$V_{\text{cap}} = \frac{\pi h}{6}\left(3a^2 + h^2\right), \tag{5.32}$$

where h is the height of the cap and a is the radius of the base of the cap (see Figure 5.10). The volume of intersection for case (iii) is calculated by splitting the region outside the volumetric element into two parts, as shown by the dotted line in Figure 5.10. The first part is a spherical cap, so Equation (5.32) can be used. The other part is a sectioned spherical cap, the volume of which is not trivial to find analytically. Instead of using an analytical solution, the volumes of the sectioned spherical caps in case (iii) were approximated numerically. Note that there are sub-cases of case (i) and (iii) where the centre of the sphere is outside the volumetric element, in these cases the volume of the intersection is the volume of the caps or sections, rather than the difference.

The accuracy of this method is limited by the size of the grid used for the numerical calculation for the sectioned spherical cap in case (iii). There is a significant speed-up, however, when compared to the purely numerical calculation.

For equally-sized spheres in 3D the maximum packing fraction is 0.74 and a random packing has a fraction of around 0.64. The packing fraction over the test space is shown in Figure 5.11. The maximum packing fraction is around the same as the fraction for a random packing ($\phi \approx 0.64$). As may be expected the value of ϕ is higher in the rising layer than in the downward-flowing layer, due to the increase in pressure. A sharp layer of very high ϕ can be observed near the bottom edge of the drum for the 28 rpm and upwards results. The sharp layer is slightly offset from the edge of the drum. Immediately adjacent to the drum ϕ is slightly lower. Like the observations for the shear stress $\boldsymbol{\tau}$ in Figure 5.5, this corresponds to the slipping event.

5.7 APPROXIMATING THE LOCATION OF THE EQUILIBRIUM- AND FREE SURFACES

The equilibrium surface is defined as the surface that marks the boundary between the upward- and downward-flowing layers in the rotating drum system. The free surface is the surface that is created by the upper-most layer of particles of the flowing layer. The algorithms described in this section to approximate these two surfaces are implemented in Python scripts and make use of the Matplotlib Python library (Hunter, 2007). This library provides a large range of functions for plotting and analysis of data. In particular a Matplotlib routine that calculates a Delaunay triangulation from an unstructured set of points was used in the algorithms for both surfaces. The triangulations are created from the set of points made up of the centres of the volumetric elements that contain particles. An example triangulation from the 63 rpm simulation is shown in Figure 5.12.

5.7.1 *Equilibrium Surface*

One methodology devised here to determine the equilibrium surface can be stated as a problem of minimizing the path integral of the magnitude of the velocity of a set of points connecting the head and the toe, i.e.

$$\min_{S} \int_{S} |\boldsymbol{v}| \, dS, \tag{5.33}$$

where S is the path approximated from the straight lines joining all of the points. The velocity along the path is calculated from a linear interpolation of the data from the volumetric elements. The set points were allowed to move along the line joining the initial position of the point and another reference point located just beyond the opposite end of the drum.

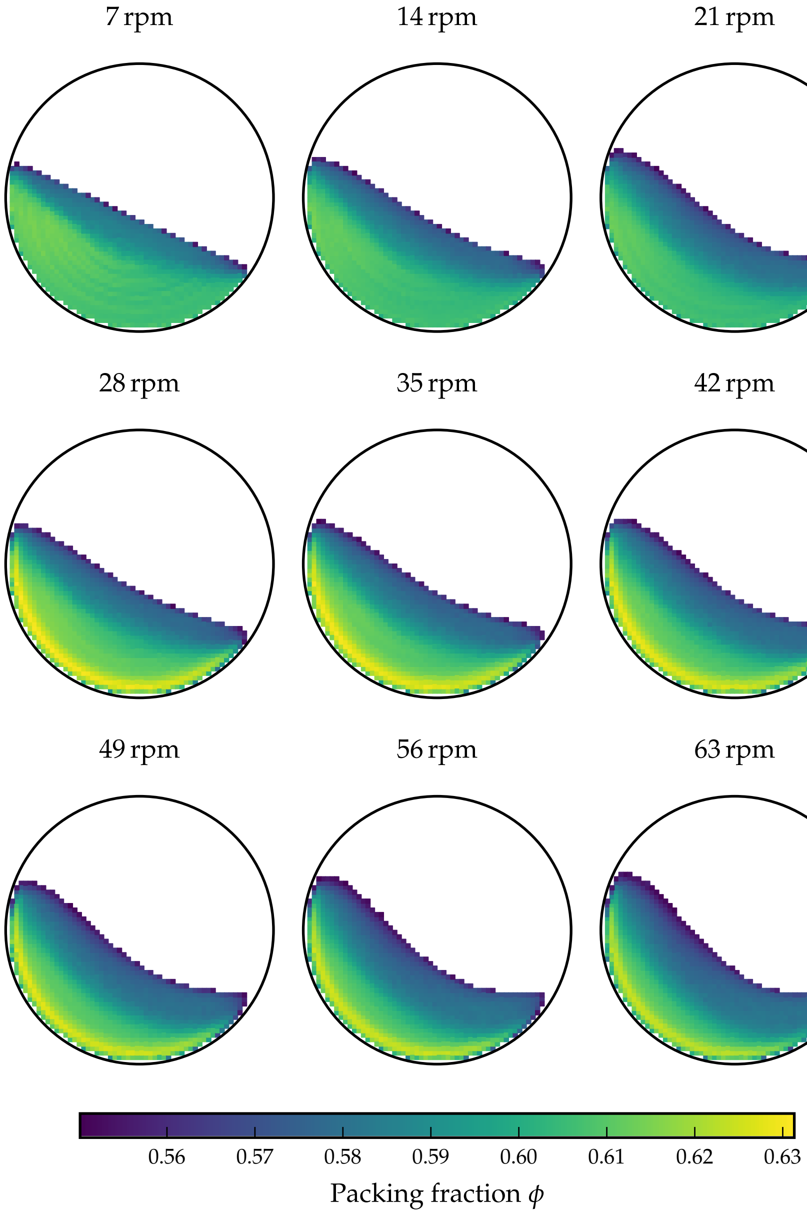

Figure 5.11: Packing fraction ϕ over the test space.

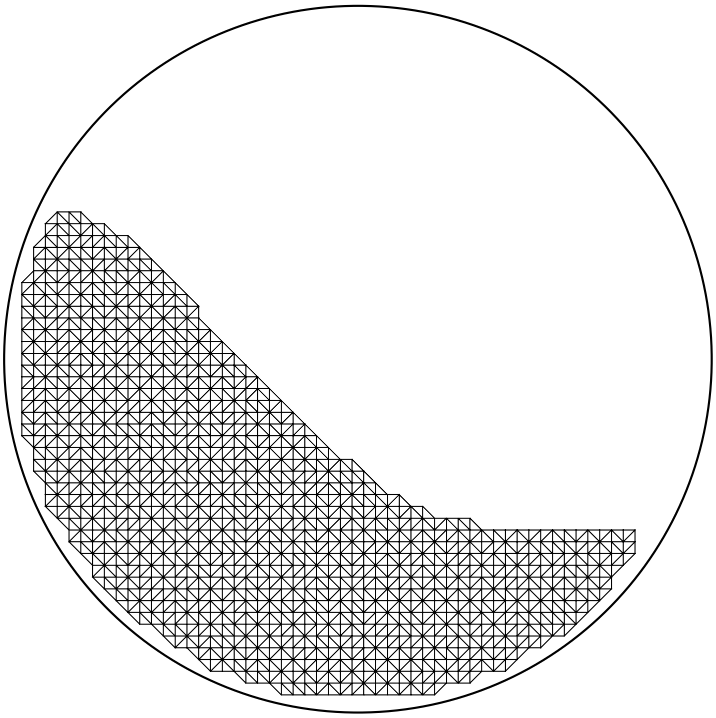

Figure 5.12: The triangulation of the 63 rpm system. Each node on the triangulation is the centre of a volumetric element that contains particles.

The algorithm was modified in order to decrease the computational cost. Initially a random-walk based algorithm was used to optimize the location of the points. Briefly, the algorithm worked by choosing one of the points at random; this point was then allowed to jump randomly along its line. If the new position of the point minimized the path integral it is kept, otherwise the point remains at the old position. An illustration of the set of lines and the point jumping is shown in Figure 5.13. The random distance of the jump was determined by a normal distribution. The mean of the normal distribution was tweaked to speed up the computation. The algorithm did obtain a minimum path integral, but was computationally expensive, even with tweaking. Eventually it was found that the optimum points coincided with the point along the line where the magnitude of the velocity $|v|$ was a minimum. The algorithm was then simplified to find the minimum velocity magnitude along each line. Algorithm 2 shows the final procedure that is used to calculate the equilibrium surface. This algorithm may not be robust enough to work on any rotating-drum system, especially with cataracting flows, but it works well for the systems considered here.

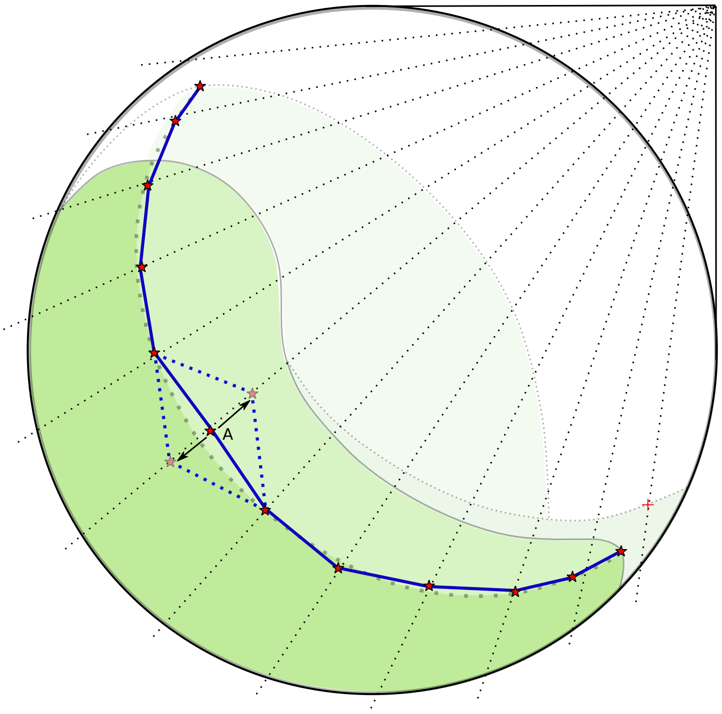

Figure 5.13: An illustration of a methodology to find the equilibrium surface: the randomly chosen point A is shifted randomly. The new point is accepted if the path integral of the magnitude of the velocity along the line joining the points (blue line) has decreased.

Algorithm 2 Algorithm to approximate the equilibrium surface.

- Start with a set of N equally spaced points $(\boldsymbol{P}_1, \boldsymbol{P}_2, \cdots, \boldsymbol{P}_N)$ between the head and toe of the flow.
- Associated with each point is a line that passes through the point and ends. The lines all meet at a point just beyond the opposite edge of the drum.
- Find where the equilibrium surface intersects each line, for each line:
  - Using a linear interpolation, find the point which corresponds to the minimum value of $|\boldsymbol{v}|$.
- Apply a smoothing function to the edges joining the points.

5.7.2 *Free surface*

The free surface is found by taking the set of upper edges of the Delaunay triangulation. A smoothing function is applied to the edges joining the points for the free surface. Figure 5.14 shows the equilibrium- and free-surfaces over the test space.

5.8 INERTIAL NUMBER

Recall from Equation 4.31 that the inertial number I is given by

$$I = \sqrt{2}|\boldsymbol{D}|d\sqrt{\frac{\rho}{p}}. \tag{5.34}$$

I can now be determined using the quantities calculated previously in this chapter. Figure 5.15 shows two histograms of the inertial number I for all of the elements in all of the simulations. The histograms have different bin spacing, Figure 5.15(a) has equally spaced bins on a linear scale and Figure 5.15(b) has equally spaced bins on a logarithmic scale. From the linearly scaled histogram it is apparent that there are a very large number of elements with very small inertial numbers. The logarithmically spaced histogram shows a relatively even spread of bin counts; this suggests that a logarithmic scale for the inertial number would be of greater use when investigating the relationship between other quantities.

The inertial number over the test space is shown, with a log-scale, in Figure 5.16. In the downward-flowing layer I is an order of magnitude higher than in the rising layer.

5.9 SUMMARY

In this chapter the methods used to obtain the continuum and material quantities in a granular system were described. The quantities are found by spatial averaging over a volumetric element and temporal averaging over snapshots of the system. A derivation of the stress $\boldsymbol{\sigma}$ over a generalized averaging function was given. The velocity gradient tensor $\boldsymbol{D}$ was found by solving nine separate linear regression problems. The technique used to calculate the packing fraction was outlined. This technique makes use of analytical and numerical methods for calculating the volume of the intersection between a sphere and a volumetric element. Algorithms for approximating the location of the free- and equilibrium-surfaces were given. Results for some of the averaged quantities were presented. Appendix A shows plots of a number of quantities interpolated over a line passing through the centre of circulation.

The results of the shear stress $\boldsymbol{\tau}$, pressure p and packing fraction ϕ show a difference in the results that corresponds to the slipping event

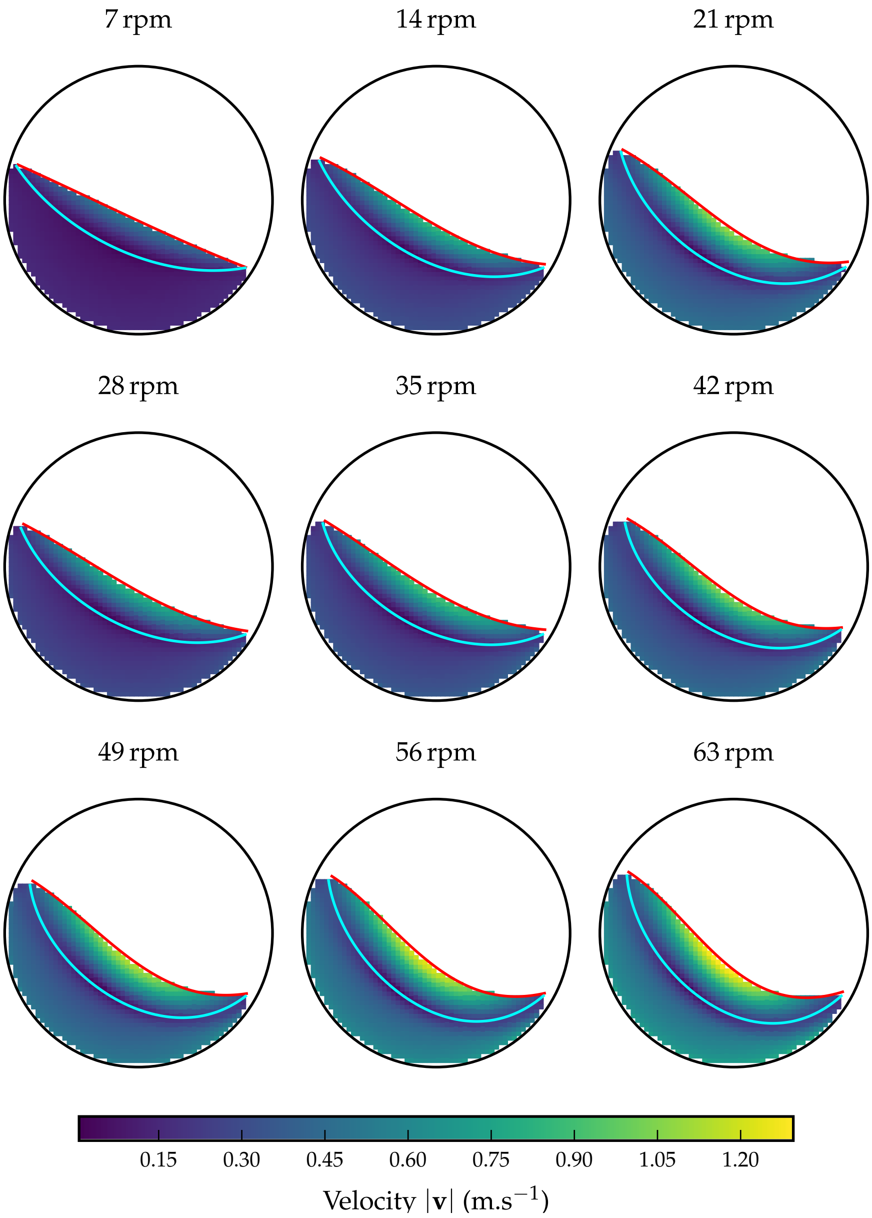

Figure 5.14: The equilibrium (cyan) and free surfaces (red) for each of the simulations. The elements are coloured according to the speed $|v|$. The equilibrium surfaces are obtained using Algorithm 2.

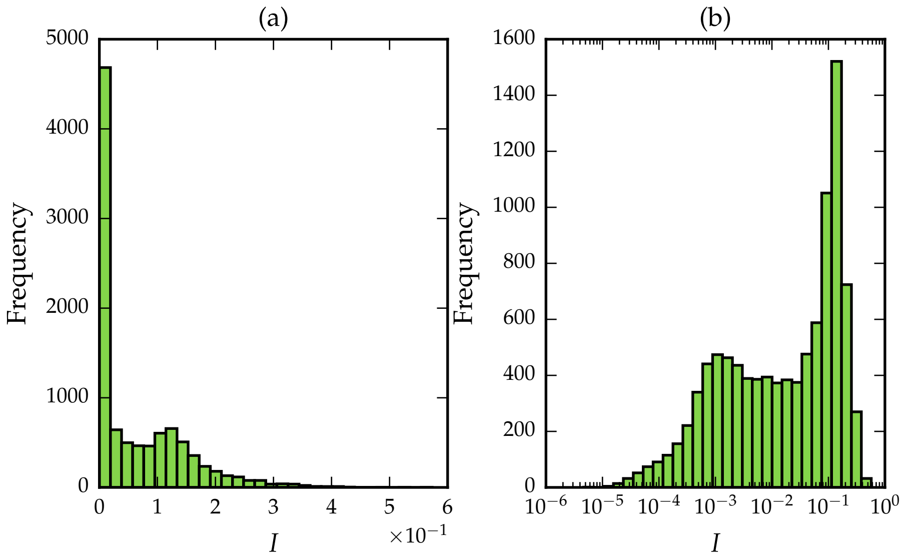

Figure 5.15: Histograms of the inertial number I. The bins in (a) are spaced evenly on a linear scale and the bins in (b) are spaced logarithmically

that was observed in Chapter 3. A fluidized layer appears right next to the bottom edge of the drum for the 28 rpm simulations onwards. This is a region where quasi-static flow is expected to be occurring. The fluidized layer is conjectured to be due to the increase in slipping occurring between the drum and the particles in contact with it.

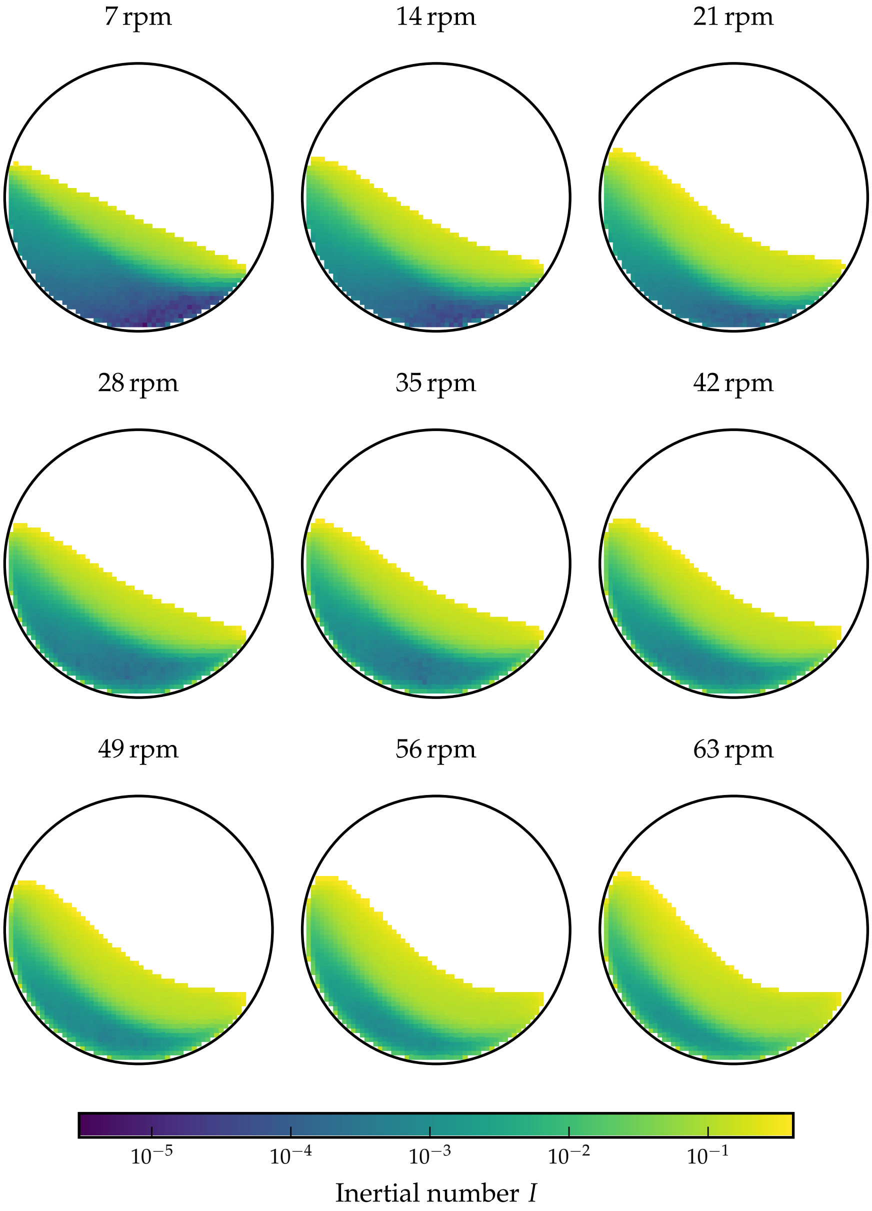

Figure 5.16: The inertial number I over the test space. The colours are mapped using a log scale.

6

INVESTIGATION OF CONSTITUTIVE LAWS

6.1 INTRODUCTION

The constitutive law of Jop et al. (2006) has been investigated in two-dimensional simulations of rotating drums (Cortet et al., 2009) and three-dimensional simulations of silo drainage (Rycroft et al., 2009).

The main purpose of this chapter is to use the spatio-temporally averaged quantities presented in Chapter 5 to investigate the validity of the constitutive law of Jop et al. over the test space: three-dimensional simulations of rotating drums performed over a range of 9 equally-spaced rotational speeds from 7 to 63 rpm. The rotating drum is a system of particular interest due to the wide range of flow regimes therein. The two key assumptions for Jop et al.'s constitutive law are that the system is incompressible and isotropic. The incompressibility condition arises from that assumption that the density in the system does not change. The above assumptions are tested and Jop et al.'s phenomenological friction coefficient is compared with the coefficient of da Cruz et al. (2005) as well as a new empirically-derived coefficient.

A necessary but not sufficient condition for isotropy is the coaxiality between the shear stress $\boldsymbol{\tau}$ and the symmetric velocity gradient $\boldsymbol{D}$. In addition, the respective principal directions of $\boldsymbol{\tau}$ and $\boldsymbol{D}$ must scale by the same amount. Satisfying these conditions ensures colinearity between $\boldsymbol{D}$ and $\boldsymbol{\tau}$. These two assumptions are investigated in this chapter using the material quantities extracted from volumetric elements that cover the whole domain. Both Cortet et al. (2009) and Rycroft et al. (2009) test isotropy by comparing $\boldsymbol{\tau}$ with the deviatoric of $\boldsymbol{D}$, rather than $\boldsymbol{D}$ itself (as done in this work). Taking the deviatoric (volume preserving part) of $\boldsymbol{D}$ enforces the assumption of incompressibility.

This chapter is arranged as follows. The incompressibility assumption is investigated in Section 6.2. A quantitative measure of coaxiality between $\boldsymbol{D}$ and $\boldsymbol{\tau}$ is described in Section 6.3. This measure is based on the angular separation between the principal directions of the respective tensors. The relationship between the inertial number and the measure of coaxiality is also investigated. The scaling between the respective principal directions of $\boldsymbol{\tau}$ and $\boldsymbol{D}$ is investigated in Section 6.4. The friction coefficient is investigated in section 6.5. The packing fraction ϕ is investigated in Section 6.6.

6.2 COMPRESSIBILITY

The constitutive relation of Jop et al. requires the constitutive response of the system to be incompressible. The volumetric component of the symmetric velocity gradient must therefore be zero, i.e.

$$\mathrm{tr}(\boldsymbol{D}) = \nabla \cdot \boldsymbol{v} = 0. \tag{6.1}$$

Figure 6.1 shows the divergence of the velocity for each of the simulations. The rising layer has approximately zero divergence for the simulations. The downward-flowing layer shows a small amount of expansion and contraction. Expansion ($\nabla \cdot \boldsymbol{v} > 0$) appears to occur in the upper part of the flowing layer and a small amount of compression ($\nabla \cdot \boldsymbol{v} < 0$) occurs in the bottom half of the flowing layer. As the upward-flowing particles reach the maximum height and start flowing downwards the decrease in pressure allows expansion to happen. When the particles reach the bottom of the flowing layer the particles "behind" them in the flowing layer exert a pressure, which compresses the region near the edge of the drum.

Another way of representing the incompressibility constraint is given by

$$\boldsymbol{D} = \boldsymbol{D}_{\mathrm{dev}}, \tag{6.2}$$

where $\boldsymbol{D}_{\mathrm{dev}}$ is the deviatoric (volume preserving) component of the symmetric velocity gradient, given by

$$\boldsymbol{D}_{\mathrm{dev}} = \boldsymbol{D} - \frac{1}{3}\mathrm{tr}(\boldsymbol{D})\boldsymbol{I}. \tag{6.3}$$

The volumetric component of $\boldsymbol{D}$ is therefore

$$\boldsymbol{D}_{\mathrm{vol}} = \boldsymbol{D} - \boldsymbol{D}_{\mathrm{dev}}. \tag{6.4}$$

In an incompressible system $\boldsymbol{D}_{\mathrm{vol}} = \boldsymbol{0}$. The ratio of the norms of $\boldsymbol{D}_{\mathrm{vol}}$ and $\boldsymbol{D}_{\mathrm{dev}}$ over the test space are shown in Figure 6.2. Over most of the test space the contribution of $\boldsymbol{D}_{\mathrm{vol}}$ to $\boldsymbol{D}$ is negligible relative to $\boldsymbol{D}_{\mathrm{dev}}$. The area at the bottom of the drum appears to have a larger volumetric component; this becomes more pronounced for the more slowly-rotating simulations with a few volumetric elements having a high ratio ($|\boldsymbol{D}_{\mathrm{vol}}|/|\boldsymbol{D}_{\mathrm{dev}}| \approx 1$). In their analyses Cortet et al. (2009) and Rycroft et al. (2009) both compare the deviatoric $\boldsymbol{D}_{\mathrm{dev}}$, rather than $\boldsymbol{D}$, with the shear stress $\boldsymbol{\tau}$. In this work the full symmetric velocity gradient $\boldsymbol{D}$ is compared to $\boldsymbol{\tau}$, as this is a more accurate representation of Jop et al.'s rheology.

6.3 COAXIALITY

Recall the three-dimensional constitutive law of Jop et al. given in Equation 2.10 by

$$\boldsymbol{\tau} = \mu(I)\frac{p}{|\boldsymbol{D}|}\boldsymbol{D}. \tag{6.5}$$

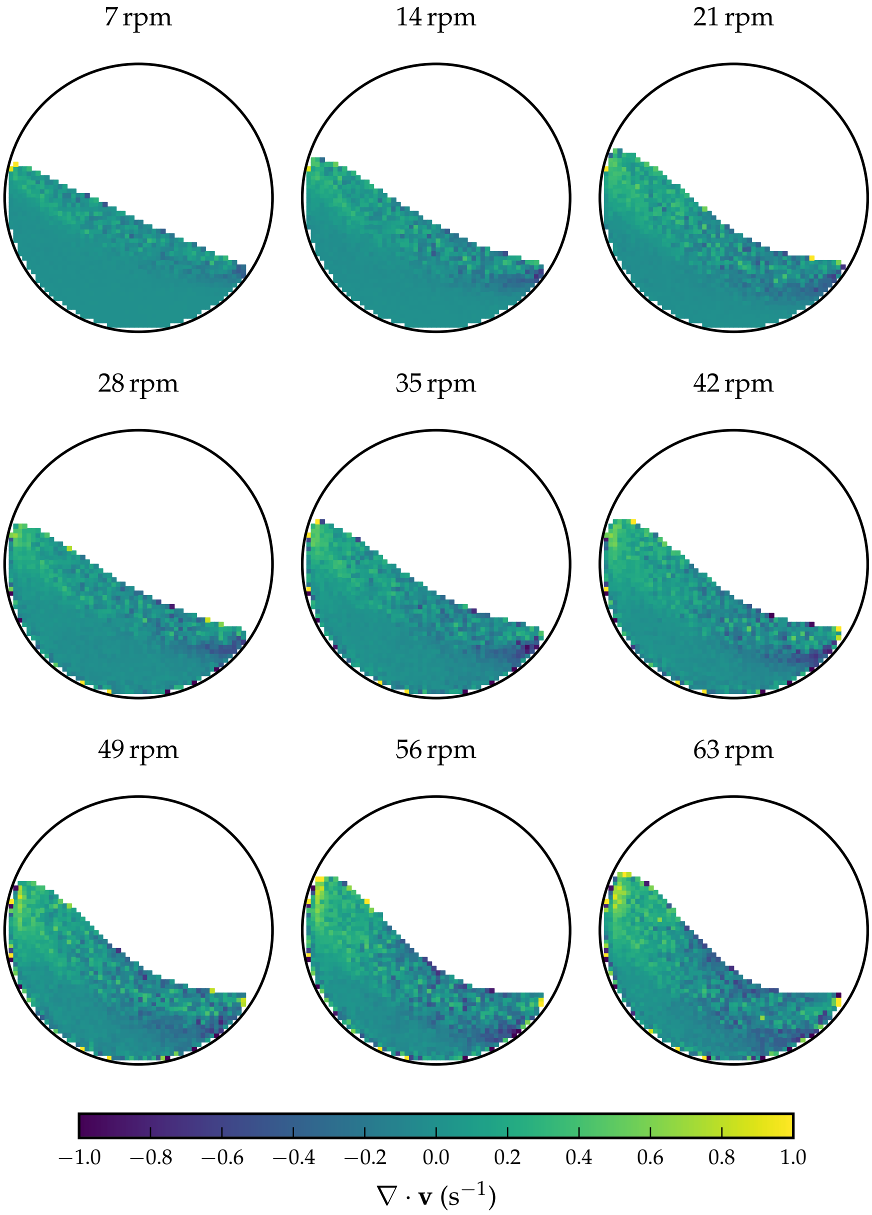

Figure 6.1: The divergence of the velocity $\nabla \cdot v$ over the test space. The colourbar is truncated from -1 to 1 as there are several volumetric elements with very high magnitude of $\nabla \cdot v$. These results are spurious, as they arise from partially-filled volumetric elements at the free surface.

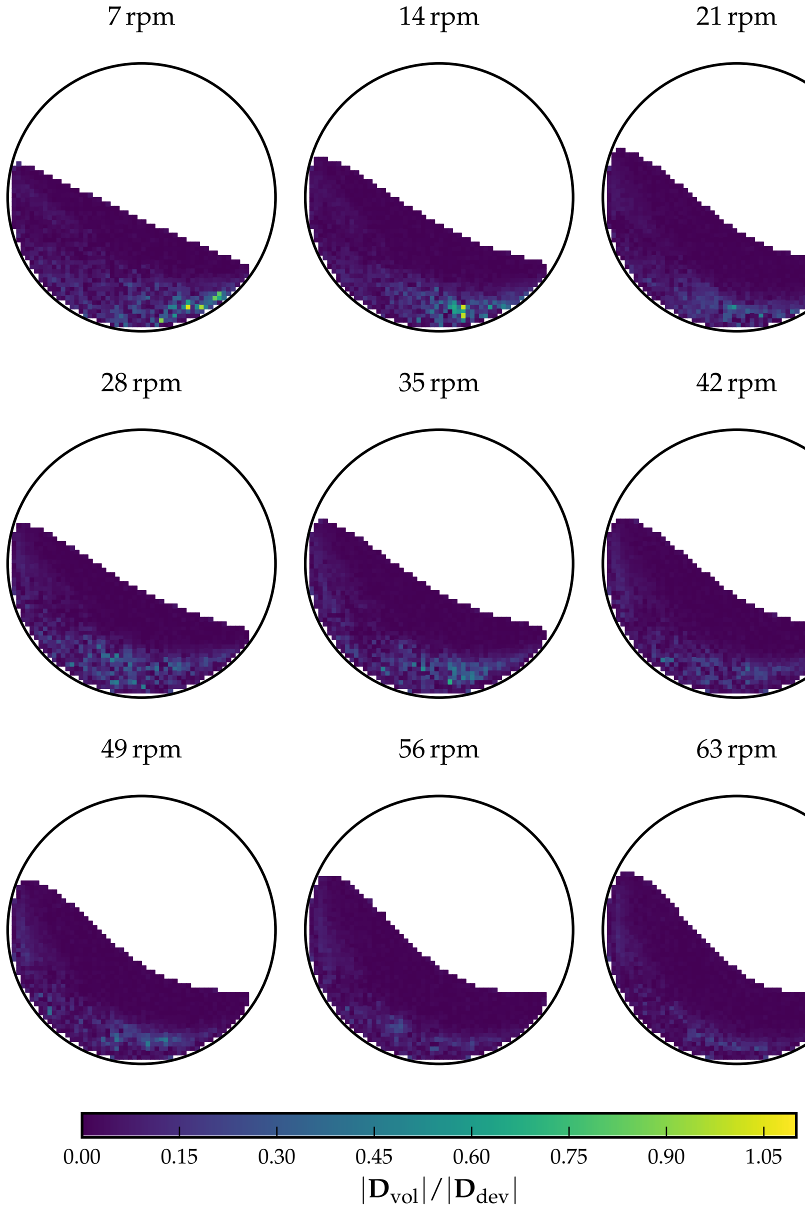

Figure 6.2: The ratio of the volumetric and deviatoric components of the symmetric velocity gradient $|\boldsymbol{D}_{\text{vol}}|/|\boldsymbol{D}_{\text{dev}}|$ over the test space.

As outlined in Chapter 4, this form of constitutive law requires the material to be isotropic and incompressible. The isotropy condition implies that the tensors $\boldsymbol{D}$ and $\boldsymbol{\tau}$ must be colinear. A simple test for colinearity is to check whether one tensor is a scalar multiple of the other; this is, however, not useful in quantifying the extent to which two tensors are colinear. In order to quantify the isotropy of the system the colinearity requirement is split into two sub-conditions:

1. The principal directions of the tensors $\boldsymbol{D}$ and $\boldsymbol{\tau}$ must align.
2. The respective principal values of the tensors $\boldsymbol{D}$ and $\boldsymbol{\tau}$ must scale by the same amount.

Both conditions need to be satisfied for the tensors to be coaxial. In this section the coaxiality condition is investigated. A new measure of coaxiality is proposed and used. In Section 6.4 the colinearity condition is investigated.

A real-valued second-order symmetric tensor $\boldsymbol{T}$ can be expressed as

$$\boldsymbol{T} = \sum_{i=1}^{r} \lambda_i \boldsymbol{v}_i \otimes \boldsymbol{v}_i, \tag{6.6}$$

where $\lambda_1 > \ldots > \lambda_r$ and $\boldsymbol{v}_1, \ldots, \boldsymbol{v}_r$ are, respectively, the principal values and principal directions of the tensor and r is the rank of the tensor (in this case $r = 3$). By definition the shear rate tensor $\boldsymbol{D}$ is symmetric. Given a sufficiently sized volumetric element, the stress $\boldsymbol{\sigma}$, and thus the shear component of the stress $\boldsymbol{\tau}$ are symmetric. The shear stress and the deformation gradient can thus be decomposed using equation (6.6) as

$$\boldsymbol{\tau} = \sum_{i=1}^{3} \zeta_i \boldsymbol{t}_i \otimes \boldsymbol{t}_i \quad \text{and} \quad \boldsymbol{D} = \sum_{i=1}^{3} \delta_i \boldsymbol{d}_i \otimes \boldsymbol{d}_i, \tag{6.7}$$

where $\boldsymbol{d}_i$ and $\boldsymbol{t}_i$ are the principal directions of $\boldsymbol{D}$ and $\boldsymbol{\tau}$, respectively. Similarly, ζ_i and δ_i are the respective principal values. Considering that the system being studied is periodic, one of the principal directions will be approximately along the axis of rotation of the drum. Both tensors will have the principal direction along the axis, so it is ignored when testing for coaxiality. The principal directions of symmetric tensors are orthogonal to one another, so the two remaining principal directions of $\boldsymbol{D}$ and $\boldsymbol{\tau}$ will lie in the plane of rotation. The extent to which $\boldsymbol{D}$ and $\boldsymbol{\tau}$ are coaxial can be quantified by comparing the angle between the two sets of principal directions of $\boldsymbol{D}$ and $\boldsymbol{\tau}$. The measure of coaxiality is denoted by θ and is taken to be the smallest angle between any two principal directions in the plane of rotation, as shown in the diagram in Figure 6.3.

Figure 6.4 shows the measure of coaxiality θ for each volumetric element in all of the simulations that were performed. There is a region

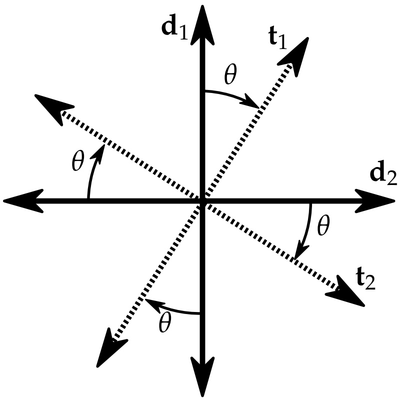

Figure 6.3: A diagram illustrating the measure of coaxiality θ, which is obtained by finding the smallest angular difference between the principal directions $\boldsymbol{t}_i$ and $\boldsymbol{d}_i$ in the plane of rotation of the drum.

at the bottom of the drum, in the rising layer, with a large measure of coaxiality ($\theta > 10^{\circ}$). This region gets smaller as the speed of rotation increases. The region also corresponds to the region in the 7, 14 and 21 rpm simulations where shear bands were observed (Figure 5.5). The downward-flowing quasi-static and rapid-dense flow regions at the top of the drum tend to have low values of the coaxiality measure ($\theta < 10^{\circ}$). The areas with high θ correspond to the areas where $\boldsymbol{D}_{\text{vol}}$, the volumetric component of the symmetric velocity gradient, is non-negligible (see previous section). To ensure that the compressibility of $\boldsymbol{D}$ does not influence the coaxiality measure, the analyses in this section and the next were re-run with the deviatoric $\boldsymbol{D}_{\text{dev}}$ instead of $\boldsymbol{D}$. The plots from the replicated analyses are shown in Appendix B. The results were not affected by the change.

Cortet et al. (2009) performed DEM simulations on a two-dimensional rotating drum with the same diameter. Figure 6.5 shows Cortet et al.'s angular separation for a drum rotating at 12 rpm alongside the measure of coaxiality for the 14 rpm simulation that was done in this work. The results of Cortet et al. are qualitatively the same. A low measure of coaxiality ($\theta < 10^{\circ}$) is visible in the flowing layer and a high value ($\theta > 10^{\circ}$) is visible in the rising layer. A more quantitative comparison can be done using Figure 6.6, which shows the normalized frequency of the coaxiality measure for the same data as in Figure 6.5. Cortet et al.'s data has a much larger proportion of elements with high measure of coaxiality ($\theta > 10^{\circ}$).

In order to calculate the measure of coaxiality the principal values of both $\boldsymbol{\tau}$ and $\boldsymbol{D}$ must be unique. If the principal values are not unique then the principal directions are not unique. The uniqueness of ζ_1 and

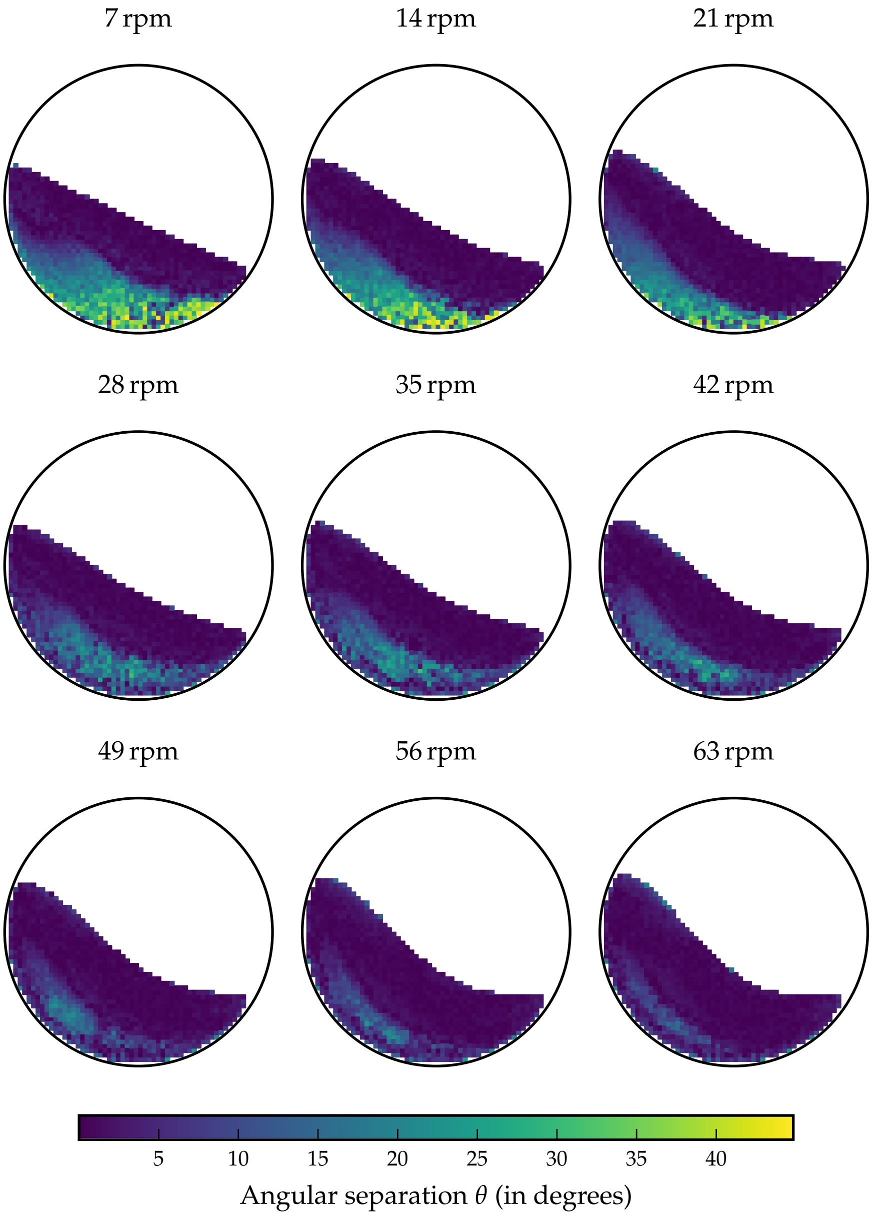

Figure 6.4: The measure of coaxiality θ over the test space.

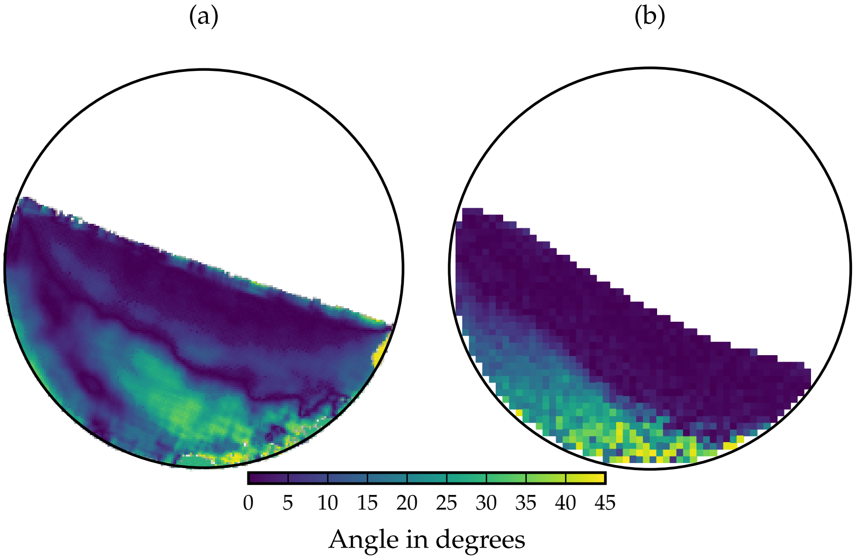

Figure 6.5: The measure of coaxiality from (a) the 12 rpm simulation of Cortet et al. (2009) (b) the 14 rpm simulation in this work. In order to get a better qualitative comparison, the data for (a) was extracted digitally from Figure 6a of Cortet et al. (2009) and converted to the same colour map as (b).

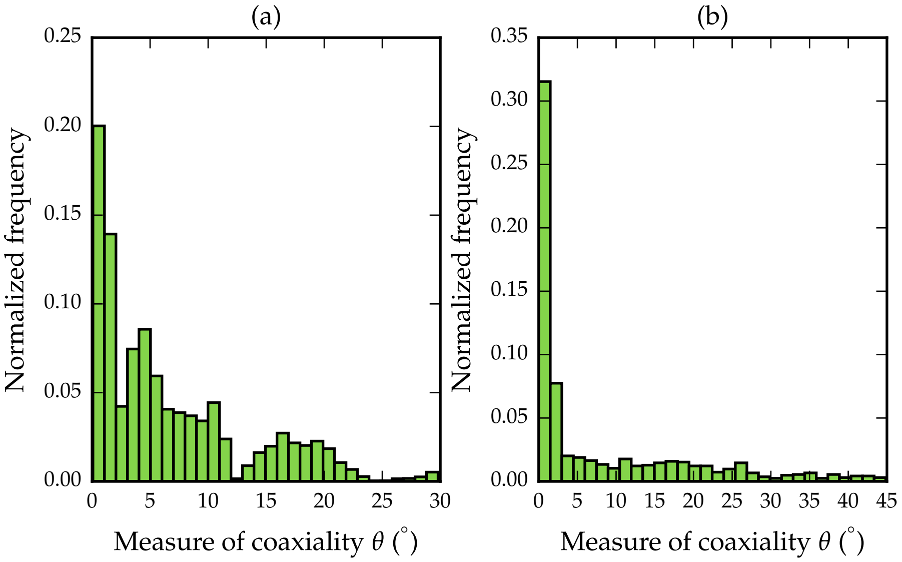

Figure 6.6: Histograms showing the normalized frequency of the measure of coaxiality θ for (a) the 12 rpm simulation of Cortet et al. (2009) and (b) the 14 rpm simulation in this work. The data for (a) was digitally extracted from Figure 6a of Cortet et al. (2009).

ζ_2, the principal values of $\boldsymbol{\tau}$ in the plane of rotation, can determined by finding their normed difference ζ_Δ, this is given by

$$\zeta_\Delta = \frac{|\zeta_1 - \zeta_2|}{|\zeta_1| + |\zeta_2|}. \tag{6.8}$$

If $\zeta_\Delta \approx 0$ then $\zeta_1 \approx \zeta_2$. For all of the volumetric elements it was found that $\zeta_\Delta = 1.0$; this indicates that all of the principal values are unique and additionally that the principal values have opposite sign (one under compression and the other under tension). Similarly, the normed difference for the principal values of $\boldsymbol{D}$ is given by

$$\delta_\Delta = \frac{|\delta_1 - \delta_2|}{|\delta_1| + |\delta_2|}. \tag{6.9}$$

In all of the volumetric elements in the test space, except three in the 7 rpm simulation, the normed difference was found to be $\delta_\Delta = 1.0$. The three exceptions had a non-zero normed difference ($\delta_\Delta > 0.64$), so all of the principal values of $\boldsymbol{D}$ in the test space are unique. The uniqueness of the principal values of $\boldsymbol{\tau}$ and $\boldsymbol{D}$ over the test space indicates that the measure of coaxiality is a meaningful way to quantify the anisotropy.

The results from Figure 6.4 show that the volumetric elements with slowly moving particles, in the rising layer, have more anisotropy between $\boldsymbol{D}$ and $\boldsymbol{\tau}$; this is especially pronounced for the slower simulations. The low velocity and high pressure in the slower simulations allows local effects such as jamming and shear banding to dominate in the rising layer. Recall that small values of the inertial number $I < 10^{-2}$ correspond to quasi-static flow. Figure 6.7 shows the measure of coaxiality θ vs the inertial number I over the test space. The volumetric elements in the quasi-static regime ($I < 10^{-2}$) have a much lower degree of coaxiality (higher θ) and the rapidly flowing volumetric elements have a high degree of coaxiality.

The set of histograms in Figure 6.8 show the distribution of the measure of coaxiality θ for each of the simulations in the test space. Details on how to interpret the figure are given in the accompanying caption. The figure allows one to observe the change in the distribution of the coaxiality measure as the rotational speed of the drum increases over the test space. At low rotational speeds there appear to be two groups of volumetric elements: those with a high measure of coaxiality ($\theta > 10^\circ$) and those with a very low measure of coaxiality ($\theta \sim 1^\circ$). As the rotational speed increases, the group of volumetric elements with a larger measure of coaxiality diminishes in size, the measure of coaxiality for this group also decreases and finally appears to merge with the other group in the 56 rpm simulation. At the same time the group of volumetric elements with a small measure of coaxiality increases in size as the rotational speed increases. Most of the volumetric elements for the 56 and 63 rpm simulations have $\theta \sim 1^\circ$.

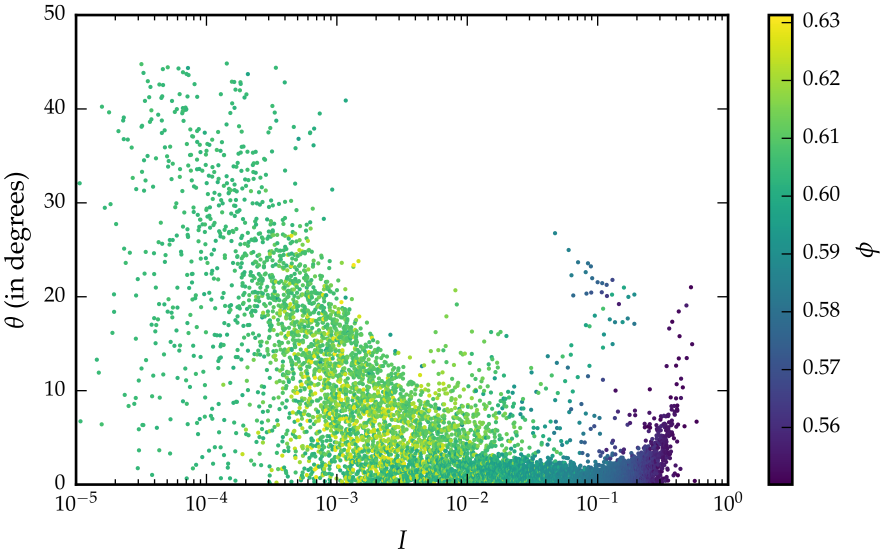

Figure 6.7: The measure of coaxiality θ vs the inertial number I over the test space. The points are coloured by the packing fraction ϕ.

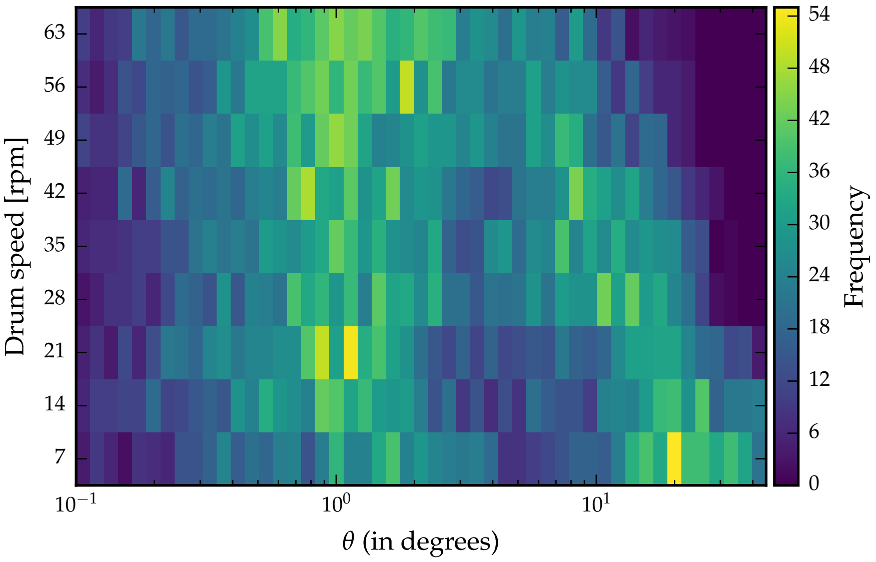

Figure 6.8: A set of histograms of the measure of coaxiality θ. Each row of cells is a histogram for one of the simulations. From the bottom row upwards the rows are arranged in ascending order of rotational speed. The rotational speed is shown on the vertical axis. Each row/histogram is divided into 50 bins. The bins are equally spaced in log space. The frequency of volumetric elements in each bin is represented by the colour.

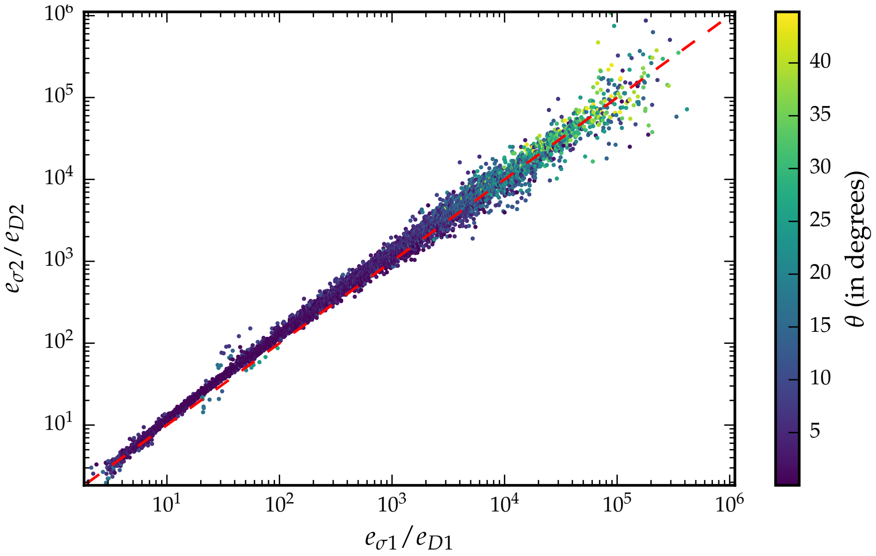

Figure 6.9: The scaling between the maximal principle directions of $\boldsymbol{\tau}$ and $\boldsymbol{D}$ for the volumetric elements in all of the simulations vs that of the minimal principle directions. The points are coloured by the measure of coaxiality θ. For reference the line $\frac{\zeta_1}{\delta_1} = \frac{\zeta_2}{\delta_2}$ is included.

The above results agree with the assertion of Barker et al. (2015) that Jop et al.'s rheology will more accurately describe 3D granular systems. The non-coaxial region at the bottom of the slowly-rotating simulations corresponds to Barker et al.'s expected zones of ill-posedness.

6.4 COLINEARITY

The colinearity condition requires that the corresponding principle values of the shear stress $\boldsymbol{\tau}$ and the symmetric velocity gradient $\boldsymbol{D}$ scale by the same amount, i.e.

$$\frac{\zeta_1}{\delta_1} = \frac{\zeta_2}{\delta_2} = \frac{\zeta_3}{\delta_3}. \tag{6.10}$$

Figure 6.9 shows the ratio between the corresponding principal directions of $\boldsymbol{\tau}$ and $\boldsymbol{D}$ in the plane of rotation of the drum for all of the bins in all of the simulations performed. From this figure it appears that the volumetric elements that do not have $\frac{\zeta_1}{\delta_1} = \frac{\zeta_2}{\delta_2}$ are elements with a large measure of coaxiality ($\theta > 10^{\circ}$). Figure 6.10 is a histogram showing the frequency of the points in Figure 6.9. From this figure it is apparent that the large majority of volumetric elements have $\frac{\zeta_1}{\delta_1} = \frac{\zeta_2}{\delta_2}$. Since the volumetric elements that satisfy the first condition for isotropy (as mentioned in Section 6.3) also satisfy the second condition, the measure of coaxiality θ can therefore be used as a measure for the isotropy in the systems in the test space.

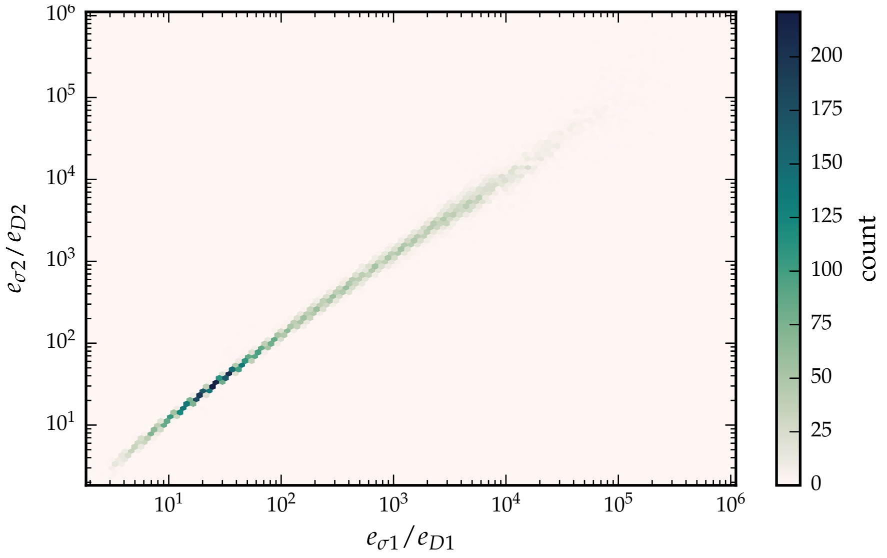

Figure 6.10: A hexagonal histogram showing the frequency of the scaling between the maximal principle directions of $\boldsymbol{\tau}$ and $\boldsymbol{D}$ for the volumetric elements in all of the simulations vs that of the minimal principle directions.

6.5 FRICTION COEFFICIENT

The results from the previous sections show that the rotating drum system becomes more isotropic as the rotational speed increases. The next step in examining the constitutive law of Jop et al. (2006) is to investigate the effective friction. The constitutive law (Equation 6.5) can be rearranged to give

$$\mu(I)\frac{\boldsymbol{D}}{|\boldsymbol{D}|} = \frac{\boldsymbol{\tau}}{p} \tag{6.11}$$

$$\Rightarrow \mu(I) = \frac{|\boldsymbol{\tau}|}{p}. \tag{6.12}$$

da Cruz et al. (2005) found a linear relationship between μ and I, given by

$$\mu(I) = \mu_{\min} + bI, \tag{6.13}$$

with constants $\mu_{\min} \simeq 0.25$ and $b \simeq 1.1$.

Jop et al. (2005) proposed a sigmoidally-shaped relation given by

$$\mu(I) = \mu_1 + \frac{\mu_2 - \mu_1}{I_0/I + 1}, \tag{6.14}$$

with constants $\mu_1 = \tan(20.9^\circ)$, $\mu_2 = \tan(32.76^\circ)$ and $I_0 = 0.279$.

Figures 6.11 and 6.12 show the friction coefficient μ versus the inertial number I for all of the bins in all of the simulations performed, with the points being coloured by the coaxiality measure θ. Figure

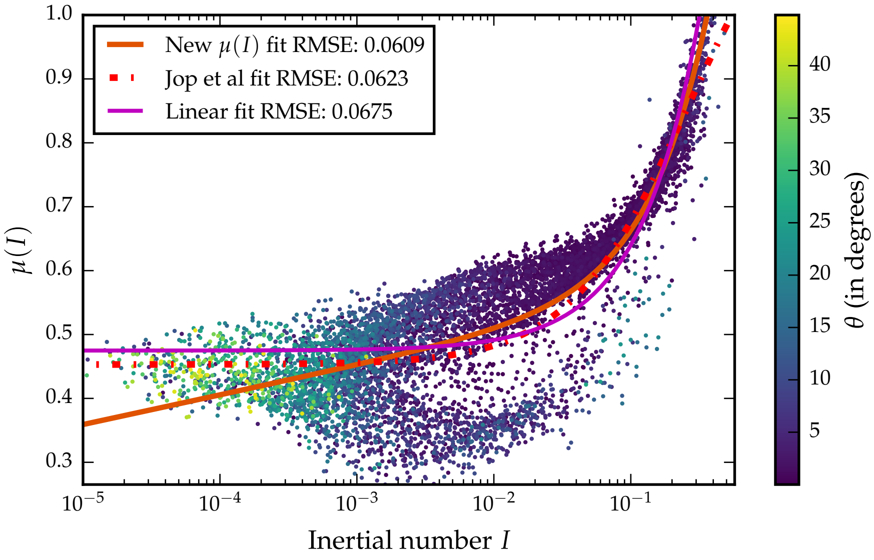

Figure 6.11: The friction coefficient μ vs the inertial number I, with a log-scale, over the test space. The points are coloured by the measure of coaxiality θ

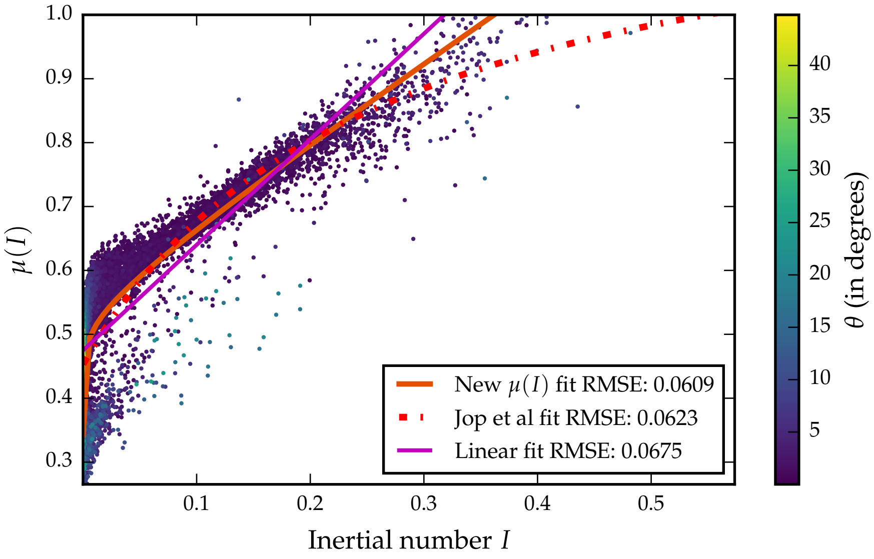

Figure 6.12: The friction coefficient μ vs the inertial number I over the test space. The points are coloured by the measure of coaxiality θ

6.11 shows the data with a log-scale for I and Figure 6.12 shows the data with a linear-scale for I. Figure 6.12 shows that for large values of inertial number ($I > 10^{-1}$) the effective friction $\mu(I)$ is approximately linear. In Figure 6.11 it appears that μ is linear for small values of I, i.e. $\mu(I) = c + d\log(I)$. Based on these observations the following effective friction is proposed:

$$\mu(I) = c + d\log(I) + eI, \tag{6.15}$$

where c, d and e are constants.

Figures 6.11 and 6.12 also show the least-squares fit of the linear $\mu(I)$ of da Cruz et al. (2005), the sigmoidal $\mu(I)$ of Jop et al. (2005) and the $\mu(I)$ proposed above (Equation 6.15). The least-squares fit parameters for the sigmoidal $\mu(I)$ found $\mu_1 = \tan(24.4^{\circ}) \pm \tan(0.1^{\circ})$, $\mu_2 = \tan(51.6^{\circ}) \pm \tan(1.8^{\circ})$, $I_0 = 0.261 \pm 0.017$ and the root-mean-squared error RSME $= 0.0623$. The linear least-squares fit of $\mu(I)$ found the intercept $\mu_{\text{min}} = \tan(25.4^{\circ}) \pm \tan(0.1^{\circ})$ and slope $b = 1.65 \pm 0.02$ with RMSE $= 0.0675$. The least-squares fit of Equation 6.15 found $c = 0.591 \pm 0.005$, $d = 0.020 \pm 0.001$ and $e = 1.19 \pm 0.02$ with RMSE $=$ 0.0609. The RMSE for the newly proposed law is the lowest of the three fitted laws. The RMSE for the sigmoidal law of Jop et al. (2006) is smaller than the linear law. All three laws capture the linear shape of the higher inertial number ($I > 10^{-1}$). The new law appears to capture the behaviour for lower I better than the other two.

The effective friction on a line passing through the centre of the drum was also considered by Cortet et al.. They found no agreement with Jop et al.'s rheology. A possible explanation for the disagreement may be due to the finding by Barker et al. (2015) of the ill-posedness of Jop et al.'s rheology in 2D. Barker et al. suggested that the 3D results may agree better with with Jop et al.'s rheology, when compared with 2D results.

While the three proposed laws may fit the data for higher inertial numbers, it is apparent that for lower inertial numbers ($I < 10^{-2}$) they do not capture the behaviour accurately. The friction coefficient appears to diverge for lower inertial numbers and takes on a "hook"-like shape. For some inertial number $I < 10^{-2}$ there are multiple possible values of the friction coefficient. It is likely that local effects can make a significant contribution to the friction coefficient at low inertial numbers. Hysteresis has also been observed in the transition between quasi-static flow and fluid-like flow in granular materials (Rajchenbach, 1990). A constitutive law that can fully describe the behaviour for these inertial numbers would have to take into account local influences.

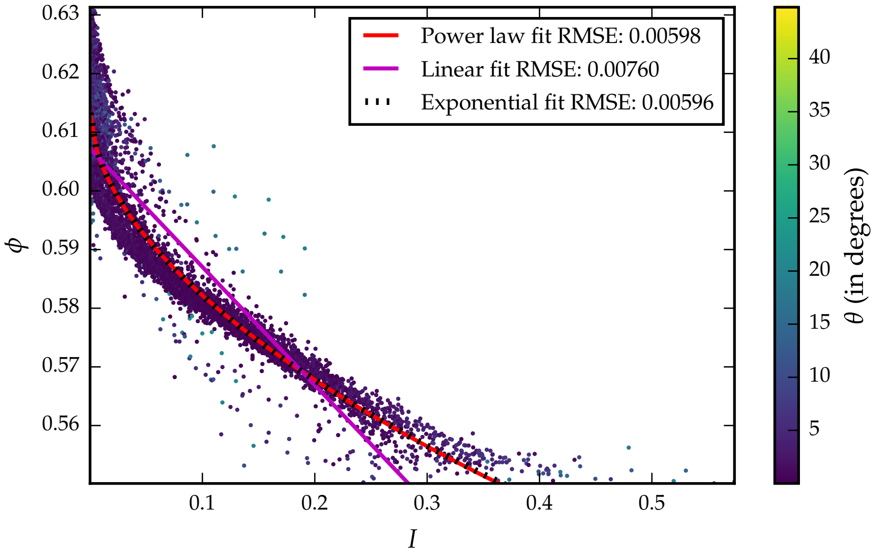

Figure 6.13: The packing fraction ϕ versus the inertial number I over the test space. The points are coloured by the measure of coaxiality θ. Least-squares fits for linear, power-law, and exponential functions are included.

6.6 PACKING FRACTION

The packing fraction ϕ for each simulation is shown in Figure 5.11. da Cruz et al. (2005) found a linear relationship between the packing fraction ϕ and the inertial number I,

$$\phi(I) = \phi_{\text{max}} - aI \tag{6.16}$$

with constants $\phi_{\text{max}} \simeq 0.81$, $a \simeq 0.3$. The linear relationship was later confirmed by Rycroft et al. (2009). Hatano (2007) found that a power law was a better fit for the data, that is,

$$\phi(I) = \phi_{\text{max}} - bI^{c}, \tag{6.17}$$

where the constants were found to be $b = 0.11$ and $c = 0.56 \pm 0.02$. Pathmathas (2015) proposed an exponential law, given by

$$\phi(I) = \phi_{\text{max}} e^{-dI^{f}}, \tag{6.18}$$

where ϕ_{max} is the maximum packing fraction and the constants were found to be $d = 1.348$, $f = 0.6014$.

Figures 6.13 and 6.14 show, respectively, linear and log-linear plots of the packing fraction ϕ versus the inertial number I over the test space with least-squares best fits of the linear, power and exponential laws. The root-mean-squared error for the least-squares fit of the power law was found to be RMSE $= 0.00598$ and the error for the fit of the exponential law was found to be RMSE $= 0.00596$. The constants

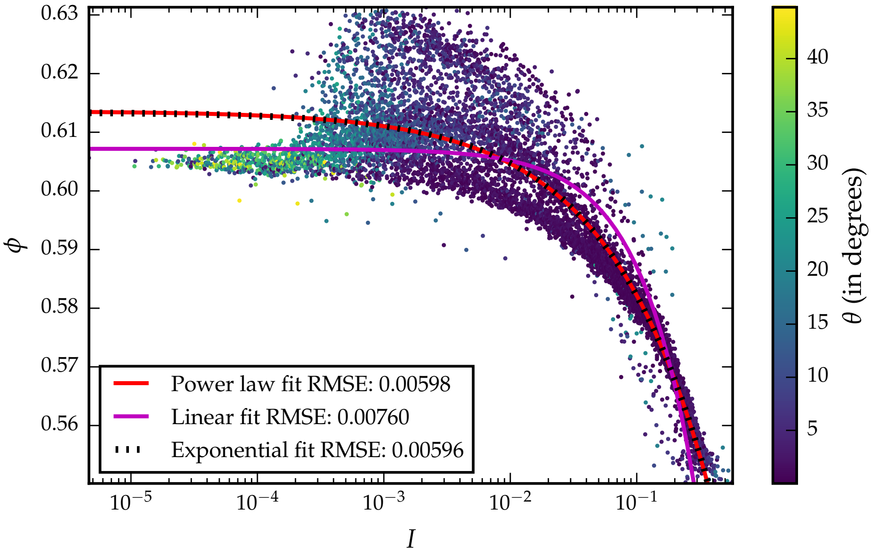

Figure 6.14: A log-linear plot of the packing fraction ϕ versus the inertial number I over the test space. The points are coloured by the measure of coaxiality θ. Least-squares fits for linear, power-law, and exponential functions are included.

for the power law were found to be $\phi_{\text{max}} = 0.6135 \pm 0.0003$, $b = 0.110 \pm 0.002$ and $c = 0.545 \pm 0.11$. The constants for the exponential law of Pathmathas were found to be $\phi_{\text{max}} = 0.6134 \pm 0.0003$, $d = 0.191 \pm 0.003$ and $f = 0.563 \pm 0.11$. The constants for the linear fit were found to be $\phi_{\text{max}} = 0.6071 \pm 0.0002$ and $a = 0.2014 \pm 0.002$. The root-mean-squared error was found to be RMSE $= 0.00760$.

With the lowest RMSE, Hatano's power law is the best-fit for the data from the test space. The RMSE is similar to that of the exponential law and the two curves are indistinguishable in Figures 6.13 and 6.14. Compared to the other two fits, the linear fit is poor. Rycroft et al. found good agreement with the linear law. The better fit may be due distribution of the inertial numbers. The results from the test space have a larger proportion of elements with higher inertial number ($I > 0.1$), when compared with Rycroft et al.'s results.

6.7 CONCLUSION

In this chapter the three-dimensional constitutive law of Jop et al. (2006) was investigated. The assumptions of isotropy and incompressibility were evaluated by examining the continuum measures from nine simulations of a rotating drum with varying speed. The inertial number-friction coefficient and inertial number-packing fraction relationships were also investigated.

The results in this chapter show that the assumptions of the constitutive law of Jop et al. are mostly valid for the rotating drums in the test space. The law was found to be more accurate for the simulations with a higher rotational speed. At low speeds the rising layer displays anisotropy. The anisotropy may be due to nonlocal effects as shear banding was observed in the same region as the anisotropy.

Tumbling mills used in the mining industry operate at high rotational speeds, further work should be done on simulating tumbling mills using a numerical algorithm such as finite-differences with Jop et al.'s law. Compressible constitutive laws may be worth investigating further, as a small amount of compressibility was observed for the downward-flowing layer in all simulations. Finally, further work on nonlocal constitutive laws, such as those proposed by Kamrin et al. (2012), may help provide a more accurate description and may be able to capture the anisotropy that was observed for slower rotational speeds.

7

SCALING RELATIONS

7.1 INTRODUCTION

A scaling law is a relationship between non-dimensional quantities derived from a system. Buckingham's Pi theorem (Bertrand, 1878; Buckingham, 1914) is typically the first step taken towards uncovering a scaling law. Briefly, the theorem states that if a system of l dimensions with p physical variables $(q_1, q_2, \cdots, q_p)$ has a physically meaningful equation $f(q_1, q_2, \cdots, q_p)$, that equation can be rewritten in terms of $s = p - l$ dimensionless parameters, i. e. $f(\pi_1, \pi_2, \cdots, \pi_s)$. For the systems simulated here there are 4 parameters: particle size d, particle density ρ_p, shear rate $\dot{\gamma}$ and pressure p. The systems are 3D, so $l = 3$ and therefore there is $4 - 3 = 1$ dimensionless parameter (Andreotti et al., 2013). The inertial number I is one such representation of this parameter; this was used to develop the $\mu(I)$ friction law (Pouliquen, 1999; da Cruz et al., 2005; Jop et al., 2005). In addition to a constitutive choice for the shear stress $\boldsymbol{\tau}$ a model for the velocity is needed to understand the dynamical behaviour of a system.

The relationship between the velocity of the particles in the flowing layer and the thickness of the layer is key scaling relation for the flow of a layer of particles down a slope. The downward flowing layer of particles in continuously rotating drums can be viewed as a continuously flowing layer of particles down a slope. The slope in this case is the equilibrium surface. In this chapter a number of variations of the flowing layer-thickness scaling are investigated. The section of flowing layer that is measured starts at a point some distance from the head and ends at a point some distance from the toe. The first varied quantity is the length of the section of flowing layer; this is varied by moving the start and end points. Second, the orientation of the coordinate system, from which the tangent velocity is calculated, is varied. Third, the flow rate is measured as the total average flow and the tangential average. These various scenarios for the velocity-thickness scaling are investigated in the test space (nine simulations of a periodic rotating drum with varying rotational speed). The scaling for each scenario is investigated by fitting a power law to the data, and comparing the results with the literature. These scenarios are investigated because the literature on flowing layer scaling is not consistent on the choice of these quantities. Assessing all of these scenarios may help explain differences in results from the literature.

The second scaling law that is investigated is the relationship between the flux through the flowing layer and the angle of repose of the bed.

The angle of repose φ is the angle between the free surface and the horizontal. Here φ is calculated in two ways: one is a constant for the whole system and the other is dependent on the location. The constant repose is the angle the semi-major axis of an ellipse that is fitted to the equilibrium surface makes with the horizontal. The location-dependent repose is the angle the tangent to the free surface makes with the horizontal.

This chapter is arranged as follows. The scaling of the flowing layer thickness with the velocity is discussed in Section 7.2. The scaling between the angle of repose, found using an ellipse fitting routine, and the rotational speed of the drum is investigated in Section 7.3.

7.2 FLOWING LAYER THICKNESS

The flowing layer is the region that lies between the equilibrium and free surfaces. A key scaling law in the flowing layer is the relationship between the thickness and the flux. In the literature the velocity and thickness scaling law in a rotating drum is usually investigated by measuring the flux along a line that is perpendicular to the both the free and equilibrium surfaces and passes through the middle of the flowing layer, as shown in Figure 2.2. Measuring over a line through the middle ensures that the influence of boundary effects are minimized. The velocity field is also largely parallel to the free surface near the middle of the flowing layer. The middle is also the thickest part of the flowing layer. Jain et al. (2002) and Govender et al. (2016) sampled over more than just the middle of the flowing layer. Jain et al. divided the flowing layer into 20 bins, the average velocity and thickness was calculated for each bin. In order to test if the scaling law applies to other parts of the flowing layer, Govender et al. took measurements of the thickness and velocity over 14 equally-spaced slices through the flowing layer. These slices were oriented such that they were perpendicular to the free surface. They found that their linear scaling law ($\langle v_t \rangle \propto h^1$), where $\langle v_t \rangle$ is the average tangential velocity through the flowing layer and h is the thickness), is representative of the whole flowing layer.

In this work measurements are taken in a similar manner to Govender et al. (2016): from equally spaced slices through the flowing layer. In this case 20 slices are taken. In addition, the length of the section of the flowing layer is varied. Consider the measure s, which is the % value that is omitted from the flowing layer near the head and toe. For example, $s = 10$ means that 10% is omitted from both the head and toe and the 20 slices are taken through the middle 80% of the flowing layer, see for example Figures 7.2 and 7.3. Four scenarios are considered in this section: $s = 10$ (middle 80%), $s = 20$ (middle 60%), $s = 30$ (middle 40%) and $s = 40$ (middle 20%). Figure 7.1 shows the slices corresponding to the four values of s for the 35 rpm simulation.

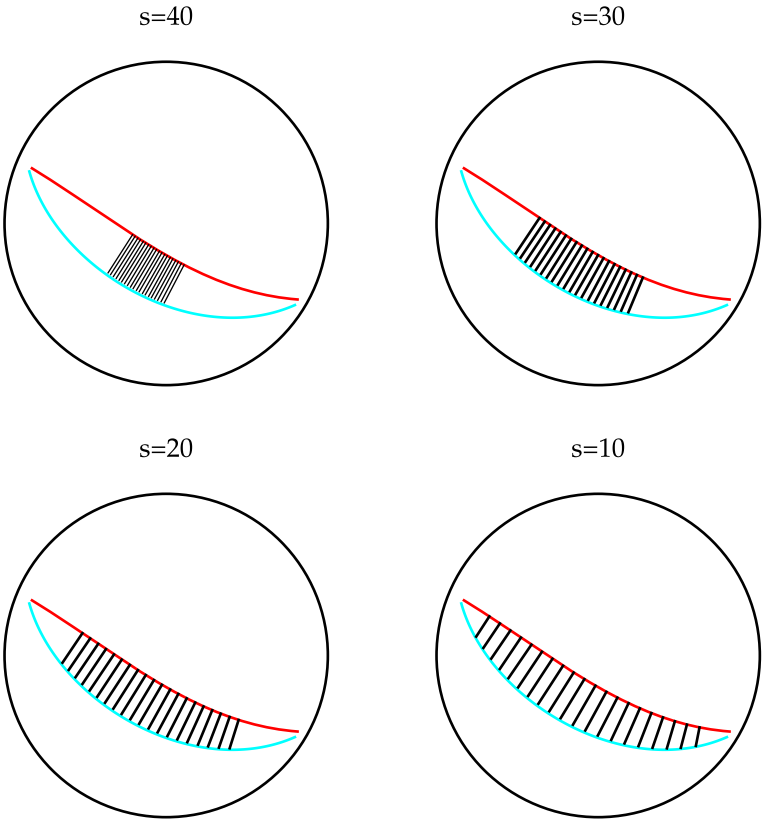

Figure 7.1: The equilibrium- and free-surface for the 35 rpm simulation with 20 slices through the middle 20%, 40%, 60% and 80% of the flowing layer ($s = 40$, $s = 30$, $s = 20$ and $s = 10$). The slices are perpendicular to the free-surface

Recall from Section 5.7 the outline of the method for the approximation of the two surfaces. The velocity along the slices are found using a linear interpolation of the volumetric elements. As they move away from the central region of the flowing layer the orientation of the slices becomes important. A slice from the middle of the flowing layer will be perpendicular to both the free surface and the equilibrium surface. As the slices move away from the middle they can no longer be perpendicular to both surfaces; for this reason two sets of slices are calculated. The first set, shown in Figure 7.2, is oriented perpendicular to the free surface. The second set, shown in Figure 7.3, is oriented perpendicular to the equilibrium surface.

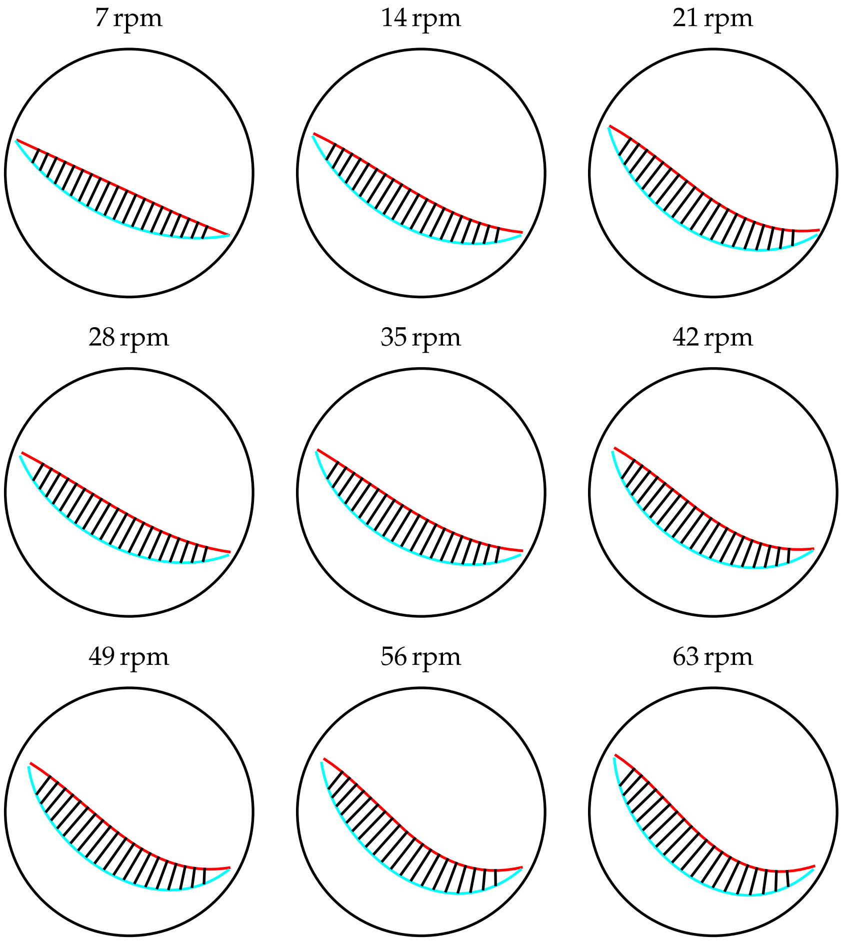

Figure 7.2: The equilibrium- and free-surfaces for all of the simulations with 20 slices through the middle 80% of the flowing layer ($s = 10$). The slices are perpendicular to the free-surfaces.

Both the flowing layer thickness and the flux are re-scaled. The rescaled flux is given by

$$Q^* = \frac{\langle v_t \rangle h}{d\sqrt{dg}}, \tag{7.1}$$

where v_t is the component of the velocity perpendicular to the slice. The flowing layer thickness h is scaled by the diameter of the particles, i.e. $\frac{h}{d}$. In addition to the flux based on the tangential velocity, the scaled average total velocity is also calculated through the slices, this is given by

$$Q^*_{\text{tot}} = \frac{\langle v \rangle h}{d\sqrt{dg}}. \tag{7.2}$$

Since the total velocity is taken, whether the slices are oriented relative to the equilibrium- or free surfaces should not make a significant difference to the average velocity.

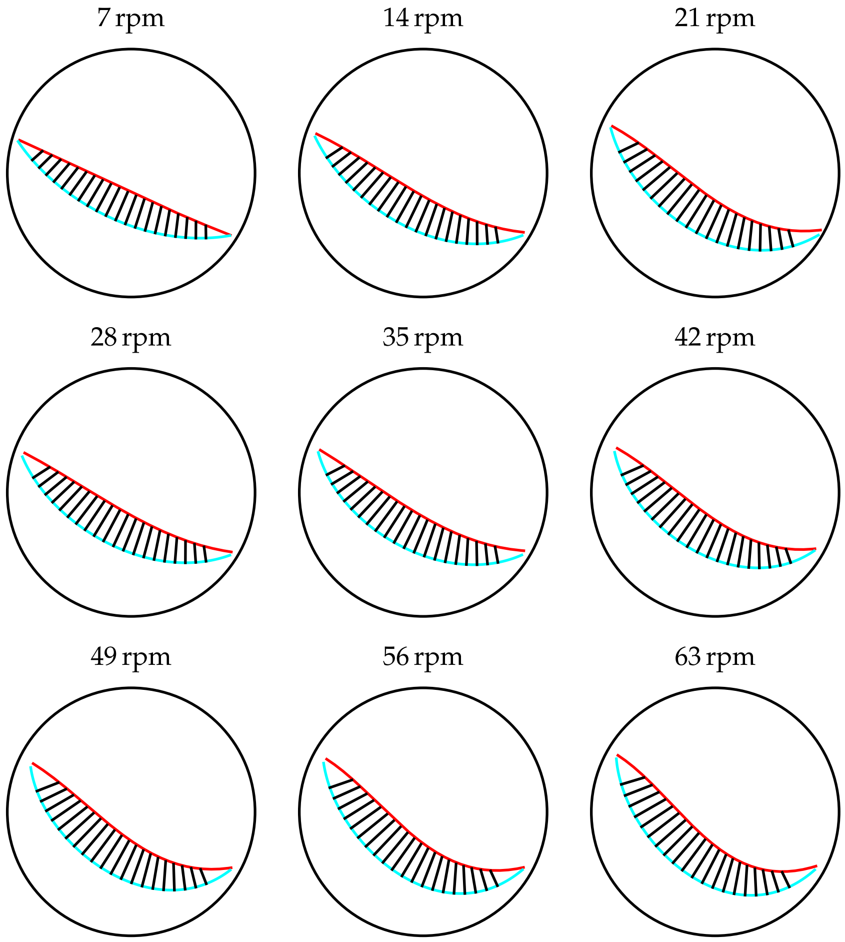

7 rpm 14 rpm 21 rpm

28 rpm 35 rpm 42 rpm

49 rpm 56 rpm 63 rpm

Figure 7.3: The equilibrium- and free-surfaces for all of the simulations with 20 slices through the middle 80% of the flowing layer ($s = 10$). The slices are perpendicular to the equilibrium-surfaces.

The scaling relation is determined by fitting a power law to the data, i.e.

$$\sqrt{Q^*} = a\left(\frac{h}{d}\right)^m \text{ and } \sqrt{Q^*_{\text{tot}}} = a\left(\frac{h}{d}\right)^m. \tag{7.3}$$

The parameters a and m are found from a least-squares fit of the data. The scaling between $\langle v_t \rangle$ or $\langle v \rangle$ and h can be found by rearranging Equation 7.3, i. e.

$$\langle v_t \rangle \propto h^{2m-1}. \tag{7.4}$$

A power law is used as many of the scaling relations from the literature can be expressed as a power law; this allows for easy comparison. Recall Table 2.1, previous work on this scaling law has produced a wide variety of results. Both GDR MiDi (2004) and Govender et al. (2016) found a linear scaling, i.e. $\langle v_t \rangle \propto h^1$; this corresponds to $m = 1$.

Figure 7.4 shows, for $s = 10, 20, 30, 40$, the relationship between $\sqrt{Q^*}$ and h/d along slices through the flowing layer that are oriented perpendicular to the free surface along with power-law and linear fits. The power-law fits correspond to Equation 7.3. The linear fits are also from Equation 7.3, but with $m = 1$, these are shown for reference. Figure 7.5 shows the relationship along equilibrium-surface-oriented slices through the flowing layer. Figures 7.7 and 7.6 show the relationship between the scaled average total velocity $\sqrt{Q^*_{\text{tot}}}$ and h/d along slices perpendicular to, respectively, the equilibrium surface and the free surface. For all four figures the power-law fits for both $s = 10$ and $s = 20$ are approximately linear. The power-law fit deviates from linear for $s = 30$ and deviates even more for $s = 40$. The results of the power-law fits for all of the scenarios are shown in Table 7.1. For each value of s there is not a significant difference between the fitted values for m for the equilibrium- and free-surface-oriented slices using both the scaled average total velocity $\sqrt{Q^*_{\text{tot}}}$ and the rescaled flux $\sqrt{Q^*}$.

For all of the scenarios, equilibrium- or free-surface-oriented and tangential or total velocity, the value of the exponent m increases as the section of the flowing layer that is being examined gets more narrow (i. e. s increases). Increasing m suggests that the scaling is not constant throughout the flowing layer. Félix et al. (2007) also found a non-constant m that was dependent on the drum diameter D scaled by the particle diameter d. They found that the scaling ranges from $\langle v_t \rangle \propto h^5$ for low values of D/d to $\langle v_t \rangle \propto h^{0.5}$ for high values of D/d.

In addition to the non-constant scaling throughout the flowing layer, there also appears to be a dependence of the scaling on the rotational speed of the drum. Figure 7.8 shows the exponent of the power-law fit for the results of each simulation. For $s = 10$, $s = 20$ and $s = 30$ the value of m appears to increase as the speed increases. There is a drop at 28 rpm, which corresponds to the slipping event observed in Chapter 3. For $s = 40$, there is no obvious increase in the value of m; this may be because the measurements are taken over such a narrow section of the flowing layer that the power law is being over-fitted.

The non-constant scaling indicates that there is no simple scaling for the flowing layer thickness in a rotating drum. It it likely that the scaling has a spatial dependence and a dependence on the drum's rotational speed. This can be further investigated by running a more diverse range of simulations than those done in this thesis. For instance, varying particle size distribution, particle shape and the dimensions of the drum would be necessary to determine a general scaling.

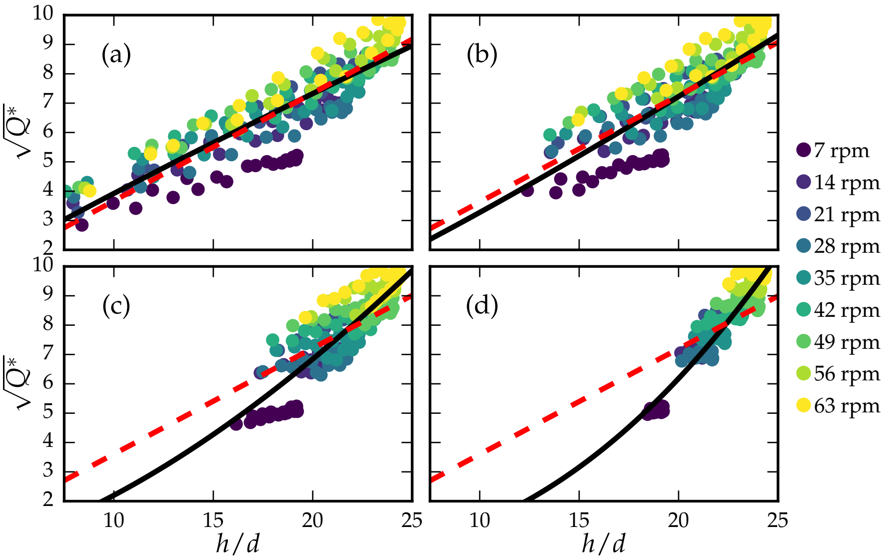

Figure 7.4: The scaled flow rate $\sqrt{Q^*}$ versus scaled flowing layer thickness h/d for (a) $s = 10$, (b) $s = 20$, (c) $s = 30$ and (d) $s = 40$. The tangential velocity is calculated from a coordinate system perpendicular to the free surfaces in the test space. Power-law and linear fits are shown, respectively, as black and red-dashed lines.

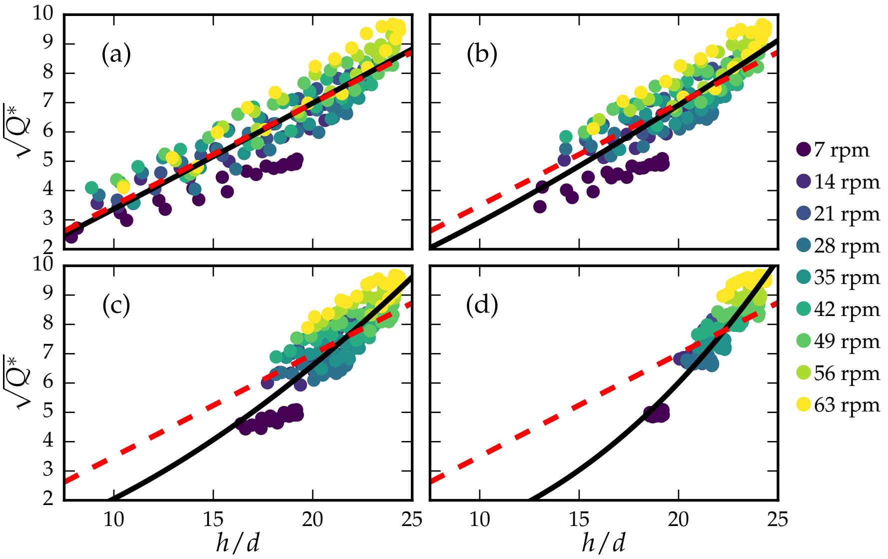

Figure 7.5: The scaled flow rate $\sqrt{Q^*}$ versus scaled flowing layer thickness h/d. The tangential velocity is calculated from a coordinate system perpendicular to the equilibrium surfaces in the test space. Power-law and linear fits are shown, respectively, as black and red-dashed lines.

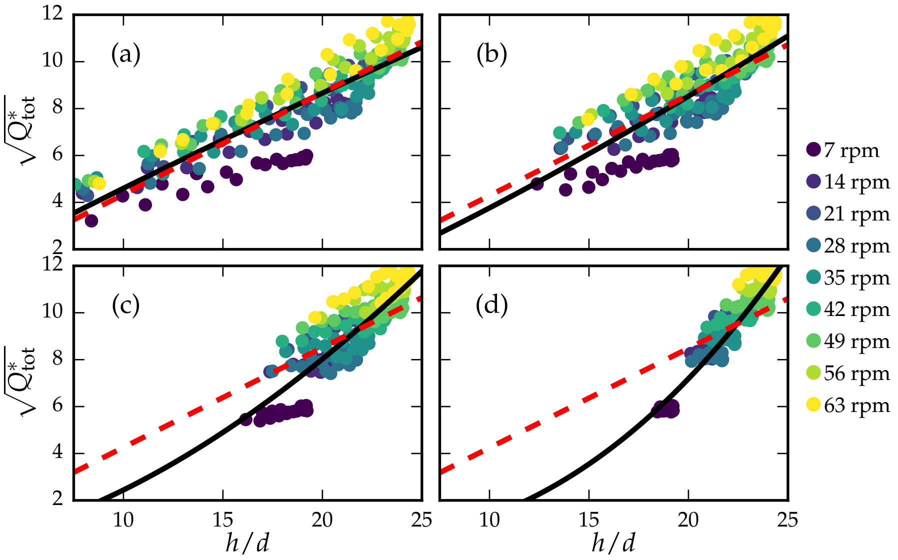

Figure 7.6: The scaled flow rate $\sqrt{Q^*_{\mathrm{tot}}}$ versus scaled flowing layer thickness h/d. The slices are from a coordinate system perpendicular to the free surfaces in the test space. Power-law and linear fits are shown, respectively, as black and red-dashed lines.

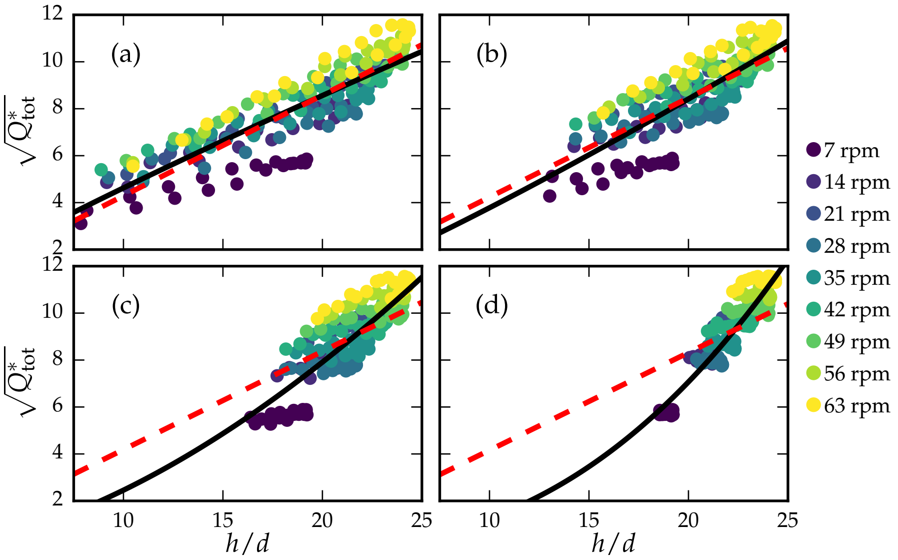

Figure 7.7: The scaled flow rate $\sqrt{Q^*_{\mathrm{tot}}}$ versus scaled flowing layer thickness h/d. The slices are from a coordinate system perpendicular to the equilibrium surfaces in the test space. Power-law and linear fits are shown, respectively, as black and red-dashed lines.

Slices relative to surface	Velocity component	s	m	RMSE
free	total	10	0.91 ± 0.08	0.937
equilibrium	total	10	0.89 ± 0.09	0.955
free	tangent	10	0.90 ± 0.08	0.757
equilibrium	tangent	10	1.05 ± 0.08	0.704
free	total	20	1.18 ± 0.13	0.973
equilibrium	total	20	1.15 ± 0.13	0.981
free	tangent	20	1.14 ± 0.12	0.795
equilibrium	tangent	20	1.24 ± 0.12	0.729
free	total	30	1.72 ± 0.17	0.880
equilibrium	total	30	1.69 ± 0.18	0.906
free	tangent	30	1.64 ± 0.16	0.717
equilibrium	tangent	30	1.68 ± 0.16	0.677
free	total	40	2.45 ± 0.14	0.575
equilibrium	total	40	2.48 ± 0.17	0.640
free	tangent	40	2.33 ± 0.13	0.464
equilibrium	tangent	40	2.38 ± 0.15	0.478

Table 7.1: Parameters for power-law best-fit for various scenarios of slices through the flowing layer. The fitted parameter m is shown with a 95% confidence interval.

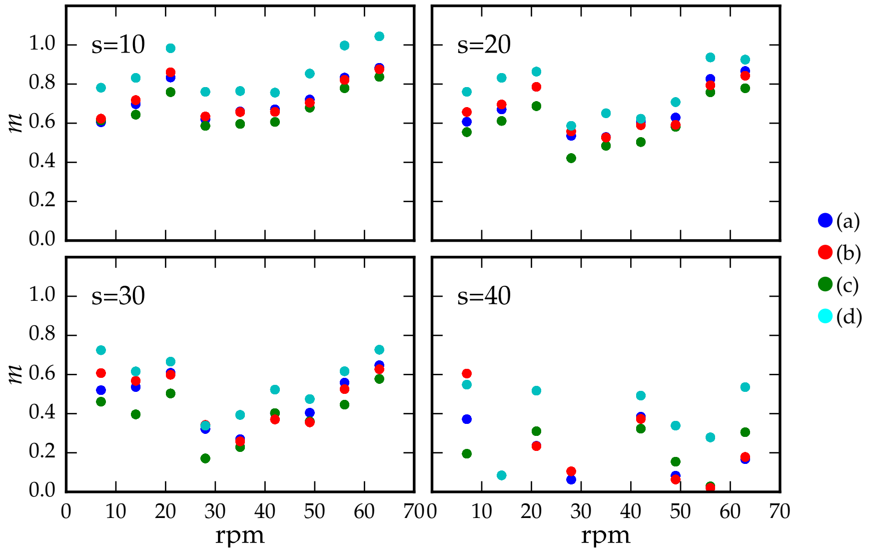

Figure 7.8: The value of the exponent of the power-law fit m done for each simulation for all of the scenarios versus the rotational speed of the drum (rpm). Each of the four graphs shows the results for different values of s, as labelled. The coloured points represent the measurements for the: (a) free-surface-oriented total velocity, (b) equilibrium-surface-oriented total velocity, (c) free-surface-oriented tangent velocity and (d) equilibrium-surface-oriented tangent velocity.

7.3 DYNAMIC ANGLE OF REPOSE

In slowly rotating drums the free surface is planar and the dynamic angle of repose is the angle the free surface makes with the horizontal. As the rotational speed increases the free surface becomes warped, taking on an "S"-like shape. The lack of a planar free surface at higher speeds requires a new definition for the dynamic angle of repose. Govender et al. (2016) proposed fitting an ellipse to the equilibrium surface. The angle that the semi-major axis of the ellipse makes with the horizontal is then taken to be the dynamic angle of repose. At low speeds the semi-major axis of the ellipse coincides with the free surface.This repose angle is representative of the system as a whole, but it may also be useful to compare the local repose angle from a number of positions on the free- or equilibrium surfaces. Both methods are investigated, the ellipse-based repose angle in Section 7.3.1 and the local repose angle in Section 7.3.2.

7.3.1 *Global repose angle*

The ellipse fitting is done using the routine described by Fitzgibbon (1998) and using the Python implementation by Foreest (2016). In Fitzgibbon's routine the ellipse fitting is represented as a constrained minimization problem. The quantity being minimized is the algebraic distance of the points to a conic section which is subject to an ellipticity constraint[1]. Figure 7.9 shows the ellipses that were fit to the equilibrium surface for each simulation.. The semi-major axis of the ellipse is parallel with the free surface for the 7 rpm simulation.

The rotating drum experiments and simulations by GDR MiDi (2004) cover a wide range of rotational speeds, particle sizes and drum dimensions. They performed experiments with steel and glass beads as well as sand, these were done for a number of drum widths and diameters. GDR MiDi compared the scaling between the rising flux and the dynamic angle of repose. The rising flux is given by

$$Q_u = \frac{\langle v_t \rangle h_u}{d\sqrt{dg}}, \tag{7.5}$$

where h_u is the thickness of the rising layer along the line passing through the centre of circulation. In rotating drum systems that have reached a dynamic equilibrium the rising and falling flux should be the same.

Figure 7.10 shows the relationship between the dynamic angle of repose φ and the rising flux Q_u for the simulations in the test space as well as the results from the experiments and simulations of GDR MiDi. GDR MiDi's results show that the general tendency is for the repose angle to increase with the flow rate. They also found that the sensitivity of the repose angle to the flow rate tends to decrease as the axial width of the drum increases, with very wide drums having an almost constant repose angle. They conjectured that in the case of infinitely long walls the effective friction is constant and independent of Q^*. They also suggest that any observed dependencies in the case of infinitely long walls would be due to "intricate wall and geometric effects".

The simulations here are done on a drum that is periodic along its axis. This is done out of computational necessity as well as to eliminate end-wall effects. The complete lack of end walls means the system should behave more like a drum of infinite width. According to GDR MiDi's conjecture the repose angle for the simulations in this thesis should be approximately constant and should be similar to the results of GDR MiDi with a very wide drum width, however this is not what the results show. The results of this thesis appear to behave more like the experiments of GDR MiDi with a very narrow drum. The dynamic angle of repose appears to have a strong dependence on the upward flux.

---

[1] A thorough overview of the ellipse fitting routine can be found in Chapter 3 of Fitzgibbon (1998).

7.3.2 *Local repose angle*

In flows of particles down a slope, the surface over which the particles are flowing is parallel to the free surface; this is also true for the repose angle in slowly rotating drums. In the middle of the flowing layer the equilibrium surface and free surface will be approximately parallel, so the repose angle will be the same regardless of the reference surface. As with the choice of a reference surface in Section 7.2, when measuring away from the middle of the flowing layer the repose angle will be different relative to the free surface versus the equilibrium surface. Figure 7.11 shows the repose angle relative to the free surface versus the scaled flow rate Q^*. The same slices through 80% of the flowing layer are used as in Section 7.2 (i. e. $s = 10$), see Figure 7.2. The results have an oblique parabolic shape, the turning point of which appears to increase as the rotational speed increases. Initially the free surface is flat (at 7 rpm), so the dynamic angle of repose is roughly equal for all of the slices. The range of angles for each simulation seems to increase as the rotational speed increases. Figure 7.12 shows the repose angle relative to the equilibrium surface versus the scaled flow rate Q^*. Because the equilibrium surface is not flat for low rotational speeds, there is a wider range of angles at low speeds when compared to the results relative to the free surface. The range of angles also increases as the speed increases.

When pursuing a scaling law involving the dynamic angle of repose, the repose angle relative to the free surface would be preferable as it is essentially constant at low rotational speeds. The equilibrium surface is, however, the surface over which the particles are flowing, so it has a more significant influence over the flow of the particles.

7.3.3 *Summary*

The results of the global dynamic angle of repose scaling are in disagreement with the results of GDR MiDi (2004); it is not clear why. Further work should include simulations with aperiodic boundary conditions and multiple drum lengths, in order to determine if drum length has any influence on the scaling. The local repose angle scaling has no obvious trend. In further work the non-dimensional quantities should be investigated in more detail, as it is possible that a scaling law may include a higher order term, such as acceleration.

7.4 CONCLUSION

In this chapter the scaling laws governing dense granular flows were investigated in the test space.

The relationship between the thickness of the downward-flowing layer and the scaled flow rate was investigated. The scaled tangential and total flow rates were calculated through 20 equally spaced slices through a middle-section of the flowing layer that varied in size from 20% to 80% of the layer. The orientation of the slices was also investigated. One set of slices was oriented perpendicular to the free-surface, while another was oriented perpendicular to the equilibrium surface. There was no significant difference between the power-law fits for the various scenarios (tangential or total velocity and free- or equilibrium-surface). The scaling was found to be dependent on the length of the section of the flowing layer. The middle 20% of the flowing layer was found to have a higher exponent in the power-law fit. When the middle 80% of the flowing layer was measured the scaled flow rate varied linearly with the thickness. A dependence on the rotational speed of the drum was also observed.

The relationship between the dynamic angle of repose φ and the flux was examined using two different definitions of θ. The first was based on best-fit of an ellipse to the equilibrium surface. φ was found to be highly dependent on Q_u. This result is contrary to the results of GDR MiDi (2004), who found that the dependence on Q_u gets weaker as the axial length of the drum increases. The reason for this discrepancy is not clear; it can be investigated further by running simulations with a wider range of boundary conditions and particle size distributions. The second θ was defined to be the tangent to either the free- and equilibrium surfaces. θ was measured relative to both surfaces at a number of slices through the flowing layer. A complex relationship between the flux and the repose angle was observed relative to both surfaces.

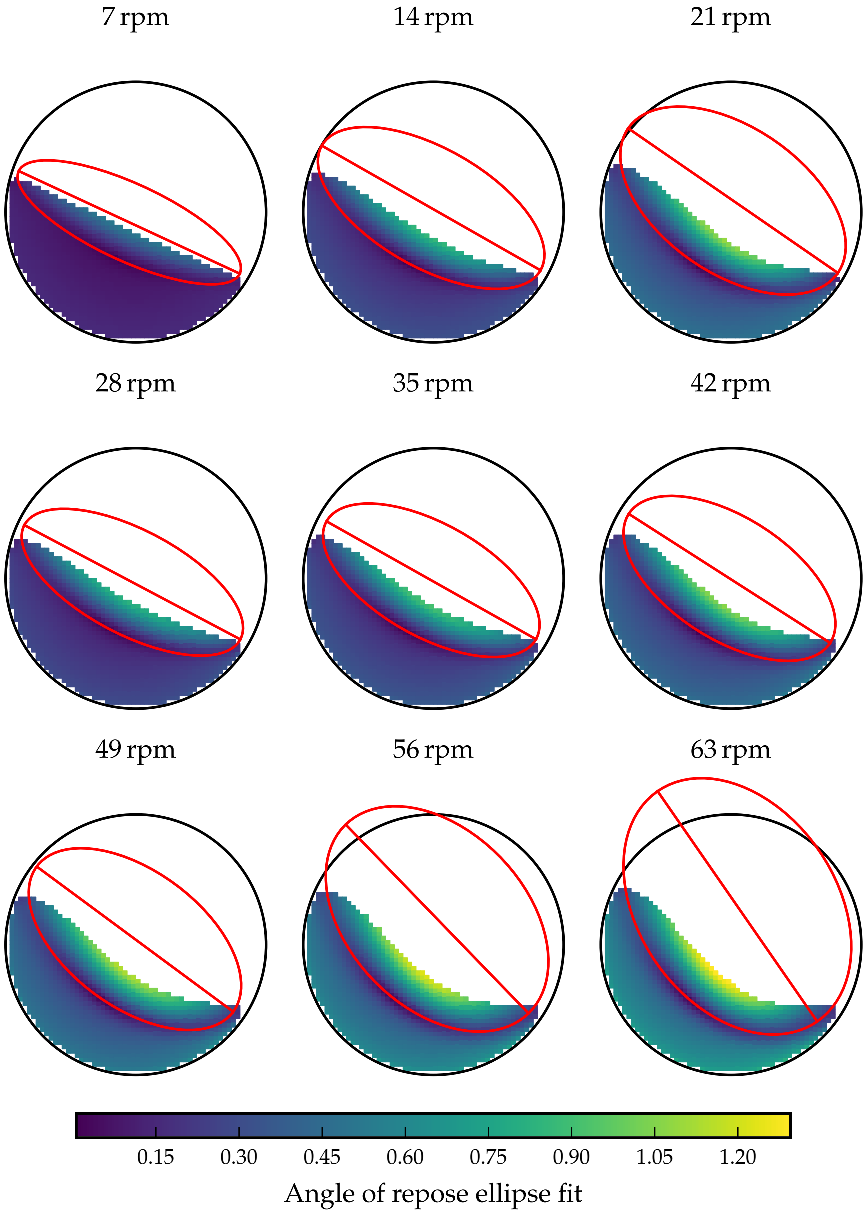

Figure 7.9: Ellipses that are fitted to the equilibrium surface for each simulation are shown in red. The semi-major axes for all of the ellipses are also shown. The volumetric elements are coloured by the velocity magnitude

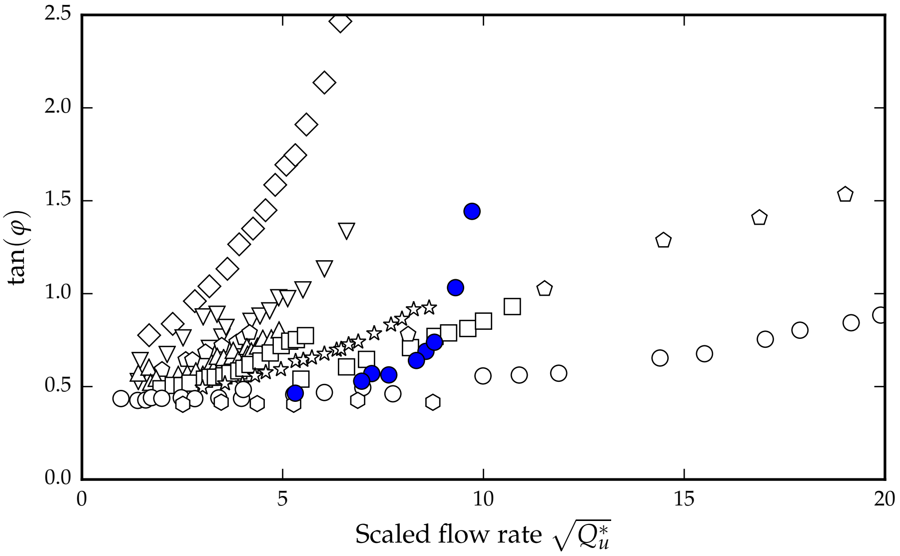

Figure 7.10: The dimensionless flow rate versus $\tan(\varphi)$, which is the friction coefficient for the dynamic angle of repose. The results shown in black are taken from Figure 6n of GDR MiDi (2004) and the blue circles are from the 9 simulations in this thesis. Each symbol represents a different experimental system. The systems with a wider drum tend to have a weaker dependence on the flux.

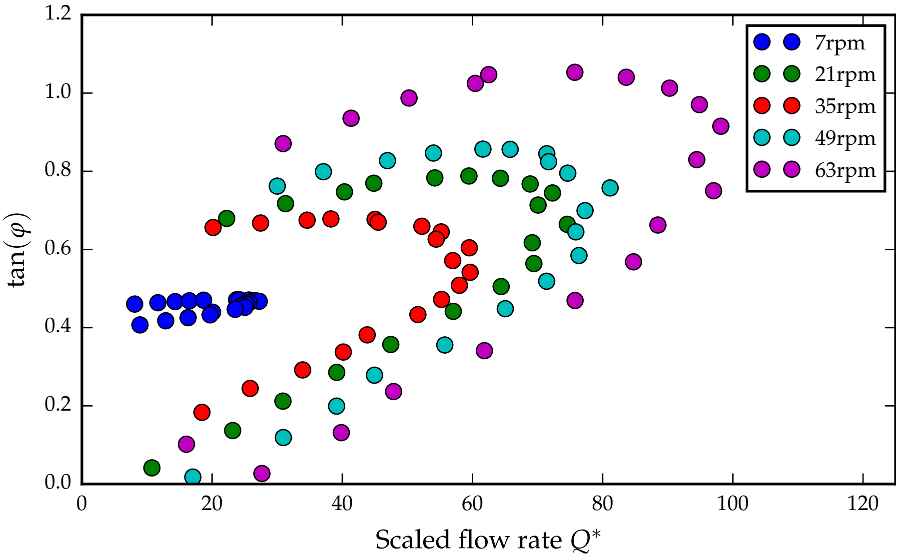

Figure 7.11: The tangent of the repose angle $\tan(\varphi)$ as measured from slices through the flowing layer perpendicular to the free surface.

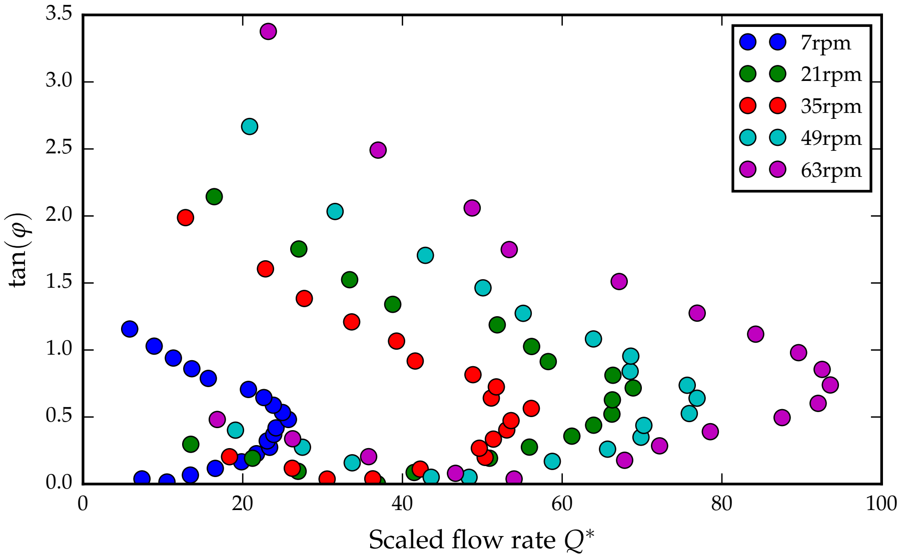

Figure 7.12: The tangent of the repose angle $\tan(\varphi)$ as measured from slices through the flowing layer perpendicular to the equilibrium surface.

8

CONCLUSION

Discrete element method-based simulations of spherical particles in a rotating drum were used to investigate scaling laws and constitutive relations for dense granular flow. Nine different simulations were run with the rotational speed varying from 7 to 63 revolutions per minute. Spatio-temporal averaging techniques were used to extract kinematic and kinetic quantities from the resulting data.

The key assumptions of isotropy and incompressibility for the three-dimensional constitutive law proposed by Jop et al. (2006) were investigated using the kinematic and kinetic measures obtained from the simulations. All of the systems were found to be largely incompressible. A small degree of compressibility was observed in the downward-flowing layer of the drum. The isotropy assumption was found to be valid in the downward-flowing layer of all of the simulations. The rising layer was found to have a high degree of anisotropy in the slowly-rotating simulations, the degree of which decreased as the rotational speed increased. The rapidly-rotating simulations were mostly isotropic. These results suggest that it may be possible to simulate the flow of granular material in rapidly rotating drums as a fluid using Jop et al.'s constitutive equation and a numerical scheme such as finite differences or finite elements. Such simulations would be worth exploring in further work. Industrial mills often contain slurries, i. e. granular suspensions. The two assumptions should also be investigated for granular suspensions with simulations done using DEM in a two-way coupling with either finite-element or finite-difference methods.

The friction coefficient $\mu(I)$ for the constitutive law was also investigated. The phenomenological laws of da Cruz et al. (2005) and Jop et al. (2005) were compared with a law proposed here. The newly proposed law was found to fit the data better, with the sigmoidal law of Jop et al. being the next-best. The new law should be tested over a wider range of simulations in further work. None of the proposed laws were able to capture the friction coefficient for low inertial numbers ($I < 10^{-2}$). This is most likely due to local effects, such as shear-banding, that were observed in regions with high anisotropy. A complete constitutive law for granular material would have to take these local effects into account. In addition, a complete law would have to be able to account for phase-changes and hysteresis. Local constitutive laws such as those by Kamrin et al. (2012) and Chen et al. (2009) are show promise in this regard, and should be investigated further.

The scaling law that relates the thickness of a layer of flowing particles with the scaled flow rate through the layer was investigated. Scaled flow rates based on the tangential and total velocity were calculated passing through a number of equally-spaced slices through the flowing-layer. The size of the middle section of the flowing layer that was measured was varied from 20% to 80%. The orientation of the slices was also varied, with one set of slices oriented perpendicular to the free surface and the other perpendicular to the equilibrium surface. A least-squares fit of a power law was performed on each set of data. The orientation of the slices and the type of velocity used in the flow rate was not found to make a significant difference to the power law. The size of the section through the flowing layer was found to make a significant difference, with large sections having an approximately linear relationship between the scaled flow rate and the scaled thickness. This indicates that the scaling of the flow rate is not constant through the flowing layer. In addition, the scaling appeared to change with the drum speed. As further work, a more comprehensive set of simulations should be performed. In this work features such as drum dimension and particle size distribution and shape were kept constant, further work to investigate this scaling relation should vary these quantities to obtain a more comprehensive data set.

The scaling law that relates the flux through the flowing layer and the dynamic angle of repose was investigated using two different measures of the repose angle. In the first measure the repose angle was taken to be related to an ellipse that is fit to the equilibrium surface. Here strong dependence on the flux was observed, which is contrary to the results of da Cruz et al. (2005), who found that the dependence should decrease as the width of the drum increases. The simulations that were performed were periodic in the axial direction, so they should behave in a similar manner to an infinitely long drum. Similar to the flowing layer thickness scaling, further work here should include a more comprehensive set of simulations. In particular, using aperiodic boundary conditions and varying the axial length of the drum would enable a better comparison with the results of da Cruz et al.

The second measure of the dynamic angle of repose was taken to be the angle the tangent to either the free or equilibrium surfaces makes with the horizontal. The repose angle using this definition is a dynamic quantity that changes according to the location of the point on the respective surface. The flux and repose angle plots showed complex behaviour. It is proposed that in further work the acceleration be introduced into the scaling, to account for the deceleration of the particles near the toe region and the acceleration near the head.

A slipping event was observed in the 28 rpm simulation; this is conjectured to be due to a frictional threshold being reached between the particles and the drum. This conjecture is supported by the sudden decrease in tangential force between the particles and the drum that was observed in a simulation in which the rotational speed was slowly increased from 21 rpm to 28 rpm. In addition the pressure and the shear stress were observed to decrease next to the edge of the drum for the 28 rpm simulations and upwards. The identically-size spherical particles used in this work may be the cause of this phenomenon. In further work, simulations with varying particle size and density should be used to see if this conjecture is correct.

A

APPENDIX: PLOTS THROUGH THE CENTRE OF CIRCULATION

In this appendix plots of various quantities interpolated along a line through the centre of circulation in each of the nine simulations in the test space.

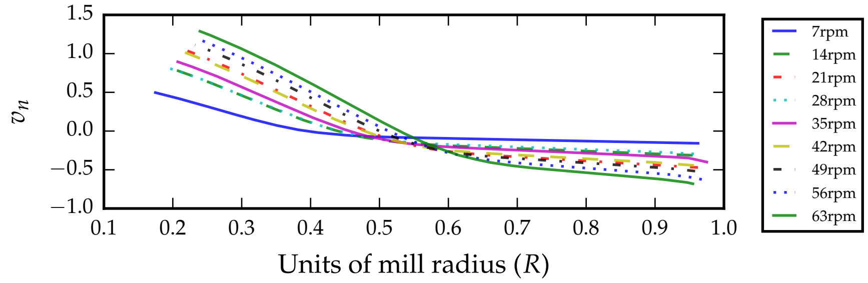

Figure A.1: The velocity tangent to the normal of the line through the centre of circulation in the test space.

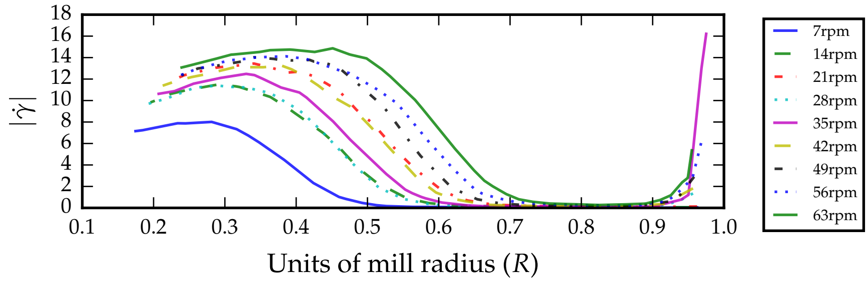

Figure A.2: The shear rate $|\gamma|$ on the line through the centre of circulation in the test space.

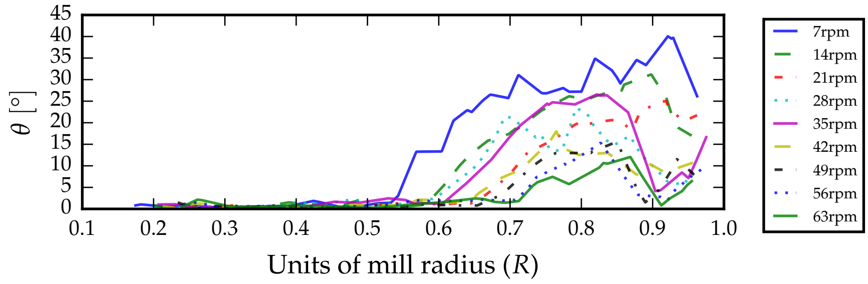

Figure A.3: The measure of coaxiality θ on the line through the centre of circulation in the test space.

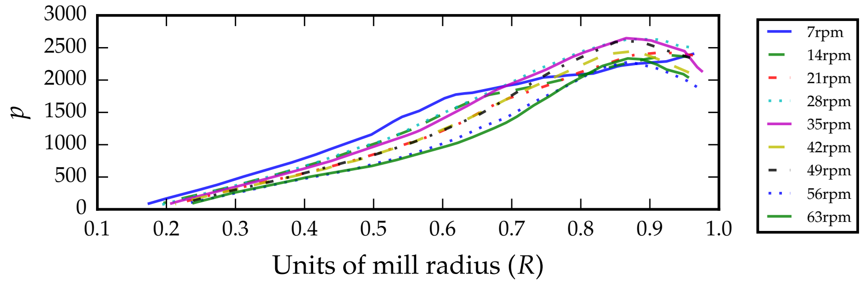

Figure A.4: The pressure p on the line through the centre of circulation in the test space.

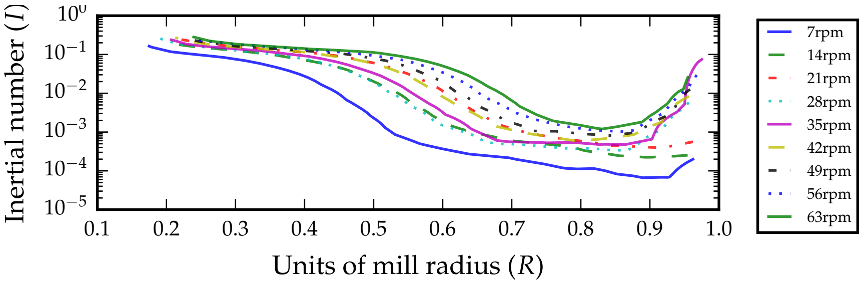

Figure A.5: The inertial number I on the line through the centre of circulation in the test space.

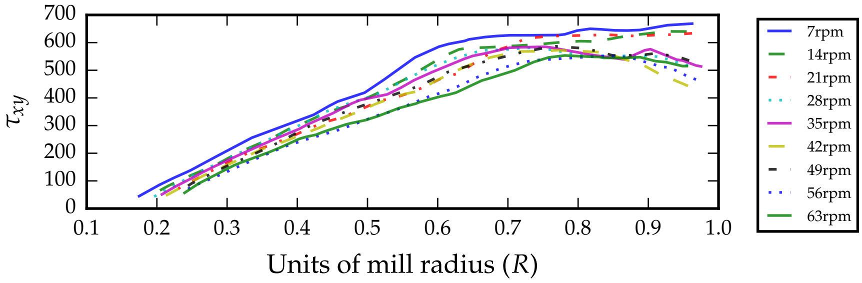

Figure A.6: The shear stress τ_{xy} relative to the line through the centre of circulation in the test space.

B

APPENDIX: COAXIALITY PLOTS USING THE DEVIATORIC OF THE SYMMETRIC VELOCITY GRADIENT

In this appendix the plots from Sections 6.3 and 6.4 are replicated using the $\boldsymbol{D}_{\text{dev}}$, the deviatoric component of the symmetric velocity gradient, instead of $\boldsymbol{D}$. There is no significant difference in the results shown here.

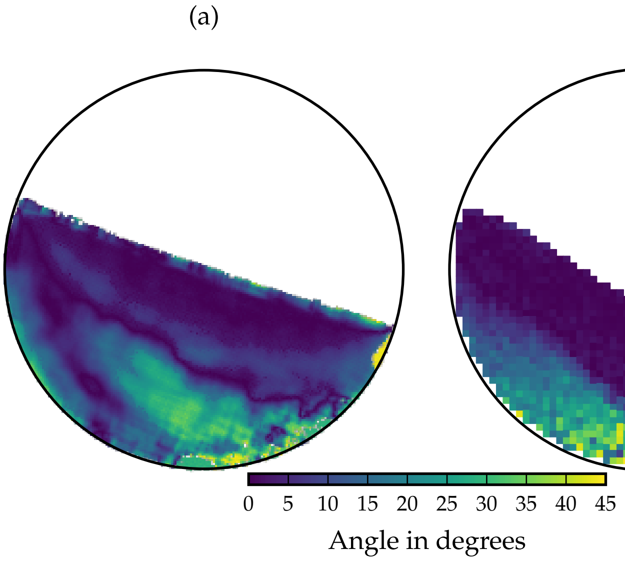

Figure B.2: The measure of coaxiality from (a) the 12 rpm simulation of Cortet et al. (2009) (b) the 14 rpm simulation in this work. In order to get a better qualitative comparison, the data for (a) was extracted digitally from Figure 6a of Cortet et al. (2009) and converted to the same colour map as (b).

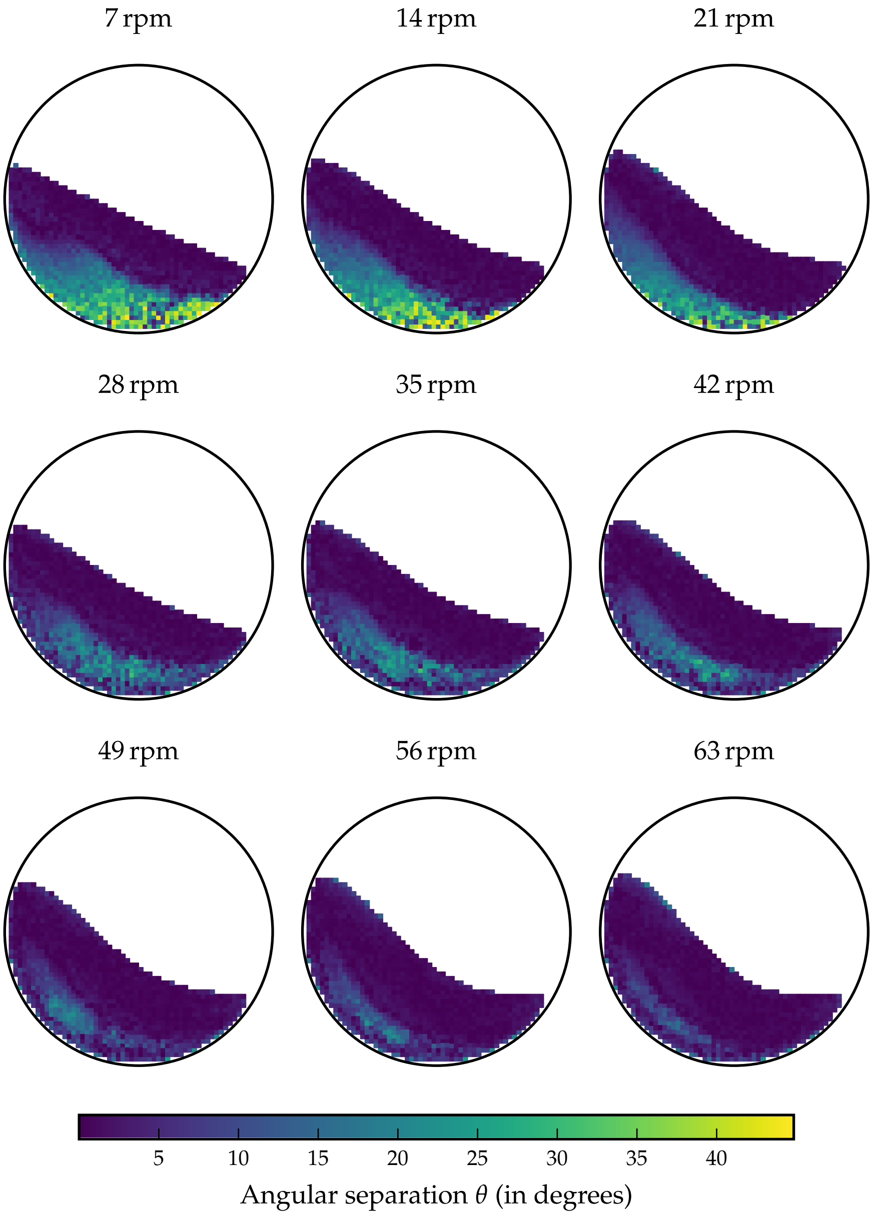

Figure B.1: The measure of coaxiality θ over the test space.

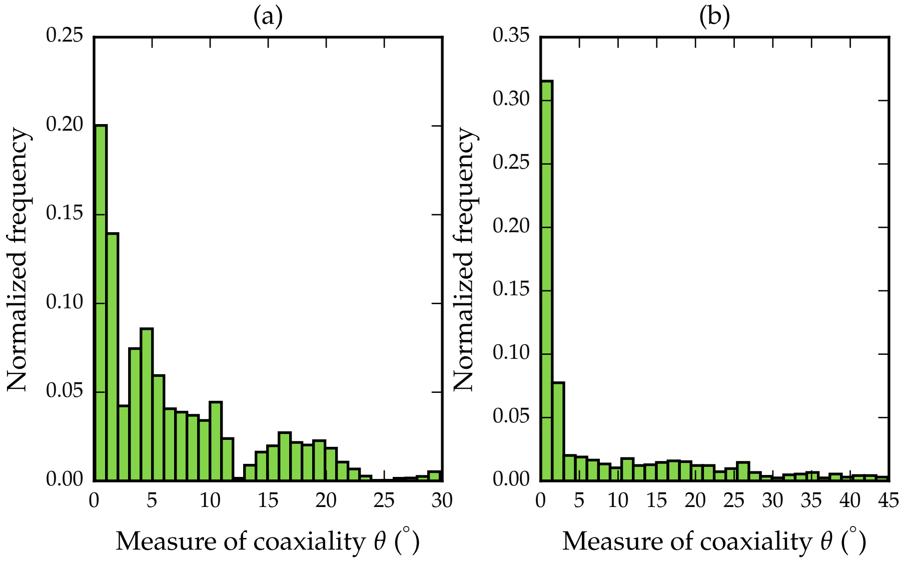

Figure B.3: Histograms showing the normalized frequency of the measure of coaxiality θ for (a) the 12 rpm simulation of Cortet et al. (2009) and (b) the 14 rpm simulation in this work. The data for (a) was digitally extracted from Figure 6a of Cortet et al. (2009).

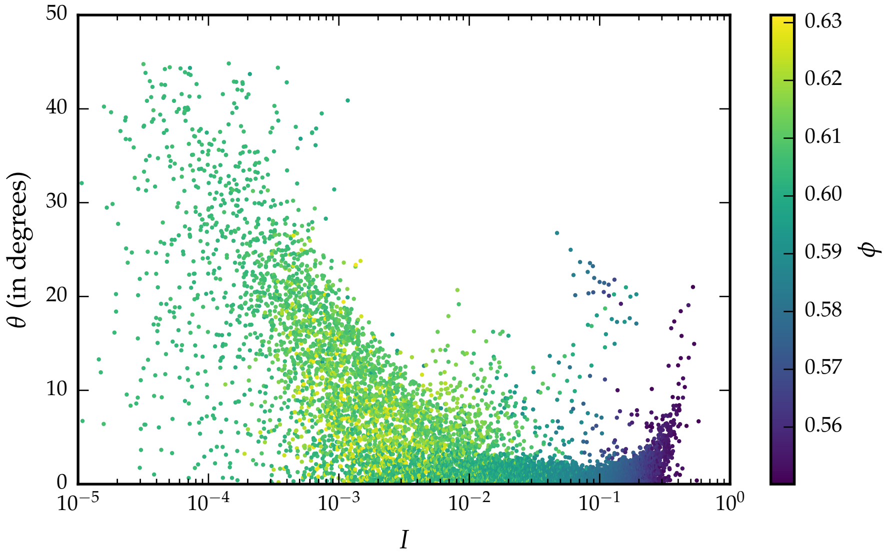

Figure B.4: The measure of coaxiality θ vs the inertial number I over the test space. The points are coloured by the packing fraction ϕ.

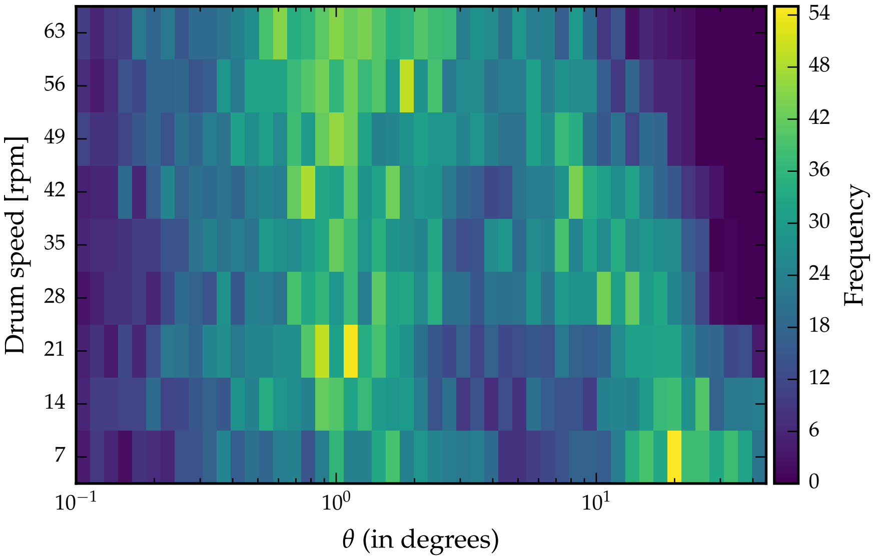

Figure B.5: A set of histograms of the measure of coaxiality θ. Each row of cells is a histogram for one of the simulations. From the bottom row upwards the rows are arranged in ascending order of rotational speed. The rotational speed is shown on the vertical axis. Each row/histogram is divided into 50 bins. The bins are equally spaced in log space. The frequency of volumetric elements in each bin is represented by the colour.

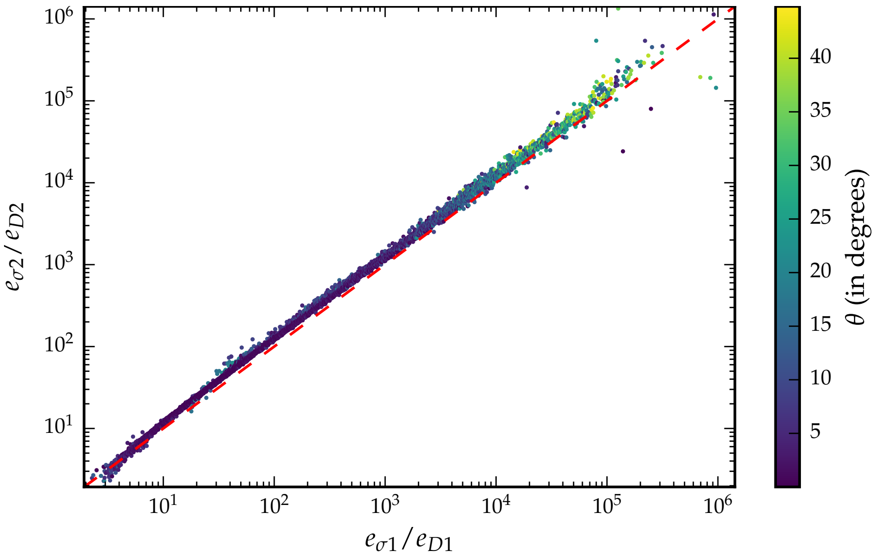

Figure B.6: The scaling between the maximal principle directions of $\boldsymbol{\tau}$ and $\boldsymbol{D}$ for the volumetric elements in all of the simulations vs that of the minimal principle directions. The points are coloured by the measure of coaxiality θ. For reference the line $\frac{\xi_1}{\delta_1} = \frac{\xi_2}{\delta_2}$ is included.

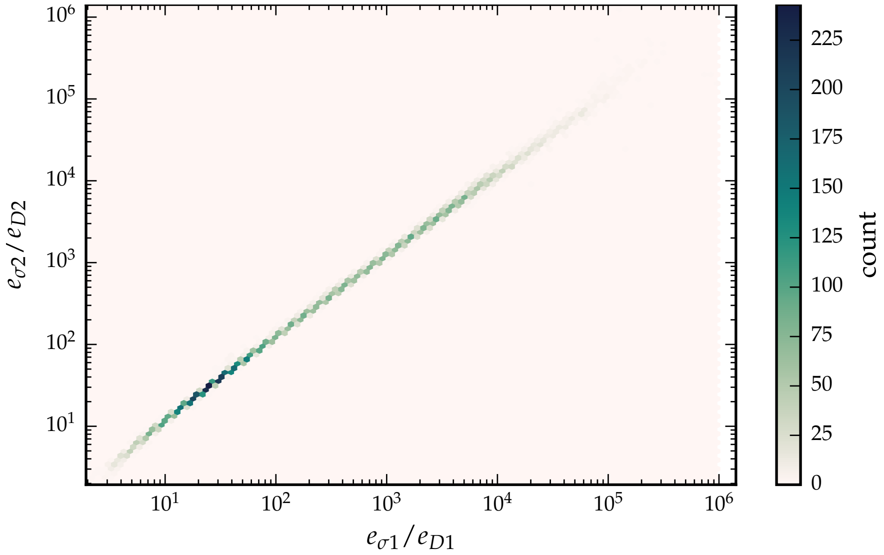

Figure B.7: A hexagonal histogram showing the frequency of the scaling between the maximal principle directions of $\boldsymbol{\tau}$ and $\boldsymbol{D}$ for the volumetric elements in all of the simulations vs that of the minimal principle directions.

BIBLIOGRAPHY

Ancey, C. (2002). Dry granular flows down an inclined channel: Experimental investigations on the frictional-collisional regime. *Physical Review E* 65.1.

Ancey, C., P. Coussot and P. Evesque (1999). A theoretical framework for granular suspensions in a steady simple shear flow. *Journal of Rheology* 43 (6).

Andreotti, B., Y. Forterre and O. Pouliquen (2013). *Granular Media: Between Fluid and Solid*. Cambridge University Press.

Aris, R. (1990). *Vectors, Tensors and the Basic Equations of Fluid Mechanics*. Dover Books on Mathematics. Dover Publications.

Astarita, G. and G. Marrucci (1974). *Principles of Non-Newtonian Fluid Mechanics*. McGraw-Hill.

Bagnold, R. A. (1954a). Experiments on a Gravity-Free Dispersion of Large Solid Spheres in a Newtonian Fluid under Shear. *Proceedings of the Royal Society of London. Series A, Mathematical and Physical Sciences* 225.1160, pp. 49–63.

Bagnold, RA (1954b). *The Physics of Blown Sand and Desert Dunes.* Dover edition.

Barker, T., D.G. Schaeffer, P. Bohorquez and J.M.N.T Gray (2015). Well-posed and ill-posed behaviour of the -rheology for granular flow. *Journal of Fluid Mechanics* 779, pp. 794–818.

Bertrand, J (1878). Sur l'homogénéité dans les formules de physique. *Comptes rendus* 86.15, pp. 916–920.

Bird, R.B., G.C. Dai and B.J. Yarusso (1983). The rheology and flow of viscoplastic materials. *Reviews in Chemical Engineering* 1.1, pp. 1–70.

Bonet, J. and J. Peraire (1991). An alternating digital tree (ADT) algorithm for 3D geometric searching and intersection problems. *International Journal for Numerical Methods in Engineering* 31.1, pp. 1–17.

Boyer, F., É. Guazzelli and O. Pouliquen (Oct. 2011). Unifying Suspension and Granular Rheology. *Physical Review Letters* 107.18, p. 188301.

Buckingham, E. (1914). On Physically Similar Systems; Illustrations of the Use of Dimensional Equations. *Physical Review* 4 (4), pp. 345–376.

Chareyre, B. and P. Villard (2005). Dynamic spar elements and discrete element methods in two dimensions for the modeling of soil-inclusion problems. *Journal of Engineering Mechanics* 131.7, pp. 689–698.

Chen, K.-C. and J.-Y. Lan (2009). Micromorphic modeling of granular dynamics. *International Journal of Solids and Structures* 46.6, pp. 1554 –1563.

Cleary, P.W., M.D. Sinnott and G.C. Pereira (2015a). Computational prediction of performance for a full scale Isamill: Part 1 – Media motion and energy utilisation in a dry mill. *Minerals Engineering* 79, pp. 220 –238.

Cleary, P.W. and M.D. Sinnott (2015b). Computational prediction of performance for a full scale Isamill: Part 2 – Wet models of charge and slurry transport. *Minerals Engineering* 79, pp. 239 –260.

Cortet, P.-P., D. Bonamy, F. Daviaud, O. Dauchot, B. Dubrulle and M. Renouf (2009). Relevance of visco-plastic theory in a multi-directional inhomogeneous granular flow. *Europhysics Letters* 88.1, p. 14001.

Cundall, P.A. (1971). A computer model for simulating progressive, large-scale movements in blocky rock systems. *Proceedings of the International Society for Rock Mechanics*. Vol. 2. 8.

Cundall, P.A. and O.D.L. Strack (1979). A discrete numerical model for granular assemblies. *Geotechnique* 29.1, pp. 47–65.

Daerr, A. and S. Douady (1999). Sensitivity of granular surface flows to preparation. *Europhysics Letters* 47.3, p. 324.

Ding, J. and D. Gidaspow (1990). A bubbling fluidization model using kinetic theory of granular flow. *American Institute of Chemical Engineers Journal* 36.4, pp. 523–538.

Dury, C., G. Ristow, J. Moss and M. Nakagawa (1998). Boundary effects on the angle of repose in rotating cylinders. *Physical Review E* 57.4, pp. 4491–4497.

Félix, G., V. Falk and U. D'Ortona (2007). Granular flows in a rotating drum: The scaling law between velocity and thickness of the flow. *European Physical Journal E* 22.1, pp. 25–31.

Fitzgibbon, A.W.J. (1998). Stable segmentation of 2D curves. PhD thesis.

Foreest, N. van (2016). *Fitting an Ellipse to a Set of Data Points*. URL: `http://nicky.vanforeest.com/misc/fitEllipse/fitEllipse.html`.

Forterre, Y. and O. Pouliquen (2008). Flows of dense granular media. *Annu. Rev. Fluid Mech.* 40, pp. 1–24.

GDR MiDi (2004). On dense granular flows. *European Physical Journal E* 14.4, pp. 341–365.

Gladky, A. et al. (Oct. 2014). *Yade 1.12.0*.

Goldhirsch, I. (Jan. 2003). Rapid granular flows. *Annual Review of Fluid Mechanics* 35.1, pp. 267–293.

Govender, I. (2005). X-Ray Motion Analysis of Charge Particles in A Laboratory Mill. PhD thesis. University of Cape Town.

Govender, I., A.T. McBride and M.S. Powell (2004). Improved experimental tracking techniques for validating discrete element method simulations of tumbling mills. *Experimental Mechanics* 44.6, pp. 593–607.

Govender, I., M. C. Richter, D. N. De Klerk and A. N. Mainza (2016). A Positron Emission Particle Tracking investigation of the scaling law governing free surface flows in tumbling mills.

Hatano, T. (2007). Power-law friction in closely packed granular materials. *Physical Review E* 75 (6).

Henein, H., J. K. Brimacombe and a. P. Watkinson (1983). Experimental study of transverse bed motion in rotary kilns. *Metallurgical Transactions B* 14.2, pp. 191–205.

Hogg, R (1999). Breakage mechanisms and mill performance in ultrafine grinding. *Powder Technology* 105.1, pp. 135–140.

Hromnik, M. (2013). A GPGPU implementation of the discrete element method applied to modeling the dynamic particulate environment inside a tumbling mill. PhD thesis. University of Cape Town.

Hunter, J. D. (2007). Matplotlib: A 2D graphics environment. *Computing In Science & Engineering* 9.3, pp. 90–95.

Jain, N., J. M. Ottino and R. M. Lueptow (2002). An experimental study of the flowing granular layer in a rotating tumbler. *Physics of Fluids* 14.2, pp. 572–582.

Jenkins, J.T. and C. Zhang (2002). Kinetic theory for identical, frictional, nearly elastic spheres. *Physics of Fluids* 14 (3).

Jop, P. (2015). Rheological properties of dense granular flows. *Comptes Rendus Physique* 16.1, pp. 62 –72.

Jop, P., Y. Forterre and O. Pouliquen (2005). Crucial role of sidewalls in granular surface flows: consequences for the rheology. *Journal of Fluid Mechanics* 541, pp. 167–192.

Jop, P., Y. Forterre and O. Pouliquen (2006). A constitutive law for dense granular flows. *Nature* 441.7094, pp. 727–730.

Kamrin, K. and G. Koval (Apr. 2012). Nonlocal Constitutive Relation for Steady Granular Flow. *Physical Review Letters* 108.17, p. 178301.

Lagrée, P.-Y., L. Staron and S. Popinet (2011). The granular column collapse as a continuum: validity of a two-dimensional Navier-Stokes model with a $\mu(I)$-rheology. *Journal of Fluid Mechanics* 686, pp. 378–408.

Landry, J.W., G.S. Grest, L.E. Silbert and S.J. Plimpton (2003). Confined granular packings: Structure, stress, and forces. *Phys. Rev. E* 67 (4), p. 041303.

Lee, C.-H. and C.-J. Huang (2012). Kinetic-theory-based model of dense granular flows down inclined planes. *Physics of Fluids* 24.7, p. 073303.

Lois, G., A. Lemaître and J.M. Carlson (2006). Emergence of multicontact interactions in contact dynamics simulations of granular shear flows. *Europhysics Letters* 76.2, p. 318.

Malahe, M. (2012). A one-way coupled DEM-CFD scheme to mode free-surface flows in tumbling mills. MSc dissertation. University of Cape Town.

Malvern, L.E. (1969). *Introduction to the Mechanics of a Continuous Medium*. Prentice-Hall series in engineering of the physical sciences. Prentice-Hall.

McBride, A., I. Govender, M. Powell and T. Cloete (2004). Contributions to the experimental validation of the discrete element method applied to tumbling mills. *Engineering Computations* 21.2-4, pp. 119–136.

McCarthy, J.J., V. Jasti, M. Marinack and C.F. Higgs (2010). Quantitative validation of the discrete element method using an annular shear cell. *Powder Technology* 203.1, pp. 70 –77.

Mellmann, J. (2001). The transverse motion of solids in rotating cylinders-forms of motion and transition behavior. *Powder Technology* 118.3, pp. 251–270.

Nakagawa, M., S. A. Altobelli, A. Caprihan, E. Fukushima and E. K. Jeong (Nov. 1993). Non-invasive measurements of granular flows by magnetic resonance imaging. *Experiments in Fluids* 16.1, pp. 54–60.

Ogawa, S., A. Umemura and N. Oshima (1980). On the equations of fully fluidized granular materials. *Journal of Applied Mathematics and Physics (ZAMP)* 31.4, pp. 483–493.

Orpe, A.V. and D.V. Khakhar (2001). Scaling relations for granular flow in quasi-two-dimensional rotating cylinders. *Physical Review E* 64 (3), p. 031302.

Parker, D.J., C.J. Broadbent, P. Fowles, M.R. Hawksworth and P. McNeil (1993). Positron emission particle tracking - a technique for studying flow within engineering equipment. *Nuclear Instruments and Methods in Physics Research*.

Parker, D.J., a.E. Dijkstra, T.W. Martin and J.P.K. Seville (July 1997). Positron emission particle tracking studies of spherical particle motion in rotating drums. *Chemical Engineering Science* 52.13, pp. 2011–2022.

Pathmathas, T. (2015). Granular Flow Modelling of Rotating Drum Flows using Positron Emission Particle Tracking. PhD thesis. University of Cape Town.

Pignatel, F., C. Asselin, L. Krieger, I.C. Christov, J.M. Ottino and R.M. Lueptow (July 2012). Parameters and scalings for dry and immersed granular flowing layers in rotating tumblers. *Physical Review E* 86.1, p. 011304.

Pont, S. Courrech du, P. Gondret, B. Perrin and M. Rabaud (2003). Wall effects on granular heap stability. *Europhysics Letters* 61.4, p. 492.

Pouliquen, O. (1999). Scaling laws in granular flows down rough inclined planes. *Physics of Fluids* 11.3, pp. 542–548.

Pouliquen, O. and F. Chevoir (2002). Dense flows of dry granular material. *Comptes Rendus Physique* 3.2, pp. 163–175.

Pournin, L., Th. M. Liebling and A. Mocellin (2001). Molecular-dynamics force models for better control of energy dissipation in numerical simulations of dense granular media. *Physical Review E* 65 (1), p. 011302.

Pournin, Lionel (2005). On the behavior of spherical and non-spherical grain assemblies, its modeling and numerical simulation. PhD thesis. École Polytechnique Fédérale de Lausanne.

Powell, M.S. and A.T. McBride (2004). A three-dimensional analysis of media motion and grinding regions in mills. *Minerals Engineering* 17.11-12, pp. 1099–1109.

Rajchenbach, J. (1990). Flow in powders: From discrete avalanches to continuous regime. *Physical Review Letters* 65 (18), pp. 2221–2224.

Rajchenbach, J. (2004). Some remarks on the rheology of dense granular flows. *The European Physical Journal E* 14.4, pp. 367–371.

Roux, J. N. and G. Combe (2002). Quasistatic rheology and the origins of strain. *Comptes Rendus Physique* 3.2, pp. 131–140.

Rycroft, C.H., K. Kamrin and M.Z. Bazant (2009). Assessing continuum postulates in simulations of granular flow. *Journal of the Mechanics and Physics of Solids* 57.5, pp. 828 –839.

Savage, S. B. and D. J. Jeffrey (Sept. 1981). The stress tensor in a granular flow at high shear rates. *Journal of Fluid Mechanics* 110, pp. 255–272.

Savage, S.B. (1984). The Mechanics of Rapid Granular Flows. *Advances in Applied Mechanics*. Vol. 24.

Schaeffer, DG (1987). Instability in the evolution equations describing incompressible granular flow. *Journal of Differential Equations* 66.1, pp. 19 –50.

Staron, L., P.-Y. Lagree and S. Popinet (2012). The granular silo as a continuum plastic flow: The hour-glass vs the clepsydra. *Physics of Fluids* 24.10, p. 103301.

Trulsson, Martin, Bruno Andreotti and Philippe Claudin (2012). Transition from the Viscous to Inertial Regime in Dense Suspensions. *Physical Review Letters* 109 (11).

Wills, B.A. and T. Napier-Munn (2015). *Wills' Mineral Processing Technology: An Introduction to the Practical Aspects of Ore Treatment and Mineral Recovery*. Elsevier Science.

Yade Authors (2016). Accessed 11 Feb 2016. URL: `https://yade-dem.org/doc/formulation.html?highlight=forward%20difference#estimation-of-by-wave-propagation-speed`.

Yamane, K., M. Nakagawa, S. a. Altobelli, T. Tanaka and Y. Tsuji (1998). Steady particulate flows in a horizontal rotating cylinder. *Physics of Fluids* 10.6, p. 1419.

Yang, R.Y., R.P. Zou and B Yu A (2003). Microdynamic analysis of particle flow in a horizontal rotating drum. *Powder Technology* 130.1, pp. 138 –146.

da Cruz, F., S. Emam, M. Prochnow, J.-N. Roux and F. Chevoir (2005). Rheophysics of dense granular materials: Discrete simulation of plane shear flows. *Physical Review E* 72 (2), p. 021309.